OPTIMIZATION OF ELECTRIC GUN SETUP TO

STUDY SHOCK RESPONSES OF Zr AND Ti

By

ALOK KUMAR SAXENA

PHYS01201004001

Bhabha Atomic Research Centre,

Mumbai - 400085,

INDIA

A thesis submitted to the

Board of Studies in Physical Sciences

In partial fulfillment of requirements

For the Degree of

DOCTOR OF PHILOSOPHY

of

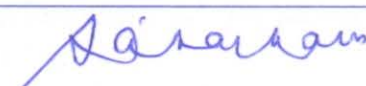# HOMI BHABHA NATIONAL INSTITUTE

December 2015

Homi Bhabha National Institute

Recommendations of the Viva Voce Board

As members of the Viva Voce Board, we certify that we have read the dissertation prepared by Alok Kumar Saxena entitled "Optimization of Electric Gun Setup to Study Shock Responses of Zr and Ti" and recommend that it may be accepted as fulfilling the thesis requirement for the Degree of Doctor of Philosophy.

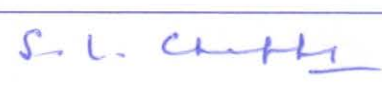|		
Dean, Physical and Mathematical Sciences: Dr. Saibal Basu		Date: 19/12/16
Special Invitee: Dr. Satish C. Gupta		Date: 19.12.2016
Guide/ Convener: Dr. T. C. Kaushik		Date: 23/12/16
Examiner: Dr. G. D. Mukherjee		Date: 19.12.2016
Member: Dr. S. L. Chaplot		Date: 19-12-2017
Member: Dr. B. N. Jagtap		Date: 19.12.2016

Final approval and acceptance of this thesis is contingent upon the candidate's submission of the final copies of the dissertation to HBNI.

I hereby certify that I have read this thesis prepared under my direction and recommend that it may be accepted as fulfilling the thesis requirement.

Date: 19/12/2016

Place: Mumbai

Guide

STATEMENT BY AUTHOR

This dissertation has been submitted in partial fulfillment of requirements for an advanced degree at Homi Bhabha National Institute (HBNI) and is deposited in the Library to be made available under rules of the HBNI.

Brief quotations from this dissertation are permissible without special permission, provided that the source is appropriately acknowledged. Requests for permissions for extended quotation from or reproduction of this manuscript in part or in whole may be granted by the Competent Authority of HBNI when in his or her judgment the proposed use of the material is in the interests of scholarship. In all other instances, however, permission must be obtained from the author.

Alok Kumar Saxena

DECLARATION

I hereby declare that the investigations presented in this thesis have been carried out by me. The work is original and has not been submitted earlier as a whole or in part for a degree/ diploma at this or any other Institution/ University.

Alok Kumar Saxena

List of Publications Arising From the Thesis

Journal

1. A. K. Saxena, T. C. Kaushik, and Satish C. Gupta, "Shock experiments and numerical simulations on low energy portable electrically exploding foil accelerators," Rev. Sci. Instrum. **81**, 033508 (2010).

2. A. K. Saxena, T. C. Kaushik, M. P. Goswami, and Satish C. Gupta, "Printed circuit board based electrically triggered compact rail gap switch," Rev. Sci. Instrum. **81**, 056106 (2010).

3. A. K. Saxena, A. M. Rawool, and T. C. Kaushik, "Crowbar scheme based on plasma motion for pulsed power applications," IEEE Trans. Plasma Sci. **41**, 3058 (2013).

4. A. K. Saxena, M. G. Sharma, and T. C. Kaushik, "Anomalous behavior of electrically exploding aluminum foils under vacuum," IEEE Trans. Plasma Sci. **43**, 2682 (2015).

5. A. K. Saxena, T. C. Kaushik, and Satish C. Gupta, "Shock loading characteristics of Zr and Ti Metals using dual beam velocimeter," J. Appl. Phys. **118**, 075904 (2015).

Conferences

1. A. K. Saxena, T. C. Kaushik, M. P. Goswami and Satish C. Gupta, "Miniaturized low energy electrically exploding foil accelerator," *Proc. of 25th National Symposium on Plasma Science & Technology (PLASMA-2010)*, Guwahati, India, p.84 (2010).

2. A. K. Saxena, T. C. Kaushik, A. M. Rawool, and Satish C. Gupta, "Equation of state measurements using single Fabry-Perot velocimeter," J. of Phys: Conf. Series. **377**, 012049 (2012).

3. A. K. Saxena, A. M. Rawool, and T. C. Kaushik, "A Simple Crowbar Switch for Pulsed Power Applications," *Proc. of 27th National Symposium on Plasma Science & Technology (PLASMA-2012),* Puducherry, India, p.122 (2012).

4. A. K. Saxena, M. G. Sharma, T. C. Kaushik and Satish C. Gupta, "Effect of foil dimensions on flyer velocity in electrically exploding foil accelerators," *Proc. of 28th National Symposium on Plasma Science & Technology, KIIT,* Bhubaneshwar, India, p.159 (2013).

5. Somanand Sahoo, A. K. Saxena, T. C. Kaushik and Satish C. Gupta, "Generation and characterization of metallic nano-particles by electrical explosion of metals," *Proc. of 28th National Symposium on Plasma Science & Technology, KIIT,* Bhubaneshwar, India p.125 (2013).

6. A. K. Saxena, A. C. Jaiswar and T. C. Kaushik, " A low cost optically isolated setup for DC high voltage measurements," *Proc. of 29th National Symposium on Plasma Science & Technology (PLASMA 2014), Mahatma Gandhi University, Kottayam,* Kerala, India, p.342 (2014).

7. A. K. Saxena, S. P. Nayak, A. M. Rawool, A. C. Jaiswar and T. C. Kaushik, "Development of a 200 kJ capacitor bank system for pulsed power applications," *Proc. of 29th National Symposium on Plasma Science & Technology (PLASMA 2014), Mahatma Gandhi University, Kottayam,* Kerala, India. p.343 (2014).

**Dedicated
to
My Parents**

ACKNOWLEDGEMENTS

Contents

5   Equation of State Measurements in Zr and Ti Metals Using Dual Beam Velocimeter   128

6   Conclusions and Future Scope of Studies   138

References   145

Synopsis

The shock waves have astonished mankind for long in its natural but disastrous presence such as lightening, meteorite impact, earthquake, volcanic eruptions etc. as well as fascinated researchers as a nonlinear discontinuity in thermodynamic variables. By suitable techniques, materials may be compressed much beyond their elastic limits under shock loading. The study of materials at such high pressures is important to understand/ predict their behavior in extreme thermodynamic conditions [1-3]. These studies also generate valuable data needed for validation of various numerical codes and theories, which can predict the material response within and beyond experimental limits.

To study materials at such high shock pressures in laboratory environment requires a well characterized shock generating technique as well as fast and precise diagnostics to produce reliable equation of state data. Such experimental techniques were first invented by French scientist Paul Vieille in 1899 to create and study shock in gases. It is important to note here that due to large separation between atoms/ molecules, a pressure of 10-100 bar may lead to strong compression and shock in gases. But in solids due to strong inter-atomic interactions, a compression of a few percent requires pressures of 10-100 GPa. Therefore for shock research on solids, advanced techniques that can create high energy density over small time duration are required and may broadly be categorized as (i) Explosives (ii) Gas guns (iii) Electromagnetic launchers and (iv) Lasers and particle beams. Using these approaches high pressure is normally created either by direct deposition of pulsed energy in material under study or by planar impact of an accelerated flyer plate.

Though chemical explosive requires special experimental facilities but they play a significant role in the evolvement of experimental shock physics and can generate shock pressures over a wide pressure range (10-100's of GPa) [4- 6]. Much higher pressures (up to 10 TPa) were reported in flyer plate experiments by Ahrens [7], using plates of U^{235} in vicinity of nuclear explosion. In parallel to explosive technology, precise shock studies have also been carried out in laboratory environment, using gas guns based on accelerating relatively massive projectiles by different energy sources like propellants, low molecular weight compressed gases (He or H_2) or a combination of both to achieve higher flyer velocities. Velocities up to 7-8 km/s have been obtained on 10-20 gm projectiles [8] on two stage gas gun devices. More intuitive design of three stage gas gun is reported to have achieved velocities up to 16 km/s [9] on low density titanium alloys disks. Electromagnetic launchers overcome this velocity limitation by using high current, pulsed power sources for projectile acceleration. One of these launchers is rail gun; in which flyer is driven by Lorentz forces (**J x B**), and has no theoretical upper velocity limit. But significant loss mechanisms restrict practically achievable flyer velocity to typically 5-6 km/s [10]. Electric gun which is the topic of interest of present thesis, utilizes large thermodynamic forces generated by fast electrical explosion of metal foils along with Lorentz force for flyer acceleration is reported to achieve velocities up to 18 km/s on 43 mg Kapton flyer [11]. Recently much powerful pulsed power source (20 MA, 200ns) at Sandia (Z- machine), was utilized in another intuitive scheme to magnetically drive a 900 µm thick aluminum projectiles to a record velocity of 45 km/s [12]. Laser and particles beams are altogether an important technique to generate shock by direct or by impact method up to TPa regime [13]. Various major laser facilities like Trident, Shiva, Nova and NIF are developed to study the behavior of materials in astrophysical and near to thermo-nuclear fusion conditions.

Out of various techniques discussed above, electric gun is considered for present study due to its significantly high velocity capabilities and less complex operations. Additionally experiments can be carried out on small quantity of target material, which makes it suitable for studies related to precious, toxic and other materials relevant to nuclear energy systems. With careful design considerations even portable systems can accelerate small flyers up to a velocity of typically 6-10 km/s [14, 15], which make this technique comparable to other complex methods like gas gun or explosives. During this research work, electric gun systems of different energies were designed, optimized, and characterized on various metal targets. This include a portable ELG-8 (8 kJ) system majorly used for the high pressure studies reported here and some very compact system to demonstrate feasibility of electric gun for low energy operation. This work also includes the development of a plasma motion based crowbar switch, which is useful for different electromagnetic launchers.

Another crucial task in any shock experiment is to precisely determine the parameters like pressure, particle/ shock velocity and temperature in addition to electrical parameters if pulsed power sources are involved. The task of measurements become critical as the duration of shock experiments normally lies from few 100's of ns to near few µs. The common methods are pressure gauges [16], shock arrival pins [17], electromagnetic particle velocity gauge [18] and radiation pyrometer [19]. Detailed information about shock loading may be obtained by using Doppler shift based optical interferometric techniques [20-22], which can in-situ measure interface velocity profiles. These interferometric techniques are accurate and provide significant insight especially when material is undergoing polymorphic transformations [23, 24]. It may also be noted that phase transformations under shock loading differs from those occurring under static/ isothermal conditions, due to presence of shear stresses, creation of defects and plastic

flow [25]. But as the identification of new phase is difficult in most of the shock experiments, data obtained from complimentary static experiments is used to predict the new phase [26]. Now with the advent of advanced in-situ x-ray diffraction technique [27] it is also possible to detect the compression kinetics at atomic level under shock loading.

In present work Fabry-Perot Velocimeter (FPV), which is based on the principle of Doppler effect, has been developed [28] and used for fast velocity measurements. The capabilities of this velocimeter have also been enhanced to operate it in dual beam mode for simultaneous measurement of projectile and of target-window interface velocity profiles [29, 30]. With this modification two fringe patterns are recorded on a single streak camera that helps in precisely determining the velocities at the time of impact and also makes this technique more economic. Moreover this improvement also makes it a standalone technique for EOS measurements.

The work in present thesis focuses on the development and optimization of electric gun set up along with Fabry-Perot velocimeter as main diagnostic, to measure equation of state (EOS) of different materials, especially titanium and zirconium. Zirconium (Zr) and titanium (Ti) are considered for this study as these metals and their alloys are of great importance for nuclear reactor components as well as nuclear waste containment due to their high corrosion resistance. The low neutron interaction cross-section of Zr is an additional advantage for these applications. Many research groups have studied the high pressure behavior of these metals using facilities like gas gun[31, 32], explosives [33, 34], high power proton beams [33] and a phase transition from hcp (α) to hexagonal (ω) phase had been detected over a wide pressure range. These variations are attributed to pressure levels in high purity titanium by Razorenov *et al.* [33] and to pressure exposure time, hydrostaticity of the pressure, microstructure and impurity

concentration by Sikka *et al.* [35] in general. It is also been reported [31] that phase transition pressure in Zr increases from 7.1 GPa to 8.3 GPa with an increase in impurity content typically from 0.02 to 0.1 % by weight and even the signature of phase transition was found absent in particle velocity profile for an impurity concentration of 1.8 %. Most of these studies were carried out on thick samples and very few have reported results on thin foils [33] where shock loading time is comparatively small. The present study validates the measurements on thin foils with the work published in literature on much thicker samples where pressure exposure time is sufficiently long. The outcomes of present work also prove the significance of compact electric gun systems in shock research.

The performance of developed electric gun system is first optimized to achieve high velocity projectiles with reasonable planarity. These optimizations include the parametric investigations of flyer/ foil dimensions, current rise time, and ambient pressure on flyer performance. The exploding foil characteristics have been studied under vacuum down to 10^{-4} mbar and in contrast to its behavior near atmospheric pressure, foil performance has been found to degrade significantly at low vacuum levels [36]. To achieve faster current rise time from existing setup, a concept of two stage exploding foil assemblies [37] is implemented and flyer performance is experimentally investigated using Fabry-Perot velocimeter. Another important outcome of these optimization studies is the enhancement in flyer velocity by plasma propulsion effect, which is governed by the exposed barrel area. With these optimizations a velocity of 4.5 km/s on aluminum flyers and 6.3 km/s on polyimide flyers have been achieved on ELG-8 system. The present work also includes the modification and implementation of an existing 1-D Lagrangian finite difference formulation to theoretically predict the flyer velocity profiles. The code performance is validated against experimental and simulation data reported in published

works as well as on our systems. The outcomes of this code have proven to be helpful in designing new systems and in optimization of existing setups.

To validate the system for shock research, characterization studies were carried out with single beam Fabry-Perot velocimeter using targets of different metals like aluminum, copper, tin, tantalum, and iron in the form of thin foils and were subjected to short duration (100-200 ns) shock pulses and pressures up to 70 GPa have been achieved in tantalum foils. Iron is considered for this study as it is well known structural material, found in earth core and deeply investigated by shock as well as static research community. Measurements of its phase transition pressure confirm the potential of our system along with diagnostics. Measured EOS data on these thin foils have been found to be matching well with the published results. In second phase of experiments better measurement accuracies were achieved by developing a dual beam Fabry-Perot velocimeter to simultaneously measure the velocity profiles of target as well as that of flyer using a single setup of streak camera and laser. The standard FPV, which is normally used in shock research, measures the velocity of a single surface. But the measurements of two velocities are crucial to determine the Hugoniot of a given material. In present work a single FPV is modified in such a way that it can measure two velocities on a single setup. This improvement in FPV makes shock diagnostics economic and operationally simple. Equation of state measurements have been carried out on zirconium and titanium metals under shock loading up to pressures of 12 GPa and 16 GPa respectively. Measured EOS data on thin foils has been found to be matching well with the data reported in literature on relatively thicker samples. The detailed velocity profiles of target-glass interface show a weak kink in its rising part indicating a phase transition from α phase to ω phase. These experiments also confirm the potential of dual beam FPV, which can alone be used to determine the EOS of different materials.

To discuss above points in detail the present thesis is organized in six chapters. Chapter-1 gives a brief introduction to shock compression physics, which includes basics about sound waves, their transformation to shock, jump conditions, Hugoniot representations, rarefaction waves, methodology of planar impact experiments and wave profiles under phase transformations. Later various dynamic compression techniques and related diagnostics to measure pressure, velocity and temperature are briefly described.

Chapter-2 elaborates the principle of electrically exploding foil accelerator technique along with technical details and capabilities of electric gun setups developed in our laboratory. Development and application of PCB based spark gap switch as well as plasma motion based crowbar switch are also discussed in this chapter. Later the description of empirical formulation known as electrical analogue of Gurney relation, and details about one dimensional numerical hydrodynamic scheme for prediction of flyer velocity are elaborated. The diagnostics involved in experiments like magnetic pick up coil for foil current measurements, fiber optic pins for shock velocity measurements, Fabry-Perot velocimeter for particle velocity measurements and its dual beam version are also covered in the last section of this chapter.

Chapter-3 covers the optimization studies carried out on electric gun setup to enhance its performance. This chapter includes the effect of foil dimensions, ambient pressure, current rise time, barrel length and its diameter on flyer velocity profile. The optimization includes the enhancement of flyer velocity by plasma propulsion effect, using barrels of diameter less than the foil size. This chapter also discusses about the concept of two stage exploding foil assemblies. The detailed analysis of these measurements will be presented in this chapter. In the last part the results of one dimensional hydrodynamic numerical simulations on electric gun

system developed in our laboratory as well as on systems reported in literature are given and the effect of return conductor on the final flyer velocity is discussed.

Chapter 4 includes the characterization studies carried out on various metals like tantalum, iron, tin, copper, and aluminum etc. These experimental measurements demonstrate the capabilities of present electric gun setup along with Fabry-Perot velocimeter. First the experiments carried out to measure the flyer velocity and its planarity are described and later shock studies carried out with single beam Fabry-Perot velocimeter to record the velocity profile of target-glass interfaces are discussed. In these experiments flyer velocity was assumed from the many repeatable and reproducible measurements carried out in similar conditions. Pressures up to 70 GPa were achieved on tantalum targets in these studies and are reported in this chapter. The results of shock velocity measurements in stepped targets of copper and tantalum at 23 GPa and 48 GPa respectively using in-house designed fiber optic shock arrival pins are also presented in last section of the chapter.

Chapter 5 covers the experimental studies carried out on zirconium and titanium metals using dual beam velocimeter where two velocities were simultaneously measured. The details of experimental results and phase transition detected in velocity profiles will be elaborated here. The techniques used to improve the measurement accuracies using common streak record are also discussed in this chapter.

The summary of the research work carried out in present thesis is described in the last chapter (Chapter 6). This chapter provides significant outcomes of experimental results and the possibilities for future research on portable electric gun setup at enhanced pressures. This chapter includes the work highlights showing the potential of low energy electric gun setup along with

dual beam FPV for high pressure research in small laboratories. These highlights mainly include the determination of polymorphic phase transition in iron, zirconium and titanium metal foils under shock loading and generation of peak pressure up to 70 GPa in tantalum metal foils. A list of references used in this thesis along with a list of publications is provided in the last.

References

[1]. L. V. Al'tshuler, "Use of shock waves in high pressure physics," Sov. Phys. Usp. **8**, 52 (1965).

[2]. V. E. Fortov, "Intense shock waves and extreme states of matter," Phys.-Usp. **50**, 333 (2007).

[3]. M. Ross, "Matter under extreme conditions of temperature and pressure," Rep. Prog. Phys. **48**, 1 (1985).

[4]. R. A. Graham, in: *Solids under high pressure shock compression: Mechanics, Physics and Chemistry*, (Springer-Verlag, NY, 1993), p.55-58.

[5]. H. S. Yadav and N. K. Gupta, "Flyer plate motion and its deformation during flight," Int. J. Impact Engg. **7**, 71 (1988).

[6]. D. J. Grosch, "Inhibited shaped charge launcher testing of spacecraft shield designs," Southwest Research Institute Report No. 06-3513 (1996).

[7]. T. J. Ahrens, "Shock wave techniques for geophysics and planetary physics," in: *Methods of experimental physics: Geophysics laboratory measurement*, (Academic Press Inc. Orlando Florida, 1987), pp.185-233.

[8]. H. F. Swift, "Light gas gun technology: A Historical perspective," in: *High pressure shock compression of solids VIII : The science and technology of high-velocity impact*,

edited by L.C. Chhabildas, L. Davison, and Y. Horie, (Springer-Verlag Berlin Heidelberg Germany, 2005), p.1.

[9]. L. C. Chhabildas, L. N. Kmetyk, W. D. Reinhart, and C. A. Hall, "Enhanced hypervelocity launcher - capabilities to 16 km/s," Int. J. Impact. Engng. **17**, 183 (1995).

[10]. D. Wetz, F. Stefani, J. Parker, and I. McNab, "Development of a plasma-driven railgun to reach 7 km/s," Proc. IEEE Int. Power Mod. and High Voltage Conf. pp.85-88, (May 2008).

[11]. J. E. Osher, H. H. Chau, G. R. Gathers, R. S. Lee, and R. C. Weingart, "Application of a 100-kV electric gun for hypervelocity impact studies," Int. J. Impact Engng. **5**, 501 (1987).

[12]. R. W. Lemke, M. D. Knudson, and J-P Davis, "Magnetically driven hyper-velocity launch capability at the Sandia Z accelerator," Int. J. Impact Engng. **38**, 480 (2011).

[13]. H. Nagao *et al.*, "Hugoniot measurement of diamond under laser shock compression up to 2 TPa," Phys. Plasmas. **13**, 052705 (2006).

[14]. A. K. Saxena, T. C. Kaushik and S. C. Gupta, Shock experiments and numerical simulations on low energy portable electrically exploding foil accelerator, Rev. Sci. Instrum. **81**, 033508 (2010).

[15]. G. Wang, J. He, J. Zhao, F. Tan, C. Sun, J. Mo, X. Xong and G. Wu, "The techniques of metallic foil electrically exploding driving hypervelocity flyer to more than 10 km/s for shock wave physics experiments," Rev. Sci. Instrum. **82**, 095105 (2011).

[16]. G. Yiannakopoulos, "A review of manganin gauge technology for measurements in gigapascal range," MRL Tech Report- MRL-TR-90-5 (1990).

[17]. R. F. Benjamin and F. J. Mayer, "Applications of the microshell-tipped optical fiber", Optical Fiber Sensors, (Optical Society of America), paper ThFF4 (1985).

[18]. M. B Boslough and T J Ahrens, "Particle Velocity Experiments in Anorthosite and Gabbro," in: *Shock Waves in Condensed Matter*, edited by J. R. Asay, R. A. Graham, G. K. Straub, (Elsevier Science, NY, 1983), pp. 525-528.

[19]. G. A. Lyzenga and T. J. Ahrens, "Multiwavelength optical pyrometer for shock compression experiments," Rev. Sci. Instrum. **50**, 1421 (1979).

[20]. L. M. Barker and R. E. Hollenbach, "Laser interferometer for measuring high velocities of any reflecting surface," J. Appl. Phys. **43,** 4669 (1972).

[21]. C. F. McMillan, D. R. Goosman, N. L. Parker, L. L. Steinmetz, H. H. Chau, T. Huen, R. K. Whipkey, and S. J. Perry, "Velocimetry of fast surfaces using Fabry-Perot interferometry," Rev. Sci. Instrum. **59**, 1 (1988).

[22]. J. Weng, H. Tan, S. Hu, Y. Ma and X. Wang, "New all fiber velocimeter," *Rev. Sci. Instrum.*, **76**, 093301 (2005).

[23]. L. M. Barker and R. E. Hollenbach, "Shock wave study of the $\alpha \rightleftarrows \epsilon$ phase transition in iron," J. Appl. Phys. **45**, 4872 (1974).

[24]. J. C. Boettger and D. C. Wallace, "Metastability and dynamics of the shock-induced phase transition in iron," Phys. Rev. B, **55**, 2840 (1997).

[25]. J. W. Forbes, in: *Shock wave compression of condensed matter: Shock wave and high pressure phenomenon: A primer*, (Springer NY, 2012) pp.201-241.

[26]. G. E. Duvall and R. A. Graham, "Phase transitions under shock-wave loading," Rev. Mod. Phys. **49**, pp.523-579 (1977).

[27]. D. H. Kalantar *et al.*, "Direct observation of the α−ε transition in shock-compressed iron via nanosecond X-ray diffraction," Phys. Rev. Lett. **95**, 075502 (2005).

[28]. A. K. Saxena, T. C. Kaushik, A. M. Rawool, L.V. Kulkarni, and S. C. Gupta, "Optical velocimetry of fast moving surfaces," BARC Report No. BARC/2007/E013 (2007).

[29]. A. K. Saxena, T. C. Kaushik, A. M. Rawool, and Satish C. Gupta, "Equation of state measurements using single Fabry-Perot velocimeter," J. of Phys: Conf. Series. **377**, 012049 (2012).

[30]. A. K. Saxena, T. C. Kaushik, and Satish C. Gupta, "Shock loading characteristics of Zr and Ti Metals using dual beam velocimeter," J. Appl. Phys. **118**, 075904 (2015).

[31]. E. Cerreta, G.T. Gray, R. Hixson, P.A. Rigg, and D.W. Brown, "The influence of interstitial oxygen and peak pressure on the shock loading behavior of zirconium," Acta. Mater. **53**, 1751 (2005).

[32]. E. Cerreta, G. T. Gray III, A. C. Lawson, T. A. Mason, and C. E. Morris, The influence of oxygen content on the α to ω phase transformation and shock hardening of titanium, J. Appl. Phys. **100**, 013530 (2006).

[33]. S. V. Razorenov, A. V. Utkin, G. I. Kanel, V. E. Fortov, A. S. Yarunichev, K. Baumung, and H. U. Karow, "Response of high purity titanium to high pressure impulsive loading," High Press. Res. **13**, 367 (1995).

[34]. A. R. Kutsar, M. N. Pavlovskii, and V. V. Komissarov, "Observation of a two wave shock configuration in zirconium," JETP Lett. **39**, 480 (1984).

[35]. S. K. Sikka, Y. K. Vohra, and R. Chidambaram, "Omega phase in materials," Prog. Mater. Sci. **27**, 245 (1982).

[36]. A. K. Saxena, M. G. Sharma, and T. C. Kaushik, "Anomalous behavior of electrically exploding aluminum foils under vacuum," IEEE Trans. Plasma Sci. **43**, 2682 (2015).

[37]. T. C. Kaushik, L. V. Kulkarni and S. K. H. Auluck, "Feasibility studies on performance enhancement in electrically exploding foil accelerators," IEEE Trans. Plasma Sci. **30**, 2133, (2002).

List of Figures

List of Tables

Chapter 1

Introduction

1.1 Motivation

The aim of present research is to develop an experimental facility to study the high pressure dynamic behavior of materials having scientific importance as well as applications in nuclear systems. Considering the compact nature, easy operational procedures and high velocity capabilities; electric gun is chosen as the shock generating device for present studies. The optimization of electric gun to accelerate planar projectiles to high velocities is the main part of this research. Another crucial activity of this investigation is to develop precise optical diagnostics that can accurately measure the equation of state of materials. In this quest Fabry-Perot velocimeter is optimized to simultaneously record the velocity profiles of two surfaces for determining the equation of state in a precise and economic way. Optical fiber based sensor technique is also explored to measure the planarity of projectiles and shock wave velocities in impacted step targets.

Zirconium (Zr) and titanium (Ti) are considered for this study as these metals and their alloys are of great importance for nuclear reactor components as well as nuclear waste containment due to their high corrosion resistance. The low neutron interaction cross-section of Zr is an additional advantage for these applications. The alpha to omega phase transition in these metals is the topic of scientific interest due to dependence of transition pressure on various

parameters. The important aspect of present study is that, it reports phase transitions on thin foils where shock loading time is relatively small, in contrast to most of the other reported works on thicker samples using relatively large and complex facilities.

1.2 Preface

The study of matter under extreme conditions has long been the topic of interest but it significantly marked its position in scientific literature during 1950-1960 with the advent of devices based on chemical and nuclear energies. Such studies are also of interest to fundamental physicist as these conditions occur more prevalently in astrophysical bodies at much higher pressures and temperatures. Many interesting phenomenon like phase transition, shock melting, fracture, spall, formation of warm dense matter etc. are found to take place in such conditions. Compression studies are also relevant to generate valuable equation of state data of different materials over a wide thermodynamic range, which are useful for validating various numerical schemes.

In laboratory environment compression along different thermodynamic regimes may be achieved by various experimental schemes. By the temporal nature of compression forces and response of material these schemes may be broadly categorized as static and dynamic. Under static compression a diamond anvil cell (DAC) is commonly used to hydrostatically compress the material between two diamonds through a pressure transmitting media. The process of compression generates the data along an isothermal path and pressures up to 750 GPa [1] has been reported so far. The dynamic compression methods like shock and quasi-isentropic schemes can subject the material to much higher pressures as well as to high temperatures. The dynamic schemes mostly create pressure along a single direction, which under certain conditions may be

approximated to hydrodynamic compression. The dynamic pressures are normally created by generating high energy densities over small time durations. Considering the way of creating pulsed energy these methods may broadly be categorized as (i) Explosives (ii) Gas guns (iii) Electromagnetic launchers and (iv) Lasers/ particle beams. By suitably controlling the rate of energy deposition [2- 4] or by using multi-layered geometries [5, 6]; the shape of pressure pulse may be modified to avoid the formation of shock and compress the material in isentropic conditions up to certain thickness. The present thesis is focused on shock compression studies of different metals by planar impact of a high velocity projectile. Therefore basics about shock physics in such conditions will be considered here while more details may be found in cited references.

Under high pressure loading shuffling at atomic and electronic levels may take place which may lead to interesting phenomenon of phase transformation. Due to fast nature, martensitic phase transformations are frequently observed under shock compression. But due to presence of shear stresses some sluggish transformations like α to ε phase in iron has also been found to occur under shock. The polymorphism of Group 4 elements has gained a lot of attention of scientific community in static as well as dynamic research. This is due to significant difference and variations observed in their transition pressure from α to ω phase by both the communities. The published phase transition pressure under shock loading varies from 6.2 GPa [7] to 8.3 GPa [8] for Zr and 5.1 GPa [9] to 11.9 GPa [10] for Ti. These variations are attributed to pressure levels in high purity titanium by Razorenov *et al.* [9] and to pressure exposure time, hydrostaticity of the pressure, microstructure and impurity concentration by Sikka *et al.* [11] in general. Various theoretical and experimental studies have been carried out to understand the effect of impurities, peak shock stress, and texture on phase transition kinetics [12-17]. It has

also been reported [8] that phase transition pressure in Zr increases from 7.1 GPa to 8.3 GPa with an increase in impurity content typically from 0.02 to 0.1 % by weight and no signature of phase transition was found in particle velocity profile for an impurity of 1.8 wt %.

In summary, investigations of various metals especially Group 4 elements under shock loading are significant for fundamental research as well as in applied sciences due to their high strength to density ratio and role in nuclear reactor components, where they may be subjected to extreme conditions. The generation of well characterized shock pulses and precise diagnostics are key requirements to carry out shock research on these important metals at laboratory scale, which is the aim of present thesis. A portable electric gun launcher along with optical interferometric system has been developed to fulfill this aim. Following sections will discuss about the fundamentals of shock as well as about its generation and measurement techniques.

1.3. Historical overview of shock research

The shock may be considered as a discontinuity in thermodynamic variables, which propagates with supersonic velocity with respect to the material ahead of it and with subsonic velocity with respect to the material behind it. The formation of such discontinuities is initiated by the sudden release of large energy in small volume. Various natural events such as lightning, earthquakes, tsunami, meteorite impact, and volcanic eruptions lead to formation of destructive shock fronts. But the study of such events in controlled way in laboratory conditions started with the advent of shock tube, in 1899 by French scientist Paul Vieille to generate shock in gases. In these devices shock is generated by sudden rupture of a diaphragm separating the two chambers with one containing gas at much higher pressure than other. Later with the discovery of chemical explosives much higher pressures were generated using blast waves [18]. Due to large separation

between atoms/ molecules in gases, strong compression and shock can be generated by a typical pressure of 10-100 bars. However in solids interaction forces between atoms mainly decide its pressure along with thermal energy contribution from lattice and electrons. Due to such forces, compression of a few percent in solids requires pressures of 10-100 GPa. To achieve such pressures chemical and nuclear energy related systems were used in mid 1960's and pressures up to TPa [19] were reported. In parallel to these direct energy driven systems, another approach of generating high pressure pulses by projectile impact was also perceived during 1948 [20] with the so called powder guns. These initial phase guns were based on accelerating projectiles by energy stored in propellants and limited to a velocity of 2.3 km/s. This limit comes because a significant part of supplied energy is used to accelerate high molecular weight burn products of propellants. To overcome this limit two stage light gas guns were built during 1955 to 1965 and velocities up to 7-8 km/s were reported [20, 21]. These guns are based on accelerating the projectile by a low mass highly compressed gas such as hydrogen/ helium. The hydrogen was compressed up 1GPa pressure by the projectile accelerated by propellants in first stage [22]. This technology was further improved by the design of three stage gas gun, which is reported to have reached velocities up to 16 km/s [23] on low density titanium alloys disks. In above described techniques the maximum flyer velocity is governed by the speed of sound, with which the pressure information is carried from energy source to the flyer. Electromagnetic launchers may overcome this limitation by using high current, pulsed power sources for projectile acceleration. One of these launchers is rail gun; in which flyer is driven by Lorentz forces ($\mathbf{J \ x \ B}$), and has no theoretical upper velocity limit. But significant loss mechanisms restrict practically achievable flyer velocity to typically 5-6 km/s [24-26]. Electrical explosion of metal conductors for shock generation was first proposed and reported by Keller and Penning [27] & by Guenther *et al.* [28]

in 1960's to produce planar shock waves. Later this work has been carried out by many researchers and this so called "electric gun" technique has emerged out as an efficient device for generating pressures in 0.5-1 TPa regimes and study the EOS of materials [29, 30], as well as initiation behavior of energetic materials [31, 32]. Electric gun which utilizes large thermodynamic forces generated by fast electrical explosion of metal foils along with Lorentz force for flyer acceleration is reported to achieve velocities of up to 18 km/s on 43 mg Kapton flyer [33].

Recently much powerful pulsed power source (20 MA, 200ns) at Sandia (Z- machine), has been utilized to magnetically accelerate 900 μm thick aluminum projectiles to a record velocity of 45 km/s [34] using the precisely shaped current pulses. Laser is altogether another important technique to generate shock by direct or by impact method up to TPa regime [35, 36]. Various major facilities like Trident, Shiva, Nova and NIF are developed to study the behavior of materials in astrophysical and near to thermo-nuclear fusion conditions.

1.4 Basics of shock waves:

The shock may be considered as a nonlinear form of sound wave. Its formation is initiated when the amplitude of pressure pulse becomes so high that the velocity at different points on a wave profile becomes a function of pressure. In case of a normal sound wave (plane) traveling in 'x' direction the equations of motion are linear and solution may be represented in functional form of 'x ± ct', where 'c' is sound velocity and 't' represents the time. Under the assumption of small variations in thermodynamic parameters and constant entropy (S), sound velocity (c) may be written as (see [37], p.252):

$$c = \sqrt{\left(\frac{\partial P}{\partial \rho}\right)_S} \qquad (1.1)$$

In above expression 'P' and 'ρ' represents the pressure and density respectively. In most of the materials the pressure to density characteristics are linear up to elastic limit, after which the slope of $(\partial P/\partial \rho)$ becomes positive. Therefore in nonlinear regime the velocity of a disturbance ('v') becomes a function of density or pressure and may be written as (see [37], p.380):

$$v = u \pm c\,(u) \qquad (1.2)$$

Here 'u' the velocity of the medium and is a function of pressure or density. Now the different points on the profile of a disturbance are at different pressures and move with different velocity. Therefore the shape of a pressure profile changes in time as it propagates through the
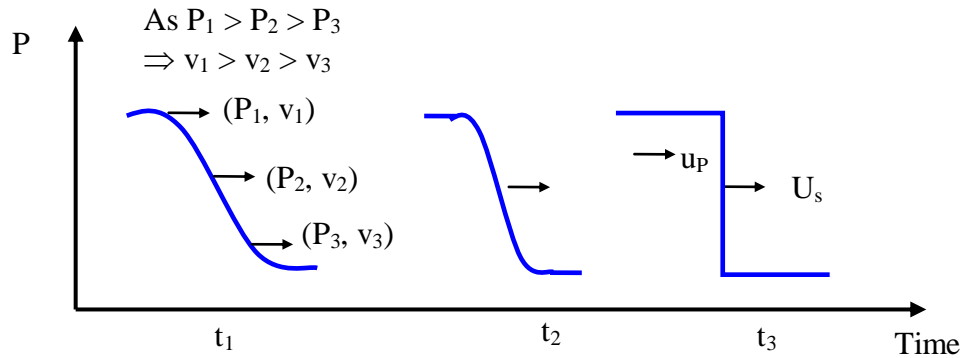
Fig. 1.1: Formation of a shock front.

medium. It is possible to show (see [37], p.367) that in a medium with $(\partial^2 P/\partial^2 \rho) > 0$ the $(\partial v/\partial \rho)$ is also positive by taking the derivative of Eq.1.2, and using the equations of continuity and momentum conservation. Therefore to form a shock wave in a medium the necessary condition

is that $\partial^2 P/\partial^2 \rho$ should be positive. The detailed as well as elaborated derivations may be found in Refs. 37 and 38 and later discussion on Hugoniot curve will also make this point more clear.

To understand the formation of shock, let us consider a disturbance profile with negative gradient of density along its direction of propagation (x-direction). Then the points on wave profile at higher density will move faster than the points at lower density making the front steeper with time. The sharpening of density front is opposed by the energy loss mechanism like thermal conduction and viscosity, the balance of two finally leads to the formation of a stable shock front. This process of shock formation is pictorially shown in Fig.1.1. The shock wave now divides the medium in two parts one undisturbed low pressure region ahead of it and other compressed region behind it. Once it becomes steady the shock front moves with a supersonic velocity (U_S) with respect to the medium ahead of it and the material follows it with a velocity 'u_P'. At this moment the wave parameters become multi valued at the shock front, therefore partial differential equations normally used for the solution of pressure waves ceases to valid at the discontinuity but it may be noted they remains valid in other regions. To connect the parameters of two regions separated by a shock, conservation of mass, momentum and energy are used to deduce jump conditions commonly known as Rankine-Hugoniot relations:

(1) Mass Conservation:

$$\rho_0 U_s = \rho(U_S - u_P)$$
(1.3)

(2) Momentum Conservation:

$$P - P_0 = \rho_0 U_S u_P$$
(1.4)

(3) Energy Conservation:

$$E - E_0 = \frac{1}{2}(P + P_0)(V_0 - V) \tag{1.5}$$

Here the subscript '0' is used to represent undisturbed medium and E is the specific internal energy, while V is the specific volume. These three equations are quite general in nature and independent of material properties. Assuming that the parameters of undisturbed medium are known, then there are total five unknowns (P, ρ, E, U_S, u_P) with three equations. With the inclusion of another relation known as equation of state and governed by material properties, there remains only one independent variable.

Equation of State:

$$P = f^n(\rho, E) \tag{1.6}$$

Hence by using above four relations (Eq. 1.3 to Eq.1.6) it is possible to express any unknown parameter in terms of one independent variable. These relations are known as Hugoniot relations and in pressure-volume space it may be expressed as:

Hugoniot relation:

$$P = H(V, P_0, V_0) \tag{1.7}$$

The curves representing above relation in a two dimensional space are referred as "Rankine-Hugoniot" curves or only "Hugoniot". It may be noted here that Eq. 1.7 represents a set of curves each starting at different value of initial state (P_0, V_0). As above equations connect two states across a shock front, therefore Hugoniot is not a thermodynamic path, but it is the locus of all possible final states that can be achieved by the passage of a single steady shock, starting from the same initial state. Under shock compression material follows the path of a

straight line known as "Rayleigh line" joining the initial and final states. A typical Hugoniot curve along with Rayleigh line is shown in Fig.1.2. Here up to certain limit, known as "Hugoniot Elastic Limit (HEL)" the curve remains linear and afterwards it becomes concave upward at higher pressures. The value of Hugoniot elastic limit for most of the metals lies within few GPa. It is also interesting to note the certain materials like fused silica have their Hugoniot convex upward $((\partial^2 P/\partial^2 \rho) < 0)$ up to certain pressure and do not support the formation of shock in that region.
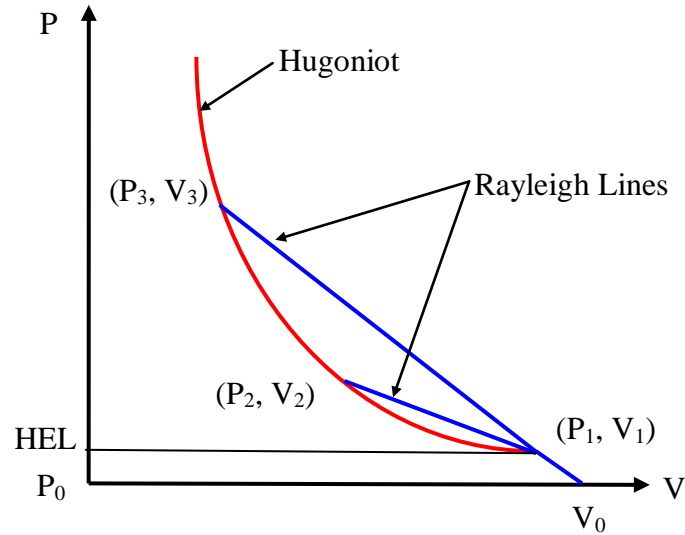
Fig.1.2: Hugoniot representation in P-V plane.

It is also important to note that Hugoniot are not only limited to P-V plane but are also represented in P-u_P plane to directly predict the outcomes of planar impact experiments and wave interactions. As Hugoniot is a material property, in P-u_P plane it can be reflected and translated according to direction of propagation of shock and initial particle velocity respectively.

To elaborate the importance of Hugoniot further two important relations may be derived from Eq.1.3 and Eq. 1.4:

$$U_S = V_0 \sqrt{\frac{P - P_0}{V_0 - V}}$$ (1.8)

$$u_P = \sqrt{(P - P_0)(V_0 - V)}$$ (1.9)

It can be observed from Eq.1.8 that square of shock velocity $(U_S)^2$ is proportional to the negative slope of Rayleigh line, so for materials having $(\partial^2 P/\partial^2 \rho) > 0$, shock velocity increases with pressure. Considering Eq.1.9 and Eq. 1.5, it is easy to see that specific kinetic energy $(u_P^2/2)$ of material following the shock is equal to its specific internal energy; if 'P_0' is much smaller than 'P' which is normally the case.

In linear region of Hugoniot the disturbances propagate with the speed of sound determined by the square root of its slope. If pressure crosses the linear limit shock formation takes place. For low pressures near to HEL, it is physically not possible to join the initial and final states by a single Rayleigh line as its slope $(\sim U_S^2)$ becomes smaller than the slope of linear part $(\sim c^2)$ and violates the condition of supersonicity of shock wave. In such situations final state may be reached by two waves one elastic wave taking the material from (P_0, V_0) to (P_1, V_1) and other shock wave taking it further from (P_1, V_1) to final state (P_2, V_2). Therefore for low amplitude shocks the slope of Rayleigh line is smaller than the slope of elastic part hence an elastic wave (elastic precursor) always leads the shock. But for pressures higher than (P_3, V_3) a single shock may be formed without violation of any stability condition and formation of elastic precursor. In general whenever there is a cusp in the Hugoniot, a single stable shock is not possible for certain pressure range, it will always split in two wave structure. These cusps also appear due to phase transition in material at a certain pressure leading to negative volume change as will be discussed later.

To complete the discussion on Hugoniot, it is important to compare it with other thermodynamic curves. The relative positions of Hugoniot, isentrope and isotherm are shown in Fig.1.3. The area under the curve represents the change in internal energy of material under compression. The total internal energy consists of elastic energy (potential energy) due to Coulomb interactions as well as thermal energy due to lattice vibrations and electronic excitations. In isothermal process the increase in internal energy is only due to elastic energy part but in an isentrope thermal parts also contribute, hence isentrope lies above the isotherm. The isentropic processes are reversible in nature but in Hugoniot energy also goes in plastic form leading to increase in entropy and temperature. The irreversible heating makes the Hugoniot to lie above the isentrope. The increase in entropy across low amplitude shocks may be written as [39]:

$$\Delta S = -\frac{1}{12T_0}\left(\frac{\partial^2 P}{\partial V^2}\right)_{atS=S_0}(V-V_0)^3 + ...\tag{1.10}$$
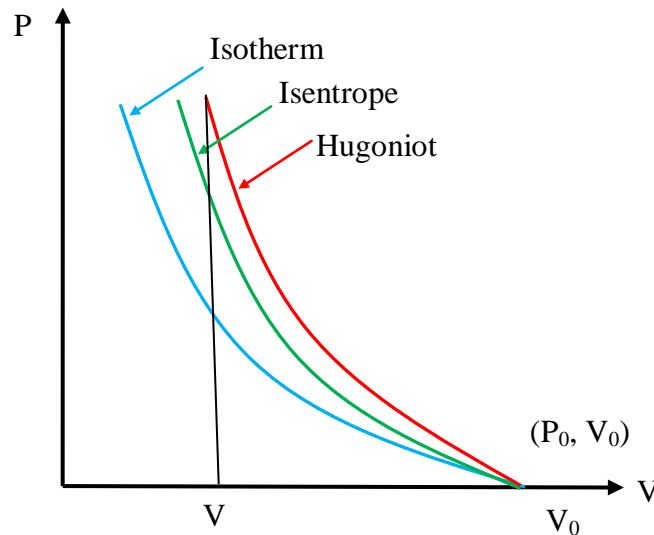
Fig.1.3: Relative position of Hugoniot with other thermodynamic curves.

Here 'T$_0$' represents the initial temperature of the material. Hence under rapid shock compression ((V-V$_0$) <0), with no exchange of energy with the surroundings, the process is thermodynamically possible, only when ΔS >0. This indicates that the term (∂^2P/∂^2V) should be positive, which is the basic condition of shock stability.

1.4.1. Rarefaction wave

In the previous section it was discussed that a shock wave is formed when there is a disturbance profile with negative gradient of density along the direction of propagation (x-direction). If instead of negative, there is positive gradient of density and material follows the condition (∂^2P/∂^2V) >0, then the profile of disturbance will spread out in time as shown in Fig.1.4. The points on profile which are at higher density (pressure) will move faster than the points on lower density. This is known as rarefaction wave, which spreads in space and release the peak pressure. The rarefaction wave brings the compressed material back to relaxed state and has particle velocity, opposite to the direction of propagation. It has different velocities at different points on its profile therefore it is represented by a series of curves in P-u$_P$ plane enveloped within highest and lowest velocity.
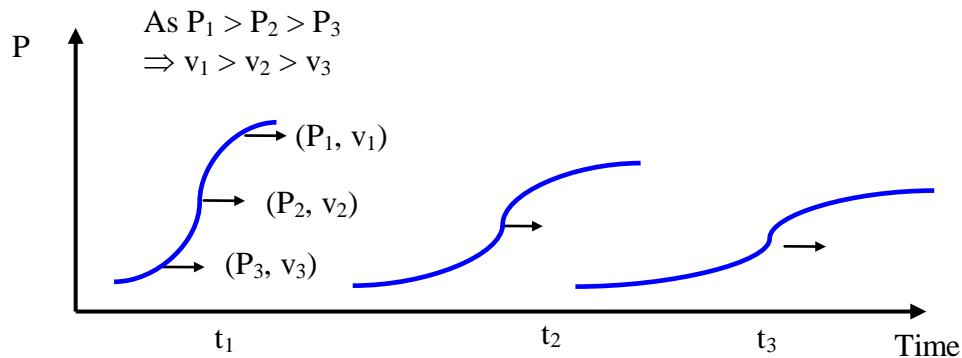
Fig.1.4: Formation of a rarefaction fan.

If in certain regions, Hugoniot of material becomes convex upward ($(\partial^2 P/\partial^2 V) < 0$), then opposite of earlier situation will happen; the points at higher pressure on disturbance profile will move slower than the points at lower pressure. This will lead to formation of a rarefaction shock, where material releases rapidly from a high pressure state.

1.4.2 Hugoniot representations in planar shock compression

Shock experiments are normally performed in one dimensional compression geometries. In these geometries the material is subjected to high strain in one direction mostly by three ways 1) by the impact of a planar projectile 2) by keeping it in contact with the high energy density sources or 3) by rapid energy deposition. Apart from the technique, the compression process is considered to be uniaxial as long as there is no strain in other two directions. But due to finite size of the projectiles as well as of energy sources, a rarefaction wave starts from the free edges and moves towards the centre with the speed of sound in compressed media. Any point where lateral rarefaction wave arrives, the condition of uniaxial compression becomes invalid. Therefore to avoid such lateral effects, measurements should be completed before the arrival of rarefaction wave. As present thesis is focused on shock experiments by projectile impact, we will discuss its details here, other methodologies may be found in cited references [40, 41].

Let us consider the impact of a projectile (A) moving with velocity 'v_F', with the target material (B), which is stationary at time $t = 0$ as shown in Fig. 1.5 (a). On impact one shock will move in the forward direction in the target material and another shock will move in backward direction in the projectile. Now if the Hugoniot curves are drawn for both projectile and target in P-u_p plane, the Hugoniot for projectile (flyer) projectile will start from initial state (P = 0, $u_P = v_F$) and will be moving in left direction to represent the left going shock. While the Hugoniot for

target will start from initial state ($P = 0$, $u_P = 0$) and will be a right going Hugoniot to represent the right going shock. It may be noted that on impact the contact surface of projectile and target should have same pressure as well as particle velocity otherwise it will lead to either separation or intermixing of two materials respectively which is physically not possible. Therefore as shown in Fig.1.5 (b), the point of intersection of two Hugoniot curves gives the final pressure and particle velocity imparted in the target material.

(a)

Before impact at t = 0   After Impact at t = t$_1$
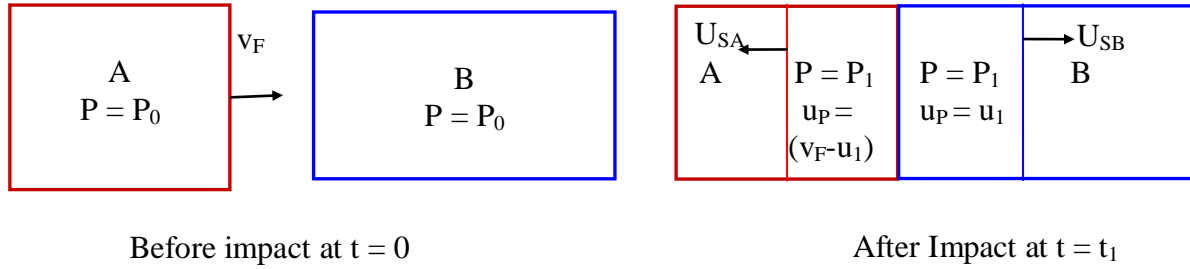
(b)
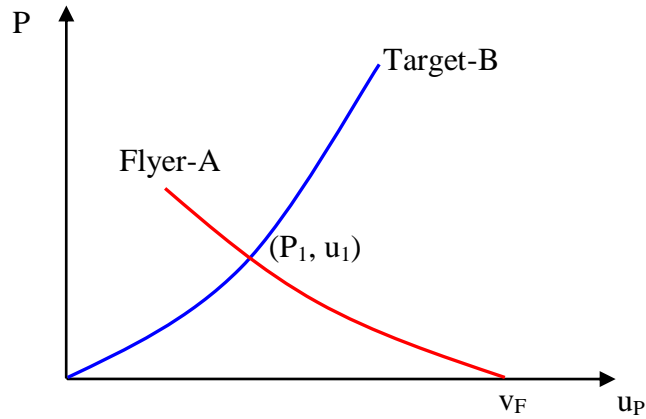
Fig.1.5: Illustration of planar impact configuration for shock studies (a) Impact of a projectile (A) with the target (B); (b) Hugoniot representation in P-u_P plane.

If the parameters like flyer velocity and particle velocity on impact are experimentally measured then it is possible to predict a point on the Hugoniot of target material, assuming

Hugoniot for flyer is known. Therefore a series of shock experiments with different flyer velocities are necessary to generate the Hugoniot of target material.

Shock impedance (Z_S) of a material is an important parameter to predict the final pressure in an impact experiments. It is defined as the product of initial density (ρ_0) and shock velocity (U_S). The pressure induced in a material as per Eq. 1.4 is given by the product of shock impedance and particle velocity (u_P), therefore higher the shock impedance steeper will be the Hugoniot and more will be the shock pressure for a given particle velocity. Therefore flyers/ targets of higher shock impedance may lead to higher pressure on impact. Though the value of shock impedance varies with shock pressure but it is a material property and also represents the toughness of material against compression. The knowledge about the shock impedance of two materials is quite useful when considering the interaction of waves at boundaries with two common guidelines [42]:

a) Wave reflections from the interface with a low impedance material occur with a change in load sign, i.e. rarefaction will reflect as a shock and shock will reflect as a rarefaction.

b) Wave reflections from the interfaces with high impedance material occur with conservation of sign.

1.5 Phase transition under shock compression

There are many materials that show polymorphism under influence of pressure and temperature. These solids have different stable crystalline structures at different pressure and temperature state. When the transition from one state to other occurs with a change in volume by absorption/ release of latent heat, then these are known as first order transitions and are the topic of interest for present work. The historical and well known example of phase transition in shock

(a)

(b)
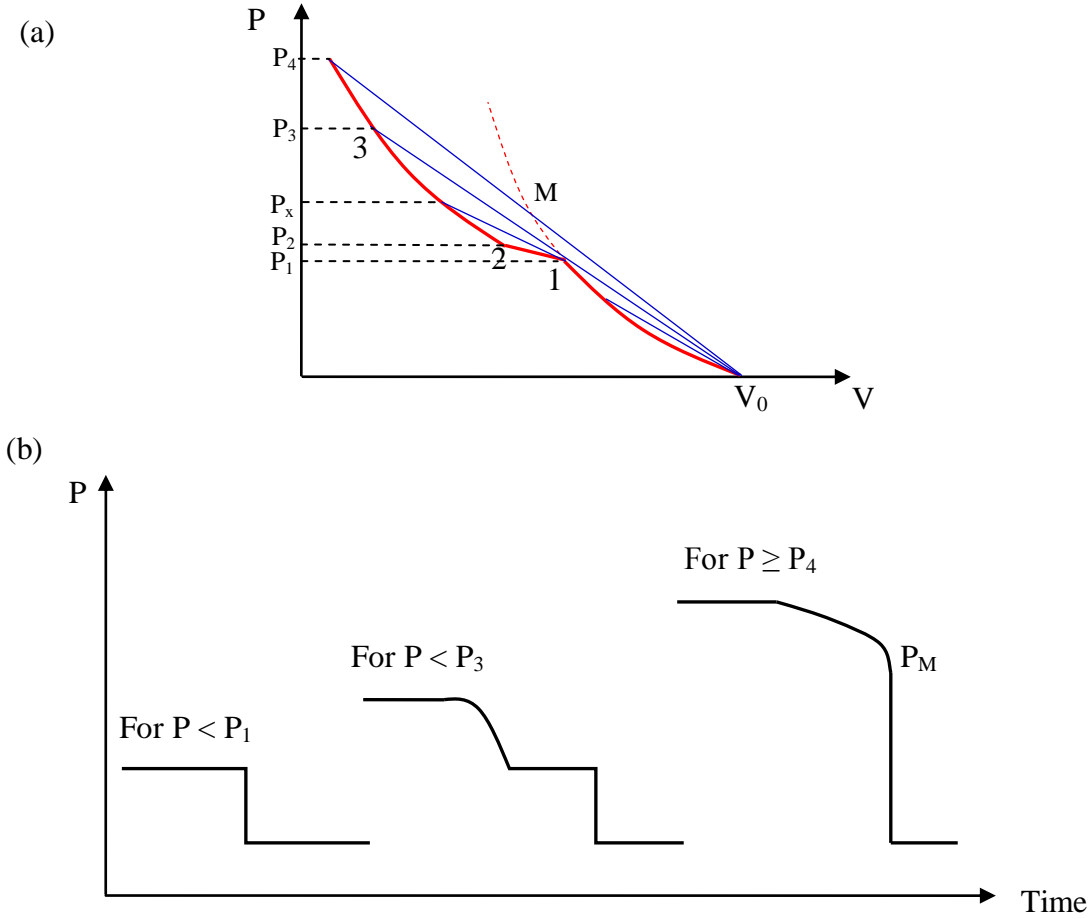
Fig.1.6: Phase transition under shock loading (a) Hugoniot curve in first order phase transition (b) Pressure pulse shape in three different pressure conditions.

[43] as well as in static community [44] is of iron which shows a structural change from α to ε phase near to 13 GPa. Due to change in volume (density) Hugoniot of such materials show a kink or change in slope near to transition point (Fig. 1.6 (a)). The Hugoniot can be divided in three regions, bounded by pressures namely P_1, P_2 and P_3. These regions correspond to Phase-I, Phase-II and mixed phase region (P_1-P_2). Here P_1 represent the transition point, where transformation starts and P_2 where it completes. While P_3 is the pressure point where Rayleigh line starting from initial state and touching the transition point, intersects the Hugoniot. In this figure elastic portion of Hugoniot is ignored assuming pressure is significantly high to suppress

the presence of elastic precursor. For pressures below P_1 (transition point), the shock wave will have the same shape as it is propagating in a material existing in phase-I as shown in Fig.1.6 (b).

When the pressure is higher than P_1 and lesser than P_3, a phase transition occurs and the final state (say P_x) can be achieved only by a combination of two shock waves as shown in Fig. 1.6 (a). The other paths taking material from initial state to final state (P_x) by a single Rayleigh line are physically not possible as this will cut the Hugoniot three times giving rise to three states behind a single shock. In double shock structure, the first will take the material from initial state (P_0, V_0) to transition point (P_1, V_1) with the following velocity, with respect to the material moving behind it:

$$U_{S1} = V_1 \left(\frac{P_1 - P_0}{V_0 - V_1} \right)^{1/2}$$

(1.11)

The another shock will further take this material from state-1 (P_1, V_1) to final sate (P_x, V_x) with following velocity with respect to the material moving ahead of it:

$$U_{S2} = V_1 \left(\frac{P_x - P_1}{V_1 - V_x} \right)^{1/2}$$

(1.12)

As can be seen from the Fig. 1.6 (a) the slope of first Rayleigh line is greater than the slope of second Rayleigh line, therefore $U_{S2} < U_{S1}$, therefore second shock will follow the first shock and phase transition will occur in the rising part of second shock. The thickness of second shock front is governed by the transition kinetics of given material.

Now considering the case when applied pressure is higher than pressure P_3 (say P_4), and a single shock can take the material from phase-I to phase-II. In this case also transition occurs in

the rising part of shock wave, but with an inclusion of intermediate metastable state (M) plotted on the extrapolated Hugoniot of Phase-I.

To complete this discussion, it may be noted that Hugoniot under phase transition has an anomalous region near the kink where it satisfies the condition $(\partial^2 P/\partial^2 V) < 0$. This condition supports the formation of rarefaction shock; therefore in materials with significant kink in Hugoniot, fast drop in pressure is expected in the release path.

1.6 Experimental shock compression techniques

A pressure of typically 10-100 GPa is required to compress any solid by a few percent due to strong interaction forces between its atoms. In shock research such pressures are generated by advanced techniques that can create high energy density over small time duration. Using these approaches high pressure is normally created either by direct deposition of pulsed energy in material under study or by planar impact of a flyer plate. These methods may broadly be categorized as (i) Explosives (chemical, nuclear, shaped charges etc.) (ii) Gas guns (single stage, double stage and compressed gas) (iii) Electromagnetic launchers (rail gun, coil gun, electric gun, and magnetically accelerated flyer plates) and (iv) Lasers and particle beams. In this section we will briefly describe some of these techniques; details may be found in cited references.

1.6.1 Explosives:

Explosives have long been used in shock research. The common experimental methodologies are either to keep explosive in contact or to use it for acceleration of a planar projectile. Explosive lenses are prepared to induce a planar shock front in a material kept in its contact. One such geometry of explosive lens is shown in Fig. 1.7; here a cone of explosive of

lower detonation velocity is kept inside another explosive of higher detonation velocity. The cone angle is decided such that once initiated at top the detonation front reaches on flat surface simultaneously. Pressures up to 45 GPa [40, 45] in near triangular temporal profile, have been achieved by such lenses. To enhance the pressure up to few hundreds of GPa and to generate square shaped pressure pulses, chemical explosives lenses have also been implemented to accelerate metal flyer plates to velocities near to 6 km/s [46]. A lot many approaches have been implemented to achieve much higher flyer velocities; in one such approach cascaded systems have been used to create overdriven shock fronts to achieve velocities more than 10 km/s [47]. The handling of explosives requires special facilities therefore such technologies are limited to few laboratories only.

$$Sin\,\theta = \frac{D_S}{D_F}$$
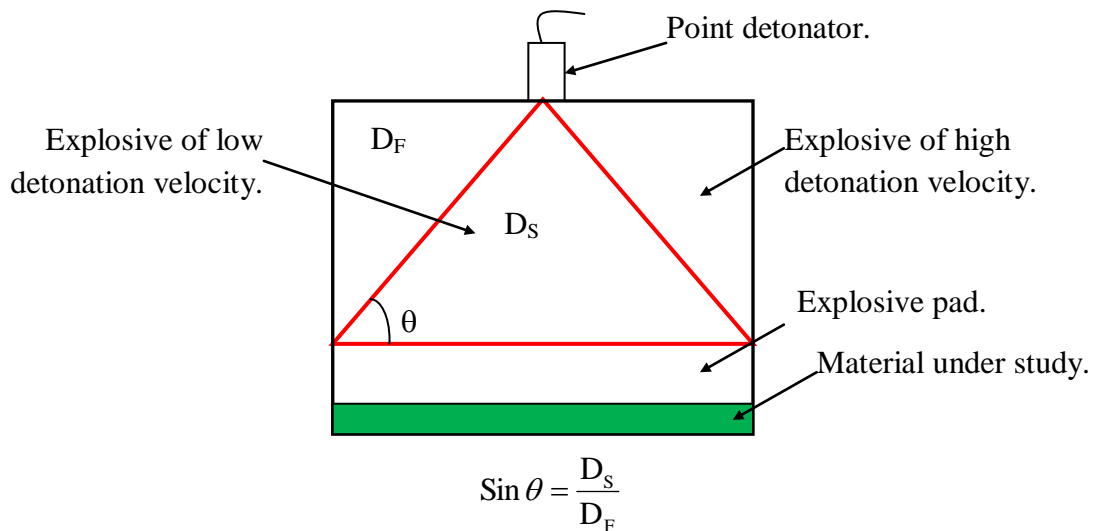
Fig.1.7: Explosive lens, formed by a combination of two explosives.

1.6.2 Single stage compressed gas gun

This is another type of gun where instead of using propellants, gases like Air or Helium compressed up to 300-400 bar are used to drive the projectile. Mechanical pumps are used for

compression and a valve is ruptured to accelerate the projectile by sudden release of compressed gas. These guns are designed for shock compression studies at relatively low pressures (few 10's of GPa) without any stringent laboratory requirements. Velocities around 0.4 km/s and 1 km/s can be achieved by using air and helium as driving gases respectively [48].

1.6.3 Powder gun/ Propellant gun

The concept of propellant gun is conceived from military field guns and rocket launchers to accelerate a projectile by burning propellants. The burning of propellants generates high pressure gases which accelerate the projectile in a barrel. As the energy supplied by the propellant is used in acceleration of projectile as well as in kinetic energy of burnt gases. These guns can accelerate projectile to a velocity of around 2.3 km/s and are used for shock studies up to 100 GPa pressure [22].

1.6.4 Two stage light gas gun

Due to heavy mass of burn gaseous products (~30 g/mole [22]), it is difficult to achieve higher velocities in powder guns. Another factor that affects the final velocity is the speed of sound, which decides the communication limit between the projectile and breach where pressure is generated, which is low for gases of high molecular weight. To overcome these issues a concept of two stage light gas gun is invoked. Here in first stage a piston is accelerated by a powder gun, which dynamically compresses a light gas (Helium or Hydrogen), filled inside its barrel to high pressures. In the central region a valve sealed conical transition is provided between first stage and smaller diameter second stage barrel containing the projectile at its breech. As the piston compresses the gas a limit is reached when the valve between two stages ruptures and the gas rushes into the second stage barrel to accelerate the projectile. The front of

the piston is made of a deformable plastic to still compress the gas till it stops in the conical

region after significant deformation. Velocities up to 8 km/s have been achieved on 16-20 g

projectiles by compressing the hydrogen gas up to 0.7-1 GPa pressure [22]. To still enhance the

projectile velocity, a third stage is augmented to isentropically launch titanium alloy disks up to

16 km/s [23].

1.6.5 Electromagnetic accelerators

As the name implies this category of launchers utilizes electromagnetic forces to

accelerate projectiles to very high velocities. In principle there is no theoretical limit for such

launchers and recently a record velocity of 45 km/s [34] has been reported on 900 μm thick

aluminum projectiles using magnetic forces at Sandia Z- machine. Due to such attractive nature,

a variety of techniques have been developed, out of which some important methods like rail gun,

electric gun, and magnetically accelerated flyer launchers, common in shock research are

discussed here.

1.6.5.1 Rail gun

The rail gun consists of two parallel metal rails connected to a pulsed power source

mostly a capacitor bank or compulsator. The rails are electrically connected to each other by a

movable armature followed by a non-conducting projectile. When the pulsed power source

induces a large current in this arrangement, a Lorentz force acts over both rails as well as on

armature. Rails are fixed but armature is free to move hence it accelerates between the rails to

high velocities along with projectile. The major problem in rail gun is its poor energy efficiency

(<50%), which is decided by residual energy stored in the magnetic flux associated with rails,

resistive losses in rails-armature contacts, frictional losses at the projectile-rail contacts, and air

drag forces. To improve its efficiency various modifications have been proposed, like projectile pre-launching [49], using plasma/ hybrid armatures [50], and distributed energy rail guns [51] etc. But still the practically achievable flyer velocity is reported to be around 5-7 km/s [24] on few grams of projectiles. Considering the practical limitations, present research interest now is shifted towards launching few kg projectiles to a velocity of 2-3 km/s for defense applications [52, 53].

1.6.5.2 Electric gun

This system works on electrical explosion of a thin metallic foil by fast current discharge. The fast and high currents are generated by pulsed power capacitor banks. Due to rapid Joule heating, the energy density in thin foils may reach up to 20-30 kJ/g, which is much higher than the explosive energy density. This leads to very high thermodynamic pressures, which are used to accelerate a thin dielectric projectile (flyer) placed in close vicinity of the exploding foil. The important aspects of electric gun system is its capability of accelerating flyers to high velocities for shock research up to 0.5 TPa [30]   and its operational simplicity. Additionally only a small quantity of target material is required which make this technique suitable for shock studies on precious and toxic materials. Velocities up to 18 km/s are reported in literature on 43 mg Kapton flyer [33].

1.6.5.3 Magnetically accelerated flyer plates

Conceptually this technique is similar to rail gun, where strong magnetic pressure is used to drive the flyers to high velocities, except the amplitude of current pulse is much higher and duration is much shorter. This technique requires fast pulse power sources like Z-machine [54] at Sandia, which can deliver a well shaped current pulse reaching up to 20 MA in 200 ns time in a

short circuit load. The load consists of two closely spaced parallel metal plates having suitable size grooves in anode plate. When the large current passes through the load, field of several Mega-Gauss is generated in between the plates, resulting in 100's of GPa pressure over the anode plate. Due to such high pressures the thin portion of anode plate gets detached and moves inside the grove as a flyer. With accurate MHD simulations two requirements are fulfilled, one is to keep the stress uniform over the grooved anode plate by suitable load design and other is to achieve shockless loading by proper shaping of current pulse. These two conditions ensure that during loading the flyer remains planar without any significant temperature rise. Some portion of flyer plate still gets ablated due to penetration of magnetic field with time leading to joule heating; therefore the usable portion of flyer is lesser than its initial thickness.

The main attractive feature of magnetically driven systems is their capability to launch flyers to very velocities which are not achievable in other schemes. In addition to impact studies these systems are also useful for quasi isentropic compression studies of materials up to 100's of GPa pressure [55].

1.6.6 High power lasers

High power lasers play a significant role in shock research, they are used in various schemes like direct drive, indirect hohlraum drive and laser driven flyers, to create extreme thermodynamic conditions in laboratory environment. In direct drive, a high energy laser pulse is focused on a solid target, which rapidly heats it up and generates expanding plasma in backward direction (laser direction). To conserve the momentum a forward moving shock is induced in the material and an analytical expression for the pressure may be written as [56]:

$$P\,(\text{kbar}) = 230.A^{7/16}.Z_i^{-9/16}.\lambda^{-1/4}.t^{-1/8}(I/10^{12})^{3/4} \qquad (1.13)$$

Here 'I' is the laser intensity in W/cm^2, 'λ' is its wavelength in μm and 't' is the pulse duration in nanoseconds. While 'A' and 'Z_i' are the atomic number and the ionization number of the target material respectively. The generated pressures may be enhanced by placing a transparent confining medium in front of the target material, which impedes the expansion of ablated plasma. However the energy deposited in the target is limited by the breakdown strength of transparent confining medium, which is governed by the properties of confining media, laser wavelength and pulse duration.

Though laser ablation methods may generate pressures in TPa regime [57], but accuracy of equation of state data is mainly restricted by the two major factors. One is the non-uniformity of laser beam over the target surface leading to non-planar shock fronts and other is the preheating of the target before shock arrival by fast moving hot electrons or hard X-rays generated in expanding plasma. To overcome the non planarity issue indirect drive scheme are used [58]. In this scheme, the laser beams are focused inside a small cavity (known as hohlraum), through small holes, and its interaction with cavity walls leads to generation of thermal X-rays. These soft X-rays are used to produce shock waves in the target kept inside the cavity. These schemes are more popular in fusion research due to radiation symmetrization and reduced sensitivity to hydrodynamic instabilities [59, 60].

The other possible scheme to generate planar shock fronts is to accelerate flyer plates by laser energy deposition on a multilayer attached to a thin flyer-foil arrangement. Results reported on Trident laser facility [61] show a typical flyer planarity of 3-10 mrad up to a flyer velocity of 7 km/s. Using indirect drive scheme, soft X-rays were also used to drive a flyer plate and to demonstrate the generation of planar shocks up to 0.75 Gbar [58]. Other than Hugoniot measurements laser with temporal ramp shaped pulses are also used to achieve quasi-isentropic

compression [61]. To generate very high pressures and to achieve conditions for inertial confinement fusion various high energy laser facilities like Trident (LANL, USA), Argus (LLL, USA), UMI 35 (USSR), Delphin (USSR), Rutherford (UK), LiMeil (France), Osaka (Japan), Shiva (LLL), Nova (LLL), and NIF (LLNL, USA) are developed worldwide.

In addition to lasers the beams of electrons, protons or heavy ions are also used for shock generation. The advantages of particle beams over lasers are longer pulse duration; better homogeneity and absence of target preheat by fast electrons [62]. Moreover heavy ion beams can generate dense plasmas near to solid density which are useful for inertial confinement fusion research [63].

1.7 Shock diagnostics

The reliability of any shock experiment depends upon the accuracy of its diagnostics. As the shock events lie from few nanosecond to microsecond, therefore special sensing schemes are employed for measurement of parameters like pressure, velocity and temperature. In this section some of these techniques, common in shock research are discussed. The conceptual details about contact type sensing pins also known as arrival time gauges, stress sensors, laser velocity interferometers and optical pyrometer will be discussed in the following subsections.

1.7.1 Contact type sensing pins

These types of sensors work on detection of shock wave arrival either by the movement of free surface, or by the ionization of compressed gas or by luminescence of shocked surfaces. The common types of sensors are electrical pins, ionization pins and fiber optic pins. The electrical pin consists of two coaxially insulated electrically charged metal electrodes. When a conducting moving surface touches the pin, the electrodes get discharged and current flows

across a resistor placed in the charging circuit, which generates a voltage spike across it. The timing of voltage spikes generated at the pins placed at known distances is recorded on an oscilloscope and is used to measure the velocity of moving surface. More sophisticated self-shorting pins [64, 65] are used, to detect the shock arrival time, where conducting surfaces are not available and shielding is required against pre-shorting by ionized gases moving ahead of the shocked surfaces. In self shorting pins, a metal cap is placed near the open ends of charged electrical pins at a very small gap (~ 50 µm); on the arrival of shock the cap moves at the free surface velocity of its material and closes the gap. Electrical pins along with self-shorting pins are very frequently used to measure the projectile velocity as well as its planarity, and shock velocity in stepped target.

In many applications where pulsed power sources are involved, these electrical pins become prone to electromagnetic noise. In such situations the use of optical fibers is quite helpful, as pins based on optical techniques do not require any electrical biasing or special electromagnetic shielding. In one type of such fiber optic pins [66], a micro balloon filled with argon gas is attached to one end of an optical fiber. When this micro-balloon interacts with the shock wave, a light flash is generated and gets recorded in the oscilloscope through a photo detector. This technique is quite sensitive, fast and immune to EM interference but requires special techniques to manufacture the micro-balloons. In some probes (Ref. 67 and other references cited therein), quartz or high density glasses are also used, which generate high shock luminescence under compression. At high pressures, the arrival of shock wave also generates a weak luminescence due to ionization of air present in the vicinity of free surface. These weak optical signals may be measured using fast and sensitive photodiodes.

1.7.2 Stress sensors

Pressure is an important parameter in shock research. In many high pressure experiments it is indirectly determined by measuring the particle velocity, but to directly measure the stresses up to 100 GPa various type of sensors have been developed. These sensors are mainly based on piezoresistive or piezoelectric effect and are normally embedded inside the target or placed near the shocked surfaces. Piezoresistive materials like Manganin, carbon, ytterbium, lithium are common for stress measurements from 0.1 GPa to 100 GPa, while piezoelectric materials like X-cut quartz, lithium niobate and PVDF (Poly(vinylidene fluoride)) are of interest for measurements up to 25 GPa. Manganin is the most widely used material since 1960's for shock research; it is an alloy of copper, manganese and nickel having reduced sensitivity of resistivity to temperature. The gauge elements are designed in various geometrical configurations from thin foils or wires of Manganin and embedded in the target material [68]. A constant current is fed to the gauge and temporal profile of voltage developed across it, is measured during shock loading. The stress profile is computed using the well calibrated data of gauge resistivity with stress. In practical situations, when loading is not purely uniaxial, a strain gauge is also placed to compensate the strain effects [69]. Though these gauges are quite popular in shock community, but their calibration at high pressures and estimation of gauge hysteresis is a difficult task. The other issue is the finite thickness of gauge element, which limits its response time.

When stresses are comparatively small, then piezoelectric sensors like x-cut quartz (~ 3 GPa) are quite commonly used. These are either placed in contact with the target or impacted directly. Being a piezoelectric material, it generates a current when its two opposite surfaces are subjected to different stress levels. It is quite useful for low stress measurements because of its large signal output, precise characterization and inherent fast response of typically less than a

nanosecond. To make it work at higher pressures, a high impedance buffer material of known Hugoniot like tungsten carbide is placed in between the quartz and target surface [65]. In parallel to x-cut quartz, lithium niobate is also used for stress measurements up to 1.8 GPa.

The gauges based on PVDF have also gained lot of interest, as these are inexpensive and can measure stresses up to 35 GPa with nanosecond response time [70]. It can also yield large signals with typical sensitivity of 23 pC /N. A lot of efforts have been made to develop PVDF films for shock applications so that gauges made by this material remain easily reproducible [71].

1.7.3 Laser velocity interferometers

The inherent sensitivity, fast response and high accuracy of optical techniques make them very useful for shock diagnostics. With the advent of lasers, many interferometric methods have been developed to measure the velocity of fast moving surfaces. These methods are based on measuring the Doppler shift in the light reflected from a moving surface, which may be the projectile, target or both. As the response time of these methods may reach near to or less than a nanosecond, the phase transition phenomenon occurring at high pressures may only be detected by such techniques. Considering the vast variety of such interferometers, a brief overview covering some of the important configurations is given here. More details may be found in cited references.

The first laser interferometer known as 'Displacement interferometer' was reported by Barker & Hollenbach [72] in 1965. In this system a Michelson interferometer was used to measure the Doppler shift in the light reflected from the moving surface, which acts as one of the mirrors of interferometer. The movement of surface causes a fringe shift, which is recorded on a

photomultiplier with velocity proportional to the fringe frequency. Due to limited frequency response of detector and recording system, the practical velocity limit of this instrument was limited to 0.2 km/s [72]. To overcome such limitation, Barker & Hollenbach made a significant improvement and developed another system known as 'velocity interferometer' [73]. In this system the Doppler shifted light is used as a source to Michelson interferometer with delay in one of the legs. Hence the Doppler shifted light is made to interfere with a delayed light signal that has been reflected from the moving surface a short time earlier. Therefore, when surface is moving with constant velocity, both light beams have the same wavelength and their beat frequency is zero. Now with this improvement the number of fringes becomes proportional to the specimen velocity and not to its displacement. But it requires that the reflecting surface must retain the mirror like finish during the motion but during shock experiments, the reflectivity of the surface deteriorates. It is further sensitive to surface tilt, hence suitable for one-dimensional motion or requires tilt-correcting mechanism such as retro-prism [74] at the specimen.

The problems related to velocity interferometer were solved by Barker & Hollenbach in their subsequently developed system, widely known as VISAR [75] (Velocity Interferometer System for Any Reflector). This system works with the light signal reflected from diffused surfaces. The intensity of light reflected from a diffused surface is quite insensitive to small rotations and tilt occurring in the reflecting surface. At the same time, the light reflected from a diffused surface lacks the spatial coherence and hence to obtain good interference fringes the path difference between two legs of Michelson interferometer should be nearly equal. To obtain fringes from the Doppler shifted light there should be a time delay in the two interfering light signals. The concept of WAMI [76] (Wide Angle Michelson Interferometer) has been invoked to meet these two apparently mutually exclusive requirements. WAMI is similar to Michelson

interferometer except one of the two mirrors is replaced by an etalon, which is polished at one side to behave as a mirror. The apparent position of mirrorized rear surface of the transparent etalon is closer to the beam splitter than its actual position, hence meets the criterion of equal length in two legs at the same time the delay is created by the motion of light in the high refractive index material of etalon. The concept of WAMI was invoked by Barker & Hollenbach in their VISAR and a transparent etalon was placed between the beam splitter and mirror of Michelson interferometer instead of rear surface mirrorized etalon.

The other important feature that has been incorporated in VISAR for improving its accuracy is to monitor the two fringe signals that are 90° out of phase. These signals are obtained in quadrature by the method of Bouricious and Clifford [77], recording of two 90° out of phase signals provides good velocity resolution and differentiate between acceleration and deceleration. A further improvement in the VISAR system has been done by Hemsing [78] to make this instrument more efficient in presence of self generated light at the target. To improve the rise time another system based on VISAR has been developed, known as Optically Recording Velocity Interferometer System (ORVIS) [79]. In this instrument, the motion of interference fringes is recorded on high-speed electronic streak camera instead on a photomultiplier tube and a rise time of 300 ps was reported.

In parallel to VISAR many researchers have worked on Fabry-Perot interferometer (FPI) to measure the Doppler shift in the light reflected from the specimen surface. It is a multibeam interferometer and the fringe diameter depends on the wavelength of the incident light. In 1968, Johnson and Burgees [74] reported the use of Fabry-Perot velocimeter (FPV) to measure the free surface velocity. They recorded the transmission of Fabry-Perot interferometer on a photodiode to measure the change in the wavelength of light reflected from the test surface. This work was

further carried out by Durand and Laharrague [80], who measured the evolution of Fabry-Perot interference fringes on a streak camera. The similar system was also developed by McMillan *et al.* [81] in which a cylindrical lens was used before Fabry-Perot interferometer to converge the interference fringes in dots for better optimization of reflected light. In 1983 Seitz and Stacy [82] has reported an experimental comparison of image intensified rotating mirror camera with the electronic streak camera. Further Goosman *et al.* [83] have reported an experimental analysis on whether the Doppler shift is affected by surface normal or not. A detailed analysis and effect of different parameters on the performance of Fabry-Perot velocimeter has been reported by McMillan *et al.* [81]. Another major development in this area is by Goosman *et al.* [84], who developed a multibeam Fabry-Perot velocimeter to simultaneously measure the velocity profile at five points on a moving surface. To make this development more economic and less complex a dual beam velocimeter [85] is developed and will be discussed in detail in next chapter.

In recent years new interferometeric techniques [86, 87] based on telecommunication based fiber optic components have emerged as compact and alignment free solution for shock measurements. In these systems an optical coupler is used to mix the Doppler shifted light with the original laser light and to generate a beat effect. The beat frequency is recorded using fast photodiode and electronic digitizers. As the free surface velocity information is decoded from the beat frequency analysis, therefore this system can work at low laser powers. In different configuration this heterodyne technique is known as Photon Doppler Velocimeter (PDV) [87] or All Fiber Displacement Interferometer [88], or in another VISAR like configuration this is also named as All Fiber Velocimeter [89].

1.7.4 Optical pyrometer

Temperature is an important parameter to determine the thermodynamic state of any shock compressed material. The measurement of temperature is frequently used to detect the melting under shock compression. Optical pyrometers work on the principal of Planck's radiation law, which states that, the spectral radiance (radiation power emitted per unit area per unit solid angle) from a grey body at temp T and wavelength λ is given by:

$$N\ (\lambda)\ = \varepsilon.\ C_1.\ \lambda^{-5}\ [\exp\ (C_2/\lambda T) - 1]^{-1} \tag{1.14}$$

Where C_1 and C_2 are constants while 'ε' is the emissivity of the radiating surface. By measuring the radiance at multiple wavelengths it is possible to numerically fit the Plank's law to deduce the temperature of shocked surface. In practical systems the radiation collected from the shocked surface is divided in different parts using beam splitters and narrow band optical filters [90, 91]. The output after filters is focused on photodiodes to measure the signals proportional to the radiance at various wavelengths. The crucial task in such systems is its calibration, which is done with a known radiation source like Quartz-Tungeston-Halogen lamp and removal of any spurious noise signals recorded in the photodiode signals.

In addition to above described methods there are various other important techniques that are used to measure the material characteristics under shock loading. Some of such advanced techniques are flash X-ray radiography [92] to record the dynamic movement of surfaces as well to indentify fractures; *in-situ* x-ray [93] to determine kinetics of phase transition, particle velocity gauges based on electromagnetic induction principle [94], and fast optical photography using streak or fast framing camera.

1.8 Plan of the thesis

The present thesis is organized in six chapters. Basics of shock physics and introductory concepts of various shock generating techniques as well as diagnostics are discussed in this chapter (Chapter 1). Chapter 2 will elaborate the pulsed power aspect of electrically exploding foil accelerator technique along with technical details and capabilities of electric gun setups developed in our laboratory. Later the description of empirical formulation known as electrical analogue of Gurney relation, and details about one dimensional numerical hydrodynamic scheme for prediction of flyer velocity are elaborated. The pulsed power switches developed for high voltage and high current applications like PCB based spark gap switch and plasma motion based crowbar switch are also discussed in this chapter. The diagnostics involved in shock experiments like magnetic pick up coil for foil current measurements, fiber optic pins for shock velocity measurements, Fabry-Perot velocimeter for particle velocity measurements and its dual beam version are also covered in the last section of this chapter.

Chapter 3 covers the optimization studies carried out on electric gun setup to enhance its performance. This chapter includes the effect of foil dimensions, ambient pressure, current rise time, barrel length and its diameter on flyer velocity profile. The optimization includes the enhancement of flyer velocity by plasma propulsion effect, using barrels of diameter less than the foil size. This chapter also discusses about the concept of two stage exploding foil assemblies. The detailed analysis of these measurements will be presented in this chapter. In the last part we have included the results of one dimensional hydrodynamic numerical simulations on our capacitor banks as well as on other reported systems and shown the effect of return conductor on the final flyer velocity.

Chapter 4 includes the impact studies carried out on various metals like tantalum, iron, tin, copper, and aluminum etc. These experimental measurements demonstrate the capabilities of present electric gun setup along with Fabry-Perot velocimeter. First the experiments carried out to measure the flyer velocity and its planarity are described and later shock studies carried out with single beam Fabry-Perot velocimeter to record the velocity profile of target-glass interfaces are discussed. In these experiments flyer velocity was assumed from the many repeatable and reproducible measurements carried out under similar conditions. Pressures up to 70 GPa were achieved on tantalum targets in these studies and are reported in this chapter. The results of shock velocity measurements in stepped targets of copper and tantalum at 23 GPa and 48 GPa respectively using in-house designed fiber optic shock arrival pins are also presented in last section of the chapter.

Chapter 5 covers the experimental studies carried out on zirconium and titanium metals using dual beam velocimeter where two velocities were simultaneously measured. The details of experimental results and phase transition detected in velocity profiles will be elaborated here. The techniques used to improve the measurement accuracies using common streak record are also discussed in this chapter.

The summary of the research work carried out in present thesis is described in the last chapter (Chapter 6). This chapter provides significant outcomes of experimental results and the possibilities for future research on portable electric gun setup at enhanced pressures. This chapter includes the work highlights showing the potential of low energy electric gun setup along with dual beam FPV for high pressure research in small laboratories. These highlights mainly include the determination of polymorphic phase transition in iron, zirconium and titanium metal foils

under shock loading and generation of peak pressure up to 70 GPa in tantalum metal foils. A list

of references used in this thesis is provided at the end.

Chapter 2

Electrically Exploding Foil Accelerator: Experimental Setup and Numerical Schemes

This chapter focuses on electrically exploding foil accelerator technique and related diagnostics developed for the measurement of equation of state of different materials. To systematically discuss the details of these techniques, this chapter is divided in three parts; the first part provides a brief introduction and working principle of electrically exploding foil accelerator technique and details of experimental setup developed in our laboratory. In this part description of electrical analogue of Gurney formulation to compute the final flyer velocity is also discussed. In second part the diagnostics involved in shock experiments like magnetic pick up coil for foil current measurements, fiber optic pins for shock velocity measurements, Fabry-Perot velocimeter for particle velocity measurements and its dual beam version to measure velocities of two surfaces are elaborated. The details of a one dimensional hydrodynamic numerical scheme used to predict the velocity profile of flyer accelerated by foil explosion is also given in present chapter. In the last part of this chapter, description of a high coulomb rating plasma motion based crowbar switch is provided, which is useful for extending the life of capacitors as well as in applications like rail gun, where crowbar is desired to enhance its efficiency.

2.1 Introduction

Electrically exploding foil accelerator or electric gun has long been used by many leading research groups [95-97] for impact studies of materials up to TPa regime [33]. Due to its less complex operations and requirement of small quantity of target material, recent research interest is shifted towards low energy portable systems [97, 98]. With careful design considerations these small systems can also accelerate small flyers up to a velocity of 10 km/s [97], which makes this technique comparable to other complex techniques like gas gun or explosives. In contrast to later two techniques, the flyer accelerated by electric gun has a smaller impact area, which restricts the simultaneous measurement of many shock parameters in a single experiment like flyer planarity/ asymmetry, flyer / target velocities and results in relatively inferior accuracies. But still this technique has gained lot of attention, as experiments can be carried out easily in small laboratories without any need of special arrangements and with the help of dedicated diagnostics it can generate valuable data at very high pressures.
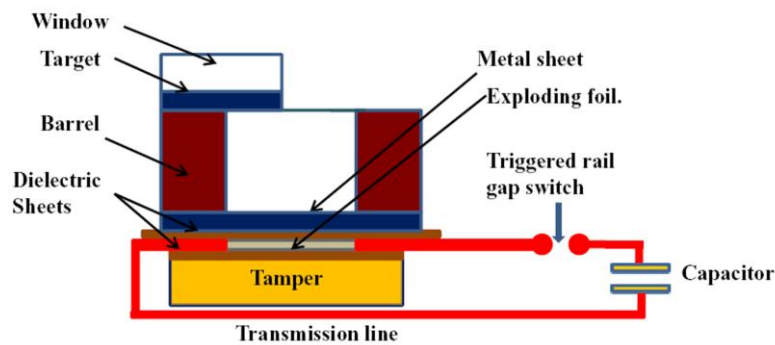
Fig. 2.1: Schematics of electrically exploding foil accelerator (electric gun), showing the experimental configuration with a target placed on top of the barrel. A layer of metal sheet is also bonded over the dielectric flyer to enhance its shock impedance.

In electrically exploding foil accelerator (also known as electric gun), a thin metal foil is exploded by fast electrical energy deposition. If the energy deposition time is sufficiently small than the heat diffusion time away from the foil; then the energy densities in foil may significantly cross the energy densities of common chemical explosives and may reach up to 20-30 kJ/g. Such super high energy densities leads to very high pressures ($\leq$ 10-20 GPa), and accelerate the projectile in small size barrels. To practically achieve fast energy deposition rates and high energy; low inductance capacitor banks are normally utilized, which are connected to exploding foil assemblies through a triggered spark gap switch. The schematic diagram of electric gun is shown in Fig. 2.1. The exploding foil assembly is made of a thin metallic bridge foil which is sandwiched in between two dielectric sheets and backed by a heavy tamper on one side and an appropriate size barrel on the other. The foil explosion generates a high thermodynamic pressure which forces the dielectric sheet to punch out around the periphery of barrel and accelerates it to suitable high velocities.   The flow of current through the exploded metal plasma and its interaction with the magnetic field also give rise to an additional Lorentz force (**J x B)**, which further enhances the flyer velocity. The material under study (target) is bonded to a suitable transparent window with a thin layer of adhesive. The target assembly is then placed over the barrel in such a manner that it covers only half the barrel area, leaving other half for measurement of flyer velocity. The transparent window of known Hugoniot is helpful in maintaining the planarity of the target as well as in measuring the equation of state of target material. The velocity of the flyer may be varied by charging the capacitor at different voltages. The amplitude of shock pulse generated in the target is decided by its material as well by flyer material and its velocity. To enhance the shock pressures, sometimes a thin sheet of metal with high shock impedance is also bonded over the top of dielectric sheet (flyer). As normally the

thickness of the flyer is much smaller than its diameter, hence the duration of shock pulse is governed by the arrival of release waves from its back free surface.

The bridge foils are normally made in square shapes with cross-section decided by the capacitor bank current and its rise time by following relation:

$$A = \int_0^{t_B} J^2 dt \tag{2.1}$$

Here 'J' is the current density, 't_B' is the burst time or the time at which foil explosion takes place. While 'A' is an empirical constant for a given material known as Action Integral and for aluminum it has a value of 6.0 x 10^{16} $Amp^2.m^{-4}.s$ [99]. Considering the capacitor bank and foil assembly as a LCR circuit, the current profile I (t) can be considered as damped sinusoidal and may be expressed as:

$$I(t) = I_0 \sin(\omega.t).\exp(-R.t/2L) \tag{2.2}$$

In above relation 'R', 'L' and 'ω' are the resistance, inductance and angular frequency of the LCR circuit respectively. While $I_o = V_0/ (L.\omega)$, where V_0 is the initial (at t = 0) charging voltage on capacitor bank. Assuming low losses in the circuit, which is normally the case with most of the practical systems, the exponential damping factor may be dropped up to first current peak without introducing any significant error and current profile may be written as:

$$I(t) = I_0 \sin(\omega.t) \quad \text{or} \quad J(t) = J_0 \sin(\omega.t) \quad \text{where } J_0 = I_0 / a \tag{2.3}$$

Here 'a' represents the cross-sectional area of the foil. Now by substituting the value of 'J' in Eq.2.1, a transcendental relation can be obtained between action integral and foil cross-section.

$$t_B - \left(\frac{2A}{J_0^2}\right) = \frac{\text{Sin}(2\omega.t_B)}{2\omega}$$

(2.4)

For a known value of J_0 and action integral this equation can be solved graphically or numerically to estimate the value of t_B for a given foil cross-section.

2.2 Electrical analogue of Gurney formulation

In case of low energy banks, where acceleration by magnetic force is comparatively small, an empirical formulation known as Gurney relation may be used to estimate the final flyer velocity. Electrical analogue of Gurney model [100] relates the projectile velocity, 'v_F' to the flyer mass per unit area 'M', exploding foil mass per unit area 'C', and current density of the foil at the time of burst 'J_B', according to following equation:

$$v_F = \frac{K.J_B^n}{\sqrt{\left(\frac{M}{C} + \frac{1}{3}\right)}}$$

(2.5)

Here K & n are empirical constants and determined by the fitting of experimental data in to above relation. This formulation indicates that to achieve higher flyer velocities, the burst current density should be high and the ratio 'M/C' should be as small as possible. To decide an optimized foil material a comparative study has been reported [29] on thirteen materials, and it was found that aluminum is the best practical material to achieve higher flyer velocities. It has also been reported earlier that the rate of current rise has strong influence on flyer velocity [101],

so even capacitor banks with lesser energy but faster rise times can accelerate small flyers to high velocities. Other parameters which affect the flyer velocity are barrel length, its diameter and mass of the flyer. The effects of these parameters on flyer performance have been studied in this work and are reported under optimization studies in next chapter.

The Gurney model is good for simplistic parametric studies but this model does not take care of time dependent energy deposition as is the case with exploding foil experiments and unable to predict the velocity histories with time. Temporal profile of flyer can be numerically obtained either by using prior knowledge of experimental power curves of capacitor bank [102] or by performing more intensive hydrodynamic simulations [98, 103, 104] which has also been carried out in present work and reported later in this chapter.

2.3 Electrically exploding foil setup

To study equation of state of various materials an 8 kJ exploding foil accelerator (ELG-8) is designed to accelerate planar projectiles of diameter 6 mm to 10 mm, up to a velocity of 6.2 km/s. In addition to this setup another very compact printed circuit board based setup is also designed to accelerate small projectiles (diameter ~3mm) to a velocity of 1.6 km/s. This miniaturized design is helpful for applications where remote single shot operations are desired. These devices with their features are discussed in following subsections:

2.3.1 ELG-8 system

This electrically exploding foil setup is designed to be a portable one. It consists of an 11 µF capacitor with a maximum charging voltage of 40 kV, connected to a parallel plate transmission line through a triggered rail gap switch (Fig. 2.2). Two large width transmission lines with 2 mm thick Mylar insulation between them are kept on a movable trolley to form the
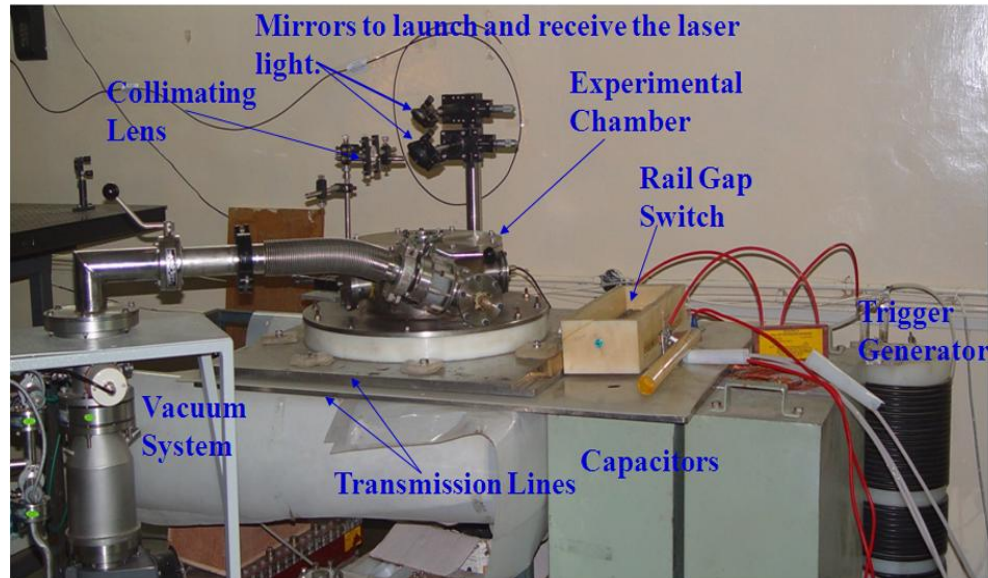
Fig. 2.2: Photograph of experimental setup.

basis for this system. The lower transmission plate is little longer in length and extends up to

capacitor's ground terminal. The top transmission plate is connected to a rail gap type triggered

spark gap switch which rests over the extended ground transmission line. The other end of the

spark gap is connected to the high voltage end of the capacitor. A central square opening is

provided in the top transmission line for carrying ground connections from the bottom

transmission line with proper insulation and vacuum sealing. An arrangement is made over the

transmission line to mount exploding foil sandwiches inside the chamber keeping the barrel

pressed by a spring loaded assembly. A circular chamber of diameter 300 mm and having four

windows for optical and electrical probing is fixed over the top transmission line over a 40 mm

thick nylon insulation ring in between. An arrangement has also been made over the chamber

base to mount the optical assemblies for velocity measurements using FPV. Though most of our

experiments are performed at atmospheric pressure, a port is also provided in the experimental

chamber to evacuate it up to 10^{-4} mbar pressure depending on the experimental needs, one more

port is provided to insert optical fibers through a vacuum interface.
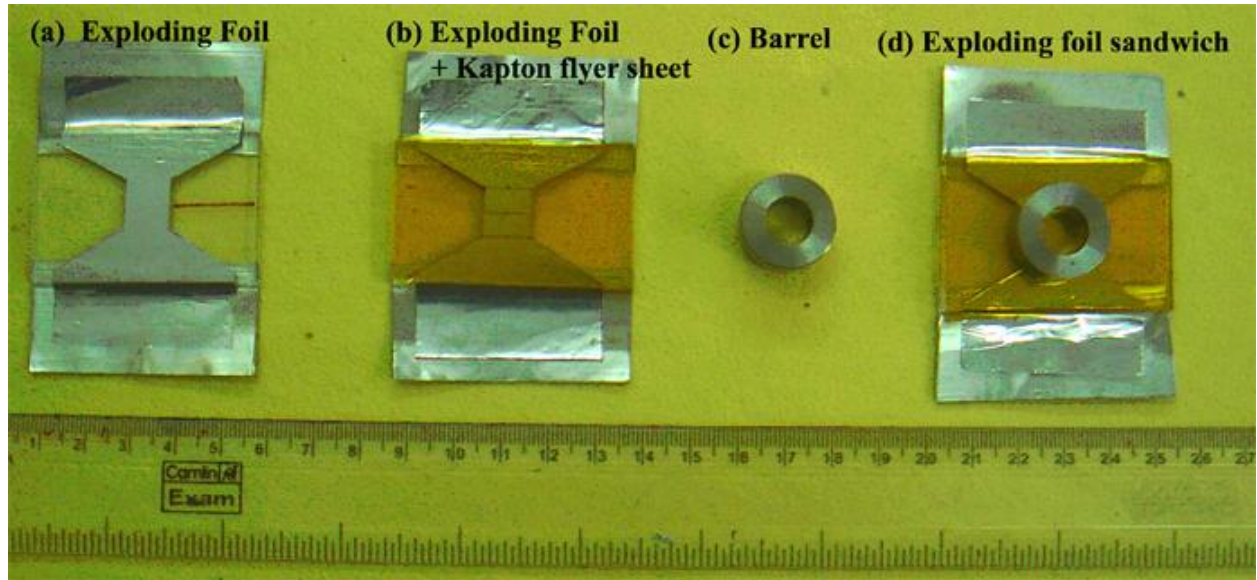
Fig. 2.3: Photograph of exploding foil assembly.

The charging unit for this system is designed in a separate movable trolley with a

handheld control panel connected to it by a 15 meters long cable. To initiate multichannels in the

rail gap switch, a cable based double Blumlein trigger pulse generator is used, which can

produce a 100 kV pulse of 30 ns rise time in an open load with a charging voltage of 25 kV.

The exploding foil sandwiches are prepared from a 25 μm thick aluminum foil (99.99 %

pure) in geometry such that a central square piece forms the most resistive part of the circuit, and

rests on a 2 mm thick Perspex tamper as shown in Fig. 2.3 (a). A 125 μm thick Kapton or metal

bonded Kapton sheet is placed on top of this metallic foil (Fig. 2.3 (b)). A barrel made of steel

with a hole of diameter less than or equal to exploding foil dimensions is then fixed over this

arrangement with proper alignment (Fig. 2.3 (d)). The dimentions of exploding foil are decided

so as to explode it before the current peak for optimum utilization of bank energy. The time

period of this system under short circuit conditions has been found to be 7.5 μs with a voltage

reversal factor of 0.82. The typical parameters of this system are listed in Table 2.1. This electric

gun setup has been optimized to achieve flyer velocities from 1.5 km/s to 4.5 km/s on 6 mm

diameter aluminum-polyimide composite flyers and up to 6.2 km/s on polyimide (Kapton) flyers.

Table 2.1

Electrical Parameters of Electrically Exploding Foil Accelerator (ELG-8)

Setup

S. No.	Parameters	Value
1.	Capacitance:	11 μF
2.	Inductance:	130 nH
3.	Charging Voltage:	40 kV
4.	Voltage Reversal Factor:	0.82
5.	Peak Current (Max)	300 kA
6.	Time Period:	7.5 μs

The diagnostics involve the measurement of current using an in situ calibrated pick-up

coil placed below the exploding foil assembly; the direct and integrated output of this loop are

recorded on an oscilloscope. The major diagnostic of this set up is a Fabry-Perot velocimeter

which is designed to record velocities in the range of 0.2 to 10 km/s with an estimated resolution

of 0.2 km/s. As will be discussed later in this chapter, with modifications it is possible to

measure velocities of two surfaces on a single streak record for precise EOS measurements.

2.3.2 Miniaturized electric gun setup

This is setup is completely designed over a commercially available double sided glass epoxy based printed circuit boards (PCB). The main feature of this design is a PCB based triggered spark gap, which is integrated to the electrically exploding foil setup fabricated on same PCB. If a compact capacitor is also mounted on the PCB then this integration makes this device a standalone system, which can be kept away from the bulky power supply. Considering the importance of spark gap switch, it will be discussed first and later the exploding foil assembly will be discussed.

2.3.2.1 Switch design

This switch is a surface discharge type rail gap switch, which has been chemically etched out from a commercially available double sided
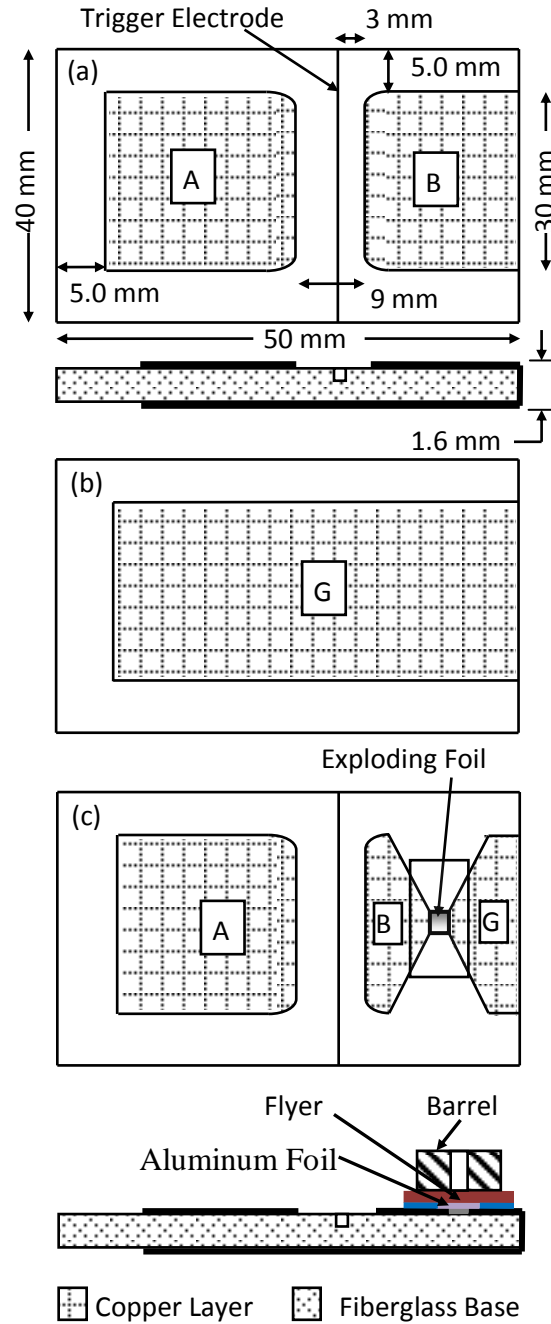
Fig. 2.4: Schematic view of PCB based rail gap switch and exploding foil assembly.
(a) Top view (b) Bottom view (c) Exploding foil on modified geometry of electrode 'B'.
A = HV Electrode; B= Top Ground Electrode G = Bottom Ground Electrode connected to 'B' by a copper strip soldered at both sides.

copper coated fiberglass board commonly used for making printed circuit boards (PCB's). For the clarity of presentation hereafter we will refer this etched board as PCB. This design has advantage that it can directly be integrated with the strip transmission lines etched over the same PCB. Such a designed switch may be used for low energy pulsed power applications, where high voltage and low currents are involved or for single shot applications involving high currents.

The spark gap has been designed over a small rectangular piece of a double-sided copper clad fiberglass epoxy board. The design of spark gap is schematically shown in Fig. 2.4. Figure 2.4(a) shows the top and side view of the switch where two electrodes have been formed by chemically etching out a 9 mm wide copper strip from one side of the PCB. Copper layer at back has been left intact to make the path for return current (Fig. 2.4 (b)). To avoid surface flash-over near the edges a 5 mm wide copper layer has also been etched out at both sides of the PCB. Trigger electrode was made from a copper wire of diameter 200 μm placed in a shallow groove created near and parallel to one of the electrodes. This arrangement is implemented to avoid direct contact of trigger electrode with the main discharge plasma. The edges of electrodes were rounded to avoid high field points near the spark gap geometry. Three RG-58 cables were used to connect the spark gap to the capacitor bank. Electrode 'A' is connected to the high voltage end of capacitor while electrode 'B' is connected to the ground through electrode 'G'. To complete the circuit, electrode 'B' and electrode 'G' are shorted by a copper strip soldered to both electrodes at one side of the PCB.

To study the electrical behavior of present switch, six such rail gaps have been prepared with similar design parameters. Electrode gap was kept 9 mm and trigger electrode was placed at a gap of 3 mm from the ground electrode. These design parameters are decided for applications requiring switching at 5-6 kV. Measured self breakdown and the minimum voltage at which gap

can be closed by application of trigger pulse (20 kV with 20 ns rise time) are given in Table 2.2. Large variations observed from one spark gap to other especially for spark gap-2 and 3 might possibly be due to small irregularities left in the copper electrodes because of poor control over chemical etching process. Even with these large variations, these rail gaps can suitably be used for 5 kV applications due to its large switching range (3~4 kV). With this wide operating range the jitter of the switch has been found to be about 4 to 10 ns and gap closing time of 5 ns [105].

Table 2.2

Experimental Results Obtained on PCB Based Spark Gaps.

	Minimum Triggerable Voltage (kV)	*Self Breakdown Voltage (kV)*
Rail Gap-1	3.5	7.9
Rail Gap-2	5.5	7.7
Rail Gap-3	4.40	7.48
Rail Gap-4	2.9	6.9
Rail Gap-5	2.5	6.73
Rail Gap-6	3.7	7.1

2.3.2.2 Exploding foil integration

To accommodate exploding foil over the same PCB the geometry of electrode 'B' has been modified and is shown in Fig. 2.4 (C). A 3x3 mm^2 wide square gap has been created in the electrode 'B', and bridged by a 6 µm thick aluminum foil. A 125 µm thick sheet of Kapton is placed over it as a flyer sheet. A barrel made out of aluminum with a circular hole of diameter 3.0 mm is placed over the Kapton sheet to guide the flyer after foil burst. This whole assembly is

then connected to a low inductance capacitor bank using three RG-58 cables as shown in the photograph of the assembly (Fig. 2.5).

After initial calibrations of switch, experiments have been carried out on an electric gun assembly that uses a 0.9 µF capacitor bank. A maximum velocity of 1.6 km/s has been achieved on Kapton flyers of diameter 3.0 mm and thickness 125 µm on this compact system. In this system the bulkiest part is capacitor bank, chosen because of its availability. This can be replaced with a still compact one such that it can directly be placed over the PCB structure without using any coaxial cables.
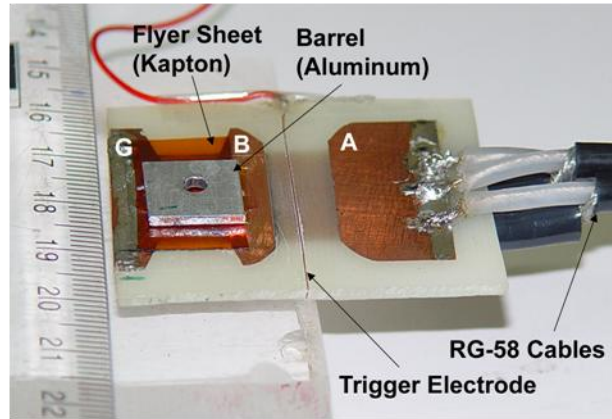
 Fig. 2.5: Photograph of exploding foil assembly integrated to PCB based rail gap switch. (Exploding foil is placed below the flyer sheet and not visible in this photograph).

2.4 Diagnostics

The diagnostics involve the measurements of electrical parameters like pulse voltage and current as well as flyer and particle velocity measurements using optical techniques. To measure the pulsed voltages across the exploding foil, a standard resistive divider based Tektronix make P6015A probe [106] is used. While an *in-situ* calibrated pick-up loop is utilized for current measurements and will be discussed in next subsection. The main shock diagnostic is an in-

house developed Fabry-Perot velocimeter, which along with its modified dual beam version will

be discussed in the later part of this section. The basics about fiber optic pins used to detect the

breakout of shock front from free surfaces will also be covered towards the end.

2.4.1 Magnetic pick-up coil

The magnetic pick-up coil works on Faraday's law of magnetic induction, and it consists

of a small wire loop placed near to a current carrying conductor. The magnetic flux linked to the

wire loop changes as per the variations in main conductor current leading to an induced voltage

across its ends proportional to the rate of change of flux. The integration of this voltage may

provide a signal proportional to the current flowing through the main conductor. The schematic

and typical circuit for a pick-up coil is shown in Fig. 2.6. Here $d\phi/dt$ and 'L' represent the

induced voltage and inductance of pickup loop respectively, while 'R' and 'C' are the resistance

and capacitance of integrator circuit.
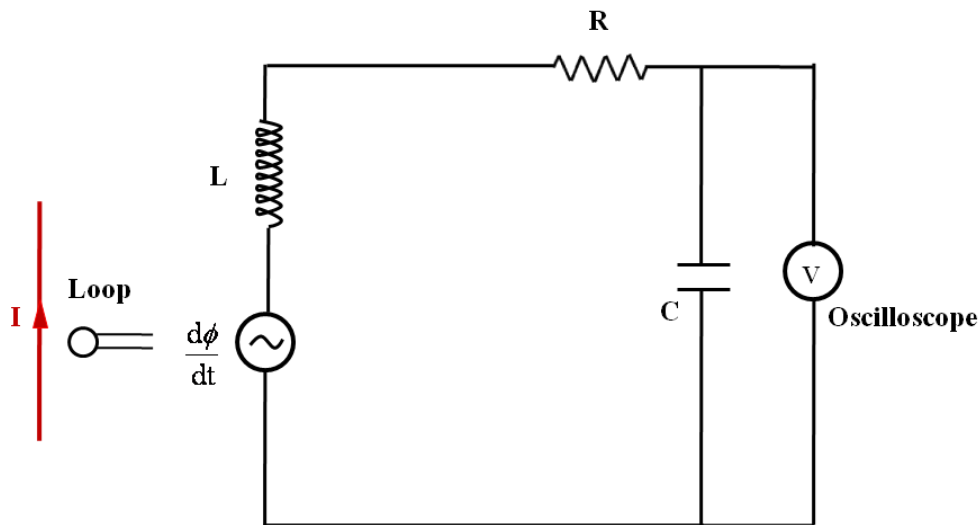
Fig. 2.6: Equivalent circuit diagram of magnetic pick-up coil.

Considering the circuit shown in Fig.2.6, it is possible to write the voltage balance equation as:

$$\frac{d\varphi}{dt} = L\frac{di}{dt} + iR + \frac{1}{C}\int_0^t i\,dt \tag{2.6}$$

If loop is designed such that R>> Lω and t<<RC then first and third terms on the right side of above equation may be neglected in comparison to middle term. Here 'ω' is the highest frequency involved in the signal. Under these assumptions the voltage across the capacitor may be derived as [107]:

$$i \approx \frac{1}{R}\frac{d\varphi}{dt}$$
$$V = \frac{1}{RC}\int_0^t \frac{d\varphi}{dt}\,dt = \frac{\varphi(t)}{RC} \propto I(t) \tag{2.7}$$

As the flux associated with the loop is dependent on its relative position from the main conductor and its orientation, therefore it should be placed at a fixed location after calibration.

In our setup a square loop of area 20 x 20 mm^2 with two turns is placed near the tamper of exploding foil at a fixed location. The inductance of this loop is around 300 nH, and it is coupled to an RC integrator of 100 μs time constant. The R and C of this integrator are 20 kΩ and 5 nF   respectively and satisfies the Eq. 2.7. To calibrate this loop, the exploding foil is replaced with a thick copper strip of similar shape. The capacitor bank is charged to a certain voltage (~16 kV) and discharged in to the short circuit load; the integrated loop output is recorded in the oscilloscope and its peak value is compared with its theoretical value calculated by following relation for under-damped circuits [108].

$$I = V_{CH}\sqrt{\frac{C}{L}}.k \qquad\qquad (2.8)$$

In this relation 'V_{CH}' is the charging voltage of capacitor and 'k' is the voltage reversal factor, calculated as the average of the ratio of consecutive current peaks recorded in the oscilloscope. The calibration factor obtained by this analysis is used to calculate the current in exploding foil experiments. In ELG-8 system this calibration factor was found to be 115 kA/V.

2.4.2 Fabry-Perot velocimeter

Fabry-Perot velocimeter is a well known technique in shock research. It measures the Doppler shift in the light reflected from a moving surface by recording the change in diameter of interference fringes of a Fabry-Perot interferometer on a streak camera. To understand the fundamentals of velocimeter it is necessary to consider Fabry-Perot interferometer first. It basically consists of two partially reflecting plane surfaces maintained parallel and separated by
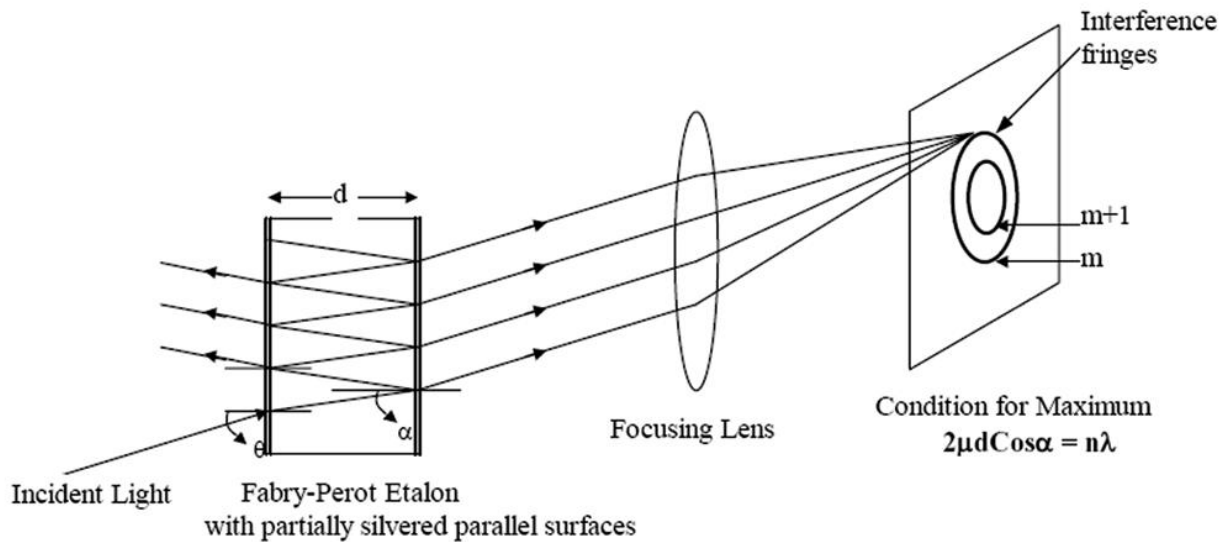
Fig. 2.7: Fringe formation in Fabry-Perot interferometer.

a distance 'd', when this distance is kept fixed, it is known as etalon. Fig.2.7 shows a Fabry-Perot etalon made of an optical material of refractive index 'μ'. A light wave entering through one of the mirrors will undergo multiple reflections inside the system so that light leaving the second mirror will consists of a series of parallel beams as shown in Fig. 2.7. These parallel light rays are brought to a common point at the focus of a lens, where they can interfere. The bright fringes produced by this multiple beam interference are narrower in comparison to the fringe spacing of those produced in two beam interferometers.

The output intensity of a Fabry-Perot interferometer follows the Airy pattern [109, 110] and is given by following relation:

$$\frac{I_t}{I_i} = \frac{1}{1 + \dfrac{4R}{(1-R)^2} \operatorname{Sin}^2(\delta/2)}$$

(2.9)

$$\text{where} \quad \delta = \frac{4\pi}{\lambda}\mu d \operatorname{Cos}\alpha$$

(2.10)

Here I_t and I_i are the intensities of transmitted and incident light, δ is the phase difference between two adjacent interfering light beams, 'R' is the reflectivity of partially reflecting surfaces of Fabry-Perot etalon and 'μ' is the refractive index of the material present between two reflecting surfaces.

There are two crucial parameters of a Fabry-Perot interferometer, one is Finesse and other is Free Spectral Range (FSR). Finesse (F) is a measure of sharpness of the fringes and is given by the ratio of fringe spacing (2π) to the width of a bright fringe at half maximum.

$$F = \frac{\pi\sqrt{R}}{1-R}$$

(2.11)

Higher the finesse sharper will be the fringes. FSR is the wavelength separation of two wavelength components present in the source at which m^{th} order fringe of one wavelength will start overlapping with the $(m+1)^{th}$ order of the other and is given by following relation:

$$FSR = \frac{\lambda^2}{2\mu d} \tag{2.12}$$

The minimum wavelength separation that can be resolved by FPI using Lord Rayleigh's [110] criterion for resolving two equal-irradiance overlapping slit images is given by the following relation:

$$(\Delta\lambda)_{min} = \frac{FSR}{Finesse} \tag{2.13}$$

The diameter of the interference fringes depends upon the wavelength of incident light and can be calculated as follows: A bright fringe of mth order occurs when phase shift δ becomes a multiple of 2π, i.e.

$$\delta = \frac{4\pi}{\lambda} \mu d Cos\alpha_m = 2m\pi \tag{2.14}$$

$$\Rightarrow \qquad m = \frac{2\mu d Cos\alpha_m}{\lambda} \tag{2.15}$$

If α is small $\qquad Cos\alpha_m = 1 - \frac{\alpha_m^2}{2} \tag{2.16}$

$$\Rightarrow \qquad \alpha_m = \pm\sqrt{2 - \frac{m\lambda}{\mu d}} \tag{2.17}$$

If the focal length of the lens placed after Fabry-Perot interferometer is 'f' then the diameter of a bright fringe corresponding to m^{th} order is given by following relation:

$$D_m^2 = 4f^2\theta_m^2 = 4f^2\alpha_m^2\mu^2 \tag{2.18}$$

Here we have taken the approximation that for small values of 'α',

$$\theta = \mu\alpha \tag{2.19}$$

$$\Rightarrow \quad D_m^2 = 4f^2\mu^2\left(2 - \frac{m\lambda}{\mu d}\right) = 4f^2\mu\frac{\lambda}{d}\left(\frac{2\mu d}{\lambda} - m\right) \tag{2.20}$$

Let us define: $\dfrac{2\mu d}{\lambda} = n + \varepsilon$ (2.21)

Here 'n' is an integer and corresponds to the order of innermost bright fringe and 'ε' is the fractional part. The significance of 'ε' can be understood if we assume a particular situation where $\varepsilon=0$, then the above equation gives the condition for maximum at center i.e. at $\alpha = 0$. In most of the cases 'ε' has certain finite value; hence instead of getting a bright dot at center, an interference fringe of finite diameter is observed and the value of 'Cosα' for the innermost bright fringe (nth order) is given by following relation:

$$Cos\alpha_n = \frac{n}{n + \varepsilon} \tag{2.22}$$

Using Eq. 2.20 and Eq. 2.21 following relation can be obtained for m[th] order fringe diameter:

$$D_m^2 = 4f^2\mu\frac{\lambda}{d}(n + \varepsilon - m) \tag{2.23}$$

Introducing another integer: $j = n-m$

$$D_j^2 = 4f^2\mu\frac{\lambda}{d}(j + \varepsilon) \tag{2.24}$$

The order of interference fringes decreases as one moves away from the center and for a given wavelength highest order corresponds to innermost bright fringe, hence $j = 0$ represents the innermost central bright ring and $j = 1$ represents the next bright fringe. Here it may be noted that ε is a quantity, which is independent of j and can be determined by the interception of the d^2 versus j curve. If large number of fringes are not available then it can be determined using Eq. 2.24 for $j = 0$ & 1.

$$\varepsilon = \frac{D_0^2}{D_1^2 - D_0^2} \tag{2.25}$$

Where

$$D_1^2 - D_0^2 = 4f^2 \mu \frac{\lambda}{d} \tag{2.26}$$

Here it may be noted that the value of $D_1^2 - D_0^2$ remains nearly constant with small changes in wavelength, as these changes are generally very small at all practical values of velocities. If we consider a velocity of 10 km/s, the Doppler shift in the wavelength is 3.5×10^{-2} nm, which will cause a relative change of the order of 10^{-5} in the value of $D_1^2 - D_0^2$, that can be neglected without making any significant error in the velocity measurement.

The relativistic Doppler shift in the light reflected from a surface moving with velocity 'v' is given by following relation:

$$\frac{\omega_R}{c} = \frac{\omega_L}{c} \left[1 + \beta (\cos\theta_L + \cos\theta_R) \right] \tag{2.27}$$

Here $\beta = v/c$, and subscript 'L' and 'R' refer to incident (laser) and reflected light respectively. 'θ_L' and 'θ_R' are the angles made by laser light and reflected light with the surface normal. In terms of velocity (v) the above expression can be written as:

$$v = \left(\frac{c.\lambda_L}{Cos\theta_L + Cos\theta_R} \right) \cdot \left(\frac{1}{\lambda_R} - \frac{1}{\lambda_L} \right) \tag{2.28}$$

Substituting the values of λ_L and λ_R from Eq.2.21:

$$v = \left(\frac{c.\lambda_L}{2\mu d} \right) \left(\frac{1}{Cos\theta_L + Cos\theta_R} \right) \cdot \left((n_R + \varepsilon_R) - (n_L + \varepsilon_L) \right) \tag{2.29}$$

$$\Rightarrow \quad v = \left(\frac{c.\lambda_L}{2\mu d} \right) \left(\frac{1}{Cos\theta_L + Cos\theta_R} \right) \cdot \left((n_R - n_L) + (\varepsilon_R - \varepsilon_L) \right) \tag{2.30}$$

$$\Rightarrow \quad v = \left(\frac{c.\lambda_L}{2\mu d} \right) \left(\frac{1}{Cos\theta_L + Cos\theta_R} \right) \cdot \left((i + (\varepsilon_R - \varepsilon_L)) \right) \tag{2.31}$$

Here 'i' represent the total number of fringes moved out from the center of the fringe pattern. In a pattern with no discontinuous jump it can be determined from the number of new fringes that have appeared. If appropriate number of fringes are available then the value of 'ε' can be measured by the intercept of D^2 vs. j curve, otherwise it can also be calculated by substituting the values of ε_R and ε_L from Eq.2.25

$$v = \frac{c\lambda_L}{2\mu d} \left(\frac{1}{Cos\theta_L + Cos\theta_R} \right) \left(i + \frac{D_{R_0}^2 - D_{L_0}^2}{D_{L_1}^2 - D_{L_0}^2} \right) \tag{2.32}$$

The above equation is derived under assumption that the value of $D_1^2 - D_0^2$ remains constant with small changes in wavelength. This equation provides a relation between velocity of

the projectile and fringe diameter, hence if fringe diameters are known at different time instances, velocity profile can be obtained by this relation. There are two cases of special interest. The first is $\theta_L = \theta_R$ and second is of normal incidence, i.e. $\theta_L = \theta_R = 0$, Later case is frequently encountered in velocimetry, when the laser is launched perpendicular to the target surface, and the equation for Doppler shift can be derived by just putting $Cos\theta = 1$ in above equation.

$$v = \frac{c\lambda_L}{4d\mu}\left(i + \frac{D_{R_0}^2 - D_{L_0}^2}{D_{L_1}^2 - D_{L_0}^2}\right) \tag{2.33}$$

The constant $(c.\lambda_L / 4d\mu)$ is known as fringe constant and for a given 'd' it decides the number of fringes that will emerge out from the centre for a given velocity change. The detailed theoretical description of F.P. velocimeter may be found elsewhere [81].

2.4.2.1 Selection criterion for Fabry-Perot velocimeter

As discussed earlier, there are two characteristic parameters of a Fabry-Perot interferometer (FPI) one is finesse and other is FSR. Finesse decides the sharpness of the interference fringes, therefore if finesse is high, the width of rings will be narrower and it will be easier to find the peak position and to discern the small changes in it. In practice the width of the peak is also influenced by the spatial resolution of streak camera. So there is no practical advantage in making the width of the rings narrower than the spatial resolution of streak camera. With high finesse, the peak transmittance of FPI also decreases, so these two factors are required to be taken into account while deciding the finesse of FPI. The finesse of a Fabry-Perot interferometer is ideally decided by the reflectance value of its mirrors as given by Eq. 2.11 but there are other practical parameters which degrade its value like flatness of the mirrors,

parallelism between two mirrors, phase difference introduced by reflection coatings and other micro defects present in the imperfectly polished plates. Hence an optimization is required for finesse calculation, taking into account all the above-mentioned parameters.

Theoretically a relation can be established between finesse (F) and separation between the FPI mirrors (d), if we know the minimum detectable wavelength change ($\Delta \lambda$) due to Doppler shift using Eq. 2.13.

$$\Delta\lambda_{\text{Min}} = \frac{\lambda^2}{2\mu.\text{d}.\text{F}} \tag{2.34}$$

This finally decides the minimum velocity that can be measured by FPV as per following relation derived from Eq. 2.28 under the assumption of $\theta_L = \theta_R = 0$.

$$v_{\text{Min}} = \frac{c}{2.\lambda}.\Delta\lambda_{\text{Min}} \tag{2.35}$$

The separation between the FPI mirrors, which also decides its FSR can be estimated by fixing the approximate number of fringes to be moved out during the whole motion of the projectile. As the fringe constant discussed in earlier section gives approximate velocity over which one fringe will emerge out, so by having a prior knowledge about the approximate final velocity likely to be achieved by the projectile, 'd' can be fixed. Once 'd' is fixed the finesse required can be calculated by above-mentioned relations (Eq. 2.34 and Eq. 2.35).

In our experimental setup the parameters for Fabry-Perot etalon have been decided to measure a minimum velocity of 0.2 km/s and movement of at least one new fringe for every velocity change of 2 km/s.

The selection of laser is also an important task as this is a precision experiment. The primary requirement for a laser is to provide enough light to generate a recordable signal and its bandwidth should be small enough to detect the minimum Doppler shift in wavelength.

The streak camera records the fringe motion generated by the FPI, hence its characteristics are also crucial. The important parameters of a streak camera are temporal resolution, distortion, dynamic range, and sweep speed. These parameters are system dependent and may be decided according to the experimental requirements. The slit width of the camera is chosen as the compromise between maximizing illumination and minimizing the errors introduced due to fringe curvature on the slit.

2.4.2.2 Experimental setup of Fabry-Perot velocimeter

The experimental configuration of Fabry-Perot velocimeter is shown in Fig. 2.8. A narrow line-width, frequency doubled Nd:YVO$_4$ cw laser is used to illuminate the target. Light
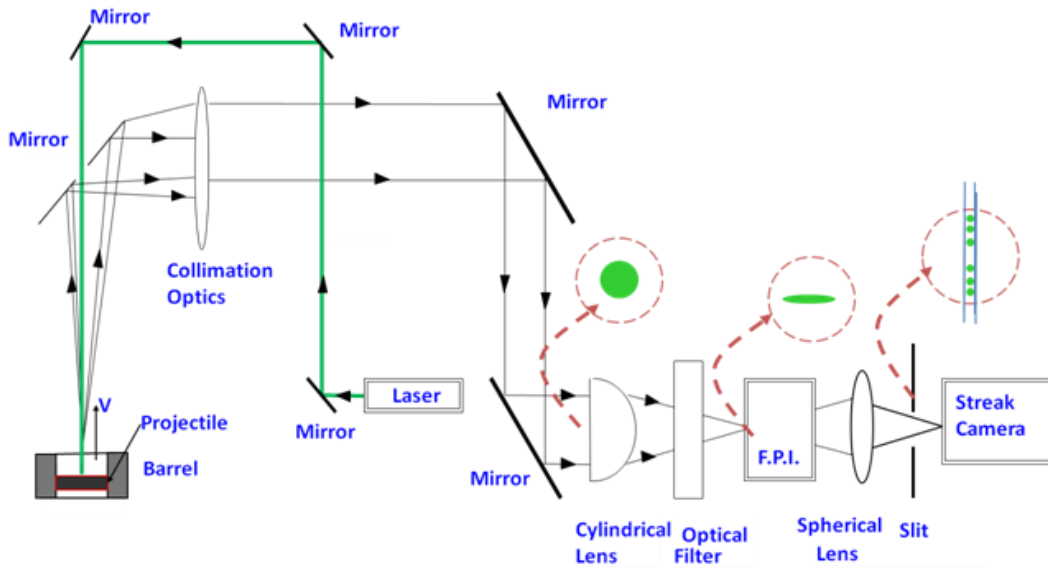
Fig. 2.8: Experimental setup of Fabry-Perot velocimeter.

reflected from the target is collected and collimated by a lens and directed towards an air spaced

Fabry-Perot etalon. The various design parameters are chosen to measure velocity in the range of

0.2 -10 km/s. The laser line-width is decided in such a manner that it is much smaller than the

expected minimum Doppler shift in wavelength. A cylindrical lens is placed before Fabry-Perot

etalon to introduce one dimensional convergence in the incident beam. Due to this cylindrical

lens, constructive interference fringes appear as dots on the camera slit, rather than usual ring

pattern produced by Fabry-Perot interferometer, hence a considerable intensity gain is achieved

using cylindrical lens. The Fabry-Perot interferometer is followed by a spherical lens, which

focuses the interference pattern on to the camera slit, which is placed perpendicular to the axis of
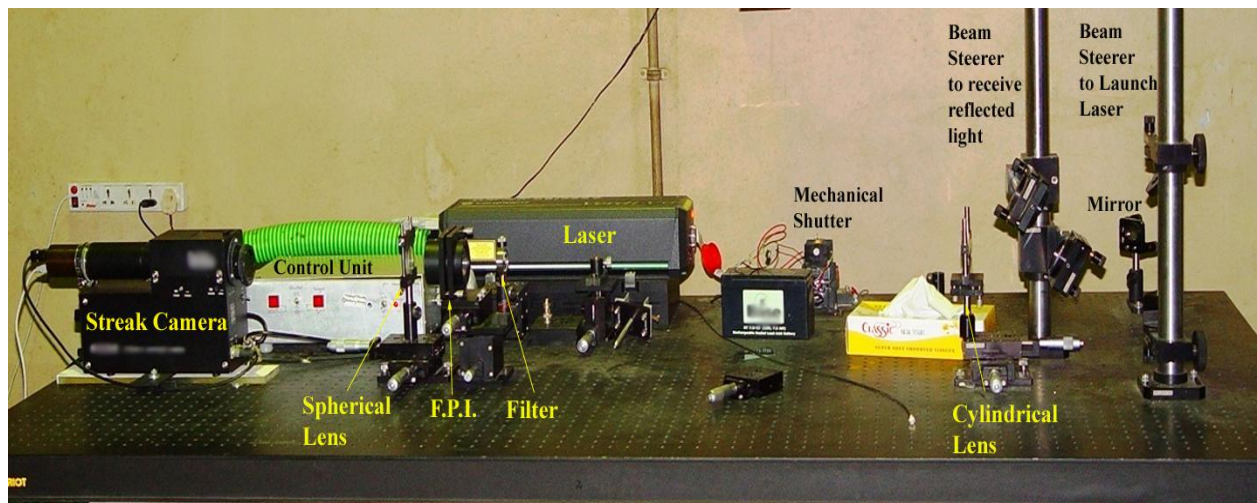
Fig. 2.9: Photograph of the Fabry-Perot velocimeter.

cylindrical lens. When light is expected to be generated during an experiment, an optical filter is

also placed before Fabry-Perot interferometer. The number of fringes observed in the streak

camera is determined by the focal length of cylindrical lens, and fringe diameters are decided by

the focal length of spherical lens. Streak camera with slits of width 100-200 μm is used in streak

mode to record the time history of interference fringes. Photograph of our system is shown in

Fig. 2.9. Here two separate beam steerers are used to launch and receive the laser light. Light is

launched through a mirror having an inclined hole at its centre along the surface normal direction. This mirror also collects the light reflected from the surface under study. To avoid plasma generated light during the experiment a narrow bandwidth (10 nm) band-pass optical filter is placed before the interferometer.

2.4.2.3 Error analysis in velocimeter records

Absolute error analysis for velocimeter records can be done by using the Eq. 2.33 in following form:

$$v = C'. \left(i + \frac{\left(D_{R_0}^2 - D_{L_0}^2 \right)}{\left(D_{L_1}^2 - D_{L_0}^2 \right)} \right) \tag{2.36}$$

$$\Rightarrow v = C'.i + C'. \frac{\left(D_{R_0}^2 - D_{L_0}^2 \right)}{\left(D_{L_1}^2 - D_{L_0}^2 \right)}$$

Where $\quad C' = \dfrac{c\lambda}{4\mu d} \quad = 1.99 \, \text{km/s for present setup.} \tag{2.37}$

Using Taylor series expansion in terms of D_R, D_{L0}, and D_{L1}, the absolute error in velocity may be written as:

$$\Delta v = \left(\frac{\partial v}{\partial D_{R0}} \right). \Delta(D_{R0}) + \left(\frac{\partial v}{\partial D_{L0}} \right). \Delta(D_{L0}) + \left(\frac{\partial v}{\partial D_{L1}} \right). \Delta(D_{L1}) \tag{2.38}$$

$$= A1.\Delta(D_{R0}) + A2.\Delta(D_{L0}) + A3.\Delta(D_{L1}).$$

Where :

$$A1 = \frac{2.C'.D_{R0}}{(D_{L1}^2 - D_{L0}^2)} \tag{2.39}$$

$$A2 = C'. \frac{2.D_{L0}.(D_{R0}^2 - D_{L1}^2)}{(D_{L1}^2 - D_{L0}^2)^2} \tag{2.40}$$

$$A3 = C'. \frac{2.D_{L1}.(D_{R0}^2 - D_{L0}^2)}{(D_{L1}^2 - D_{L0}^2)^2} \tag{2.41}$$

Here the errors caused by λ and d are not considered as these are much smaller ($\Delta\lambda/\lambda$ ~10^{-8} and $\Delta d/d$ ~ 10^{-5}) than the errors caused by diameter measurements.
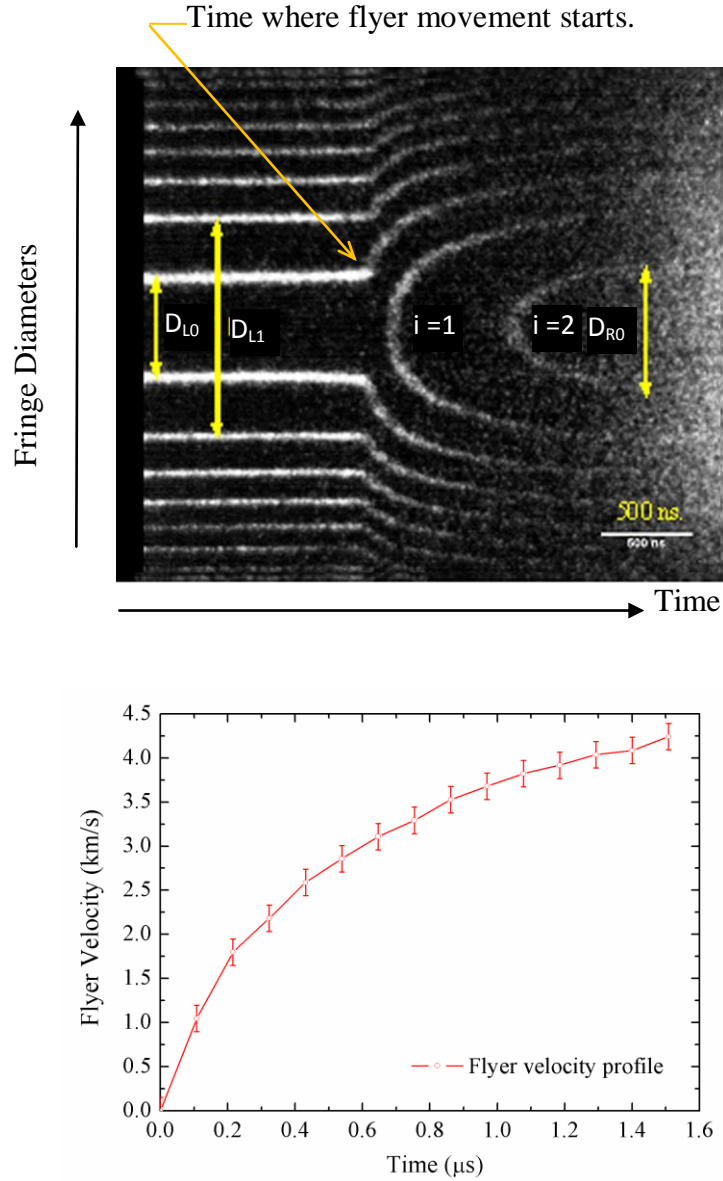
Fig. 2.10: (a) Streak record showing the evolution of interference fringes with time. (b) Typical inferred velocity profile.

It may further be noted that our initial experiments on equation of state and flyer velocity measurements have been carried out on a streak camera which provides records on photographic films, and the error in measurement of fringe diameters is considered as the average of fringe

thicknesses. Later with the availability of accurate digital streak camera a method has been developed to measure fringe diameters with better accuracies.

To illustrate the typical accuracies of our setup an experimental data is considered here, when electric gun was operated at 34 kV and a flyer velocity of 4.2 km/s has been achieved on composite flyer made of 100 μm aluminum bonded to 125 μm Kapton sheet. The evolution of fringe pattern measured on the streak camera is shown in Fig. 2.10 along with computed flyer velocity profile.

Here the typical fringe diameters and their widths as deduced from the streak record after certain digital magnification are as follows:

D_R= 50.38 mm (near the terminal velocity), D_{L0}= 44.68 mm and D_{L1} = 96.873 mm.

While ΔD_{L0} = 5.4 mm, ΔD_{L1} = 5.4 mm and ΔD_R = 5.6 mm (typical).

Therefore using Eq. 2.38, absolute error in velocity may be written as:

$$\Delta v = (2.72x10^{-2}).5.4 + (2.23x10^{-2}).5.4 + (3.83x10^{-3}).5.6 \, \text{km/s}$$
$$\Rightarrow \Delta v \approx 0.3 \ \text{km/s}$$

$$\Rightarrow \left(\frac{\Delta v}{v} \right)_{Absolute} = 7.1\%$$

Further as the maximum absolute error depends upon the value of D_{R0} hence it is different for different velocity points. The value of D_{L0} depends upon the operating mode (frequency) of the laser, which is internally decided by the laser instrumentation and may also vary from one experiment to other. These errors may further be reduced with the help of image analyzing schemes that can more accurately predict peak position and reduce the error in its determination. A method for velocity measurements at the time of flyer impact with better accuracies has been developed and will be discussed in Chapter 5.

2.4.2.4 Resolution

It is clear from the above-described relation for absolute error in velocity that it is mainly caused by the error in measurement of fringe diameters. Hence the minimum detectable change in fringe diameter will decide the resolution of present setup. Considering that change in fringe position may be deciphered when a fringe moves by half of its thickness. Therefore by substituting $D_{R0} = D_{L0} + \Delta D$ in Eq. 2.33 a relation for minimum detectable velocity may be written as:

$$v_{MIN} = \frac{c\lambda_L}{4d\mu}\left(\frac{2D_{L0}\Delta D}{D_{L1}^2 - D_{L0}^2}\right) \qquad (2.42)$$

Here ΔD corresponds to full fringe width as D_{R0} is obtained by the movement of two diametrically opposite fringes. Substituting the following experimentally measured values in above expression:

$D_{L0} = 44.68$ mm, $D_{L1} = 96.873$ mm, $\Delta D = 5.4$ mm, $\frac{c\lambda_L}{4d\mu} = 1.99$ km/s.

$\Rightarrow$ $\qquad\qquad\qquad\qquad\qquad v_{MIN} = 0.13$ km/s

Considering the diameter values obtained in other experimental records, we can reasonably conclude that the velocity resolution of our system is 0.2 km/s.

2.4.2.5 Dual beam Fabry-Perot velocimeter

One of the important outcomes of present work is the development of a dual beam Fabry-Perot velocimeter (FPV) with improved capabilities to simultaneously measure the velocity profiles of projectile as well as that of target-window interface. The recording of two fringe patterns on a single streak camera helps in precisely determining these velocities at the time of impact and also makes this technique more economic. It is worthwhile to mention that the

measurements of two velocities are crucial to determine the Hugoniot of a given material. These velocities may be projectile (flyer) velocity and the free surface or target window interface velocity of impacted target. While working in dual beam mode the interferometer is illuminated by a light consisting of two Doppler shifted wavelengths one from the accelerated projectile and other from the shocked target, to generate a superimposed fringe pattern. As the rate of change of fringe diameters are different for two surfaces and both start at different time instances therefore it is possible to identify and infer the velocity records of both the surfaces.
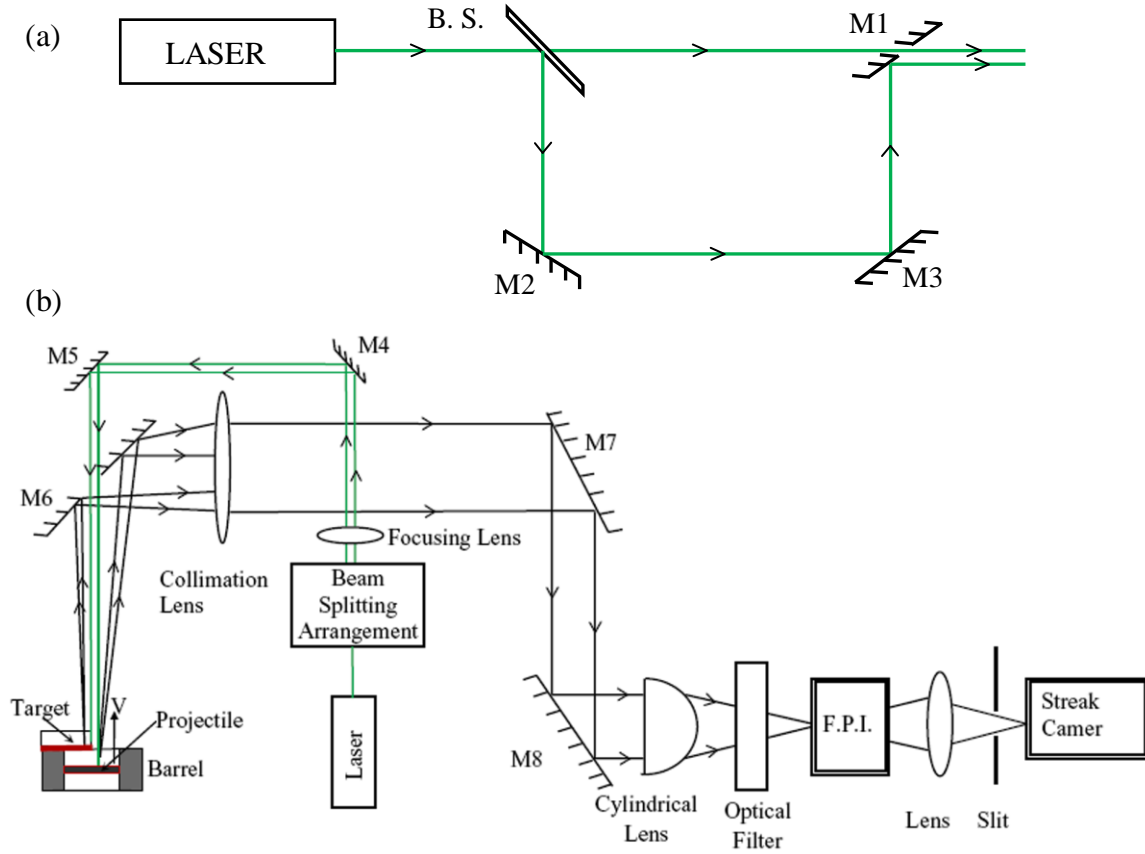
FIG. 2.11: Assembly of (a) beam splitting optics to generate two parallel beams from a single laser and (b) modified dual beam Fabry-Perot velocimeter to record two surface velocities on a single streak record. (M1 - M8: Optical mirrors with M1 and M6 having an inclined hole at their centre, B. S.: Beam splitter of ratio 70:30, and F.P.I.: Fabry-Perot interferometer).

Multi point velocity measurement systems were reported earlier [84, 111] but due to use of multiple streak cameras and complicated optical arrangements, these extensions were less economic and limited to a few laboratories only. The concept of dual beam velocimeter [112] has also been worked out in present thesis, using half the laser beam for illumination of target while other half for illumination of flyer and carried out the equation of state (EOS) measurements on polyurethane based retro-reflective tape and aluminum targets that will be discussed in Chapter 4. But this type of arrangement put a restriction on the placement of target as well as it poses difficulty in controlling the laser energy distribution over the target and flyer. In many experiments it is desired to concentrate more laser energy on target than flyer due to severe degradation in target reflectance on shock arrival. Therefore a reinvestigation has been carried out with necessary modifications to measure the EOS points with better accuracies using two beams of unequal intensities derived from a single laser.

The dual beam FPV essentially involves the generation of two nearly parallel laser beams of unequal intensities and recording of dual interference pattern on a streak camera. The optical arrangement used to divide single laser output into two nearly parallel optical beams is shown in Fig. 2.11 (a). Here a beam splitter (B.S.) is used to create two beams of unequal intensities in ratio of 70:30, which are later combined on a mirror (M1) having an inclined hole at 45° with the help of two mirrors (M2 and M3). One beam directly passes through the inclined hole and the other is reflected from the front metallic coatings near the hole. The separation between the two beams can be varied by changing the position of mirror (M3). As the diameter of these beams are quite large (2-3 mm), a good quality focusing lens (Fig. 2.11 (b)) is used after beam splitting assembly to obtain focused spots of diameter less than 1 mm. Though this lens slightly disturbs the parallelism of two beams but in shock experiments normally diffused surfaces are used and

slightly non-parallel beams may not have significant effect on scattered light collected from both the surfaces. The schematic of dual beam FPV is shown in Fig. 2.11 (b), it is similar to standard velocimeter except that the scattered light is collected from two surfaces and focused on the interferometer. One beam is focused on projectile and other is focused on target-glass interface such that the time profile of interference fringe diameters of both the surface are recorded on same streak camera. The beam on target-glass interface is positioned away from the target edge to avoid early arrival of release waves from the free boundaries. Due to difference in vertical position of two surfaces by barrel height (typically 2-3 mm) the focused spots after cylindrical lens are found to be slightly displaced. But by positioning the direction of two incident laser beams, this displacement can be aligned along the direction of camera slit. Thus initially when both surfaces are at rest two slightly displaced fringe patterns are formed, which separate out after the movement of flyer and may be used for measuring the values of D_{L0} and D_{L1} used in Eq. 2.33. It may also be noted that the quantity $(D_{L1}^2 - D_{L0}^2)$ remains the same for both the patterns and is independent of Doppler shift, [81] therefore it may be calculated from any part of streak pattern. The temporal resolution of a Fabry-Perot velocimeter is mainly decided by the cavity fill time of etalon and streak camera resolution as also discussed in detail in Ref. 81. In present experimental setup the dominating factor is cavity fill time and the temporal resoltion was found to be approximately 3 ns.

2.4.3 Fiber optic pins

Materials having poor reflectivity or subjected to very high pressures, where reflectivity reduces to very low levels, the implementation of Fabry-Perot velocimeter becomes difficult. In such materials equaion of state data may be generated by measuring the shock velocity using arrival time gauges placed on stepped targets. As pulsed power souces generate lot of EM

interference, use of electrical pins is not preferred and optical techniques are normally implemented. At high pressures, the arrival of shock wave also generates a weak luminescence due to sudden change in temperature near the free surface or by the inonization of compressed air present in its viscinity. To experimentally detect these light signals at different target steps, we have utilized large diameter (~1mm) polymer optical fibers with fast photodiodes. These fibers have been coupled to fast avalanche photodiodes at other end and their output has been recorded on an oscilloscope. Avalanche photodiodes have been reverse biased near the breakdown region, and have a rise time of approximately 3 ns. Avalanche photodiodes are preferred because of their faster response time and better light detection efficiency as the light signals are generally weak and time delay between two fiber signals is of the order of few ten's of ns. Time delay between the generations of shock luminescence at consecutive steps is then used to compute the shock wave velocity in the impacted targets.

2.5 1-D hydrodynamic numerical simulation

The performance of electric gun depends upon many parameters like bank charging voltage, its inductance, geometry of exploding foil, and material properties of foil, flyer and tamper etc. Interdependence of these parameters makes the task of optimization very complex and theoretical modeling is normally desirable. The flyer is accelerated by both hydrodynamic and magnetic forces. To optimize the system design and predict the flyer velocity profile, a 1D hydrodynamic code that considers both hydrodynamic as well as magnetic forces and based upon Lagrangean finite difference formulation developed earlier [113] is implemented. This code is developed in FORTRAN-90 and requires the electrical parameters of capacitor bank and dimensional parameters of foil and flyer as input and generates the spatial (along the direction of motion) and temporal profiles of pressure, temperature, density, velocity, and energy deposited at

user defined time intervals. The predictions of hydrodynamic code are normally governed by the implemented models of resistivity of the exploding foil as a function of pressure and temperature and the equation of state of the flyer and foil material. The present formulation utilizes the EOS model proposed by McCloskey [114] and resistivity model by Burgees [115] and the velocity predictions for this combination are compared with the experimental results measured on different capacitor banks. Details will be discussed in next Chapter.

In this code the complete region of interest is divided into finite number of meshes. The mesh scheme is shown in Fig. 2.12 where the subscript indicates the mesh number, and the quantities p, ε, Q, u, J, σ, R represent the pressure, internal energy, electrically deposited energy, velocity, current density, electrical conductivity and position coordinates of different meshes respectively. The quantities with half subscript are used to indicate their values at the center of the meshes. The mesh boundaries for exploding foil are defined by user at start and calculations for electrical energy and magnetic pressure are carried out for meshes between these boundaries only.
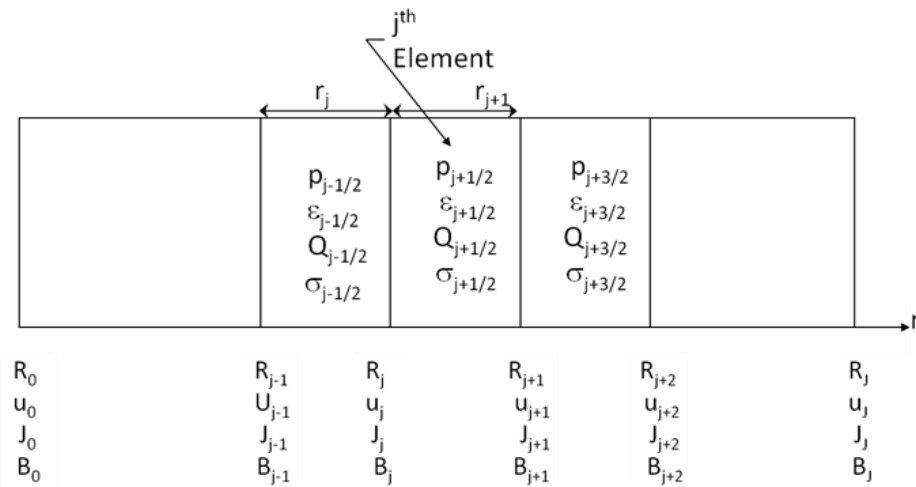
Fig.2.12: Mesh scheme.

Lagrangean differential equations for fluid dynamics representing the conservation of mass, momentum and energy can be written in finite difference form as given in Ref. 116:

$$\text{Conservation of mass :} \qquad V_{j+1/2}^{n+1} = V_O \frac{R_{j+1}^{n+1} - R_j^{n+1}}{r_{j+1} - r_j} \qquad (2.43)$$

$$\text{Conservation of momemtum :} \qquad \frac{u_j^{n+1} - u_j^n}{\Delta t} = -2V_O \frac{p_{j+1/2}^n - p_{j-1/2}^n}{(r_{j+1} - r_{j-1})} \qquad (2.44)$$

$$\text{Conservation of energy :} \qquad \varepsilon_{j+1/2}^{n+1} - \varepsilon_{j+1/2}^n + p_{j+1/2}^n(V_{j+1/2}^{n+1} - V_{j+1/2}^n) = Q_{j+1/2}^n \qquad (2.45)$$

In addition to above three equations, equation of state of the material is also required to solve these equations exactly.

$$\text{Equation of state:} \qquad p_{j+1/2}^{n+1} = f(\varepsilon_{j+1/2}^{n+1}, V_{j+1/2}^{n+1}) \qquad (2.46)$$

Here the superscript 'n' is used to indicate the time step and 'V' and 'r' represent the specific volume and the Lagrangean coordinates of the meshes respectively.

The current values are obtained at each time step by solving the equations of LCR circuit. The inductance and resistance are considered in two parts. One is of capacitor bank, which remains constant during the simulations, and other is of exploding foil which varies as per the change in foil parameters. These computed current values are further used to calculate the boundary values of the magnetic field at extreme ends of exploding foil. The boundary value of magnetic field is taken as the magnetic field produced by two infinite current carrying flat transmission lines. This assumption is fairly valid when the return current carrying conductor is assumed to be placed just below a tamper, whose thickness is much smaller than the lateral dimensions of transmission lines. Using Maxwell's equations, magnetic field diffusion equation in one dimension may be written as:

$$\left(\frac{\partial \mathbf{B}}{\partial t}\right) = \left(\frac{1}{\mu_0 \sigma}\right) \cdot \left(\frac{\partial^2 \mathbf{B}}{\partial \mathbf{R}^2}\right) - \left[\frac{1}{\mu_0 \sigma^2}\left(\frac{\partial \sigma}{\partial \mathbf{R}}\right) + v\right] \cdot \left(\frac{\partial \mathbf{B}}{\partial \mathbf{R}}\right) - \mathbf{B} \cdot \left(\frac{\partial v}{\partial \mathbf{R}}\right) \qquad (2.47)$$

Above equation in finite difference form along with the boundary values can be solved

for calculating the value of magnetic fields at different mesh boundaries. The variation of

resistivity with foil temperature and volume is taken according to the model proposed by

Burgees [115]. The computed magnetic field at every mesh boundary is then used to calculate

current densities at the center of the meshes using following equation in finite difference form:

$$\nabla \times \mathbf{B} = \mu_0 \mathbf{J} \qquad (2.48)$$

These calculated current densities are further used to calculate the electrical energy

deposited and magnetic force acting on different meshes. For pressure calculations a three-term

equation of state proposed by McCloskey is implemented. This equation of state considers the

pressure and specific internal energy as summation of three terms which may be expressed as:

$$P(\eta, T) = P_c(\eta) + P_n(\eta, T) + P_e(\eta, T) \qquad (2.49)$$
$$E(\eta, T) = E_c(\eta) + E_n(\eta, T) + E_e(\eta, T)$$

Here first term is the contribution from the elastic interactions at 0 K, second term is the

contribution from thermal lattice vibrations and third term stands for thermal excitation of

electrons. Each of these terms have different analytical formulation for different thermodynamic

regimes and described in detail in the report by McCloskey [114]. This equation of state model is

further modified to include the Thomas Fermi quantum corrections in the high pressure and high

temperature regime [117]. The validity of this equation of state has been verified by matching the

Hugoniot and isotherm generated by the code with the experimentally reported values. To

maintain the stability in presence of shock, a dissipative term, known as artificial viscosity is also

added in pressure term, as suggested by VonNeumann [118]. The implicit numerical method is

implemented to calculate the temperature from energy equation and explicit method is used for

velocity calculations in momentum conservation equation. The initial time step in the code is user defined but its value is restricted in the code by Courant-Friedrichs-Lewy [116] condition. Further time step adjustment is also carried out by observing the convergence in temperature and density values for different meshes.

The present code allows user to enter following inputs:

- o Dimensions and materials of exploding foil and flyer.

- o Electrical parameters for capacitor bank.

- o Number of meshes for different materials.

At start the code checks the consistency of input data opens output files and defines the coordinates, thermodynamic and electrical properties of different meshes. The code runs the hydrodynamic simulations till the flyer cross a user defined barrel length or the number of runs exceeds a pre-defined limit. The code stores various thermodynamic and electrical parameters of different meshes at user defined time intervals in one output file. In another output file parameters like pressure, temperature, density, resistivity in the central mesh of exploding foil, circuit current, and flyer velocity (i.e. velocity of outermost mesh) are stored in a tabular form at pre-defined time intervals. This data file can be imported in any plotting software to display output in graphical form. Time of burst of exploding foil is taken as the time at which a sharp rise in resistivity is observed. The validation this code, its predictions for ELG-8 system and major outcomes will be discussed in next chapter.

2.6 Plasma motion based crowbar switch

A high coulomb rating switch and crowbar arrangement is desired in large capacitor bank systems utilized in applications like rail gun and coil gun. An effort has been made in this direction to combine both the switch and crowbar in a single design. In this scheme a plasma

motion based rail spark gap has been modified to incorporate another crowbar electrode at the end of rail electrodes. The discharge plasma generated and accelerated by self generated magnetic field in modified main rail gap switch is utilized to close the additional crowbar switch at a predefined time. Here we will describe it briefly while details may be found in Ref. 119.

A typical capacitor bank system with crowbar circuit is shown in Fig. 2.13. Initially the capacitor is charged to a predefined voltage while switches S_M and S_C are in open state. Then the main switch S_M closes and initiates current in the load consisting of resistance R_L and inductance L. Subsequently when current reaches its peak, second switch S_C closes and provides a low impedance path (Z_C) to the current which protects the capacitor and load from reaching large negative voltage cycles.
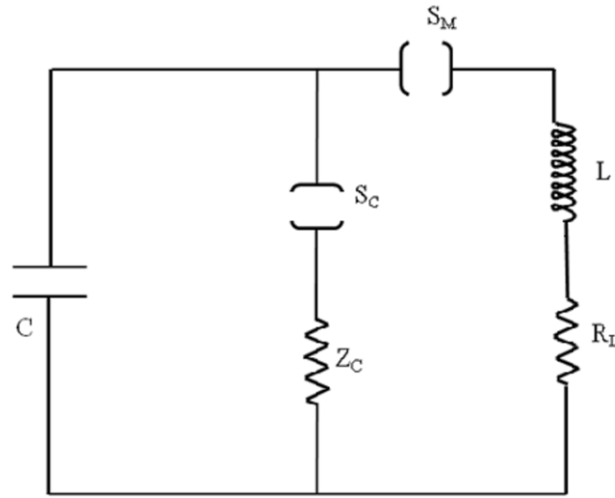
Fig.2.13: Circuit model of crowbar switch.

An arc motion based rail gap switch was reported by Kovalchuk *et al.* [120] to achieve less electrode erosion, especially for high coulomb charge transfer applications like rail gun, coil gun, magnetic flux compression generator etc. We have further modified this geometry by using a typical field distortion type rail gap switch and replacing its knife edge trigger electrode by a point electrode kept at one end of the rails. Another electrode connected to crowbar resistor has

been placed near the high voltage electrode at the other end of the rails. The schematic of this modified switch is shown in Fig. 2.14. The separation of crowbar electrode from high voltage (HV) electrode is kept larger than that of main sparkgap to avoid its self breakdown before the start of load current. Further the crowbar electrode is placed at one side of the rail gap to avoid its direct exposure to UV radiation generated during main gap closure. The mechanism of this scheme is as follows: first the trigger electrode initiates the breakdown at one end of the rails; Lorentz (**J X B**) force accelerates this discharge channel along the rails; when this discharge plasma reaches other end of rails it closes the gap between HV and crowbar electrodes and diverts current from load to crowbar resistor.
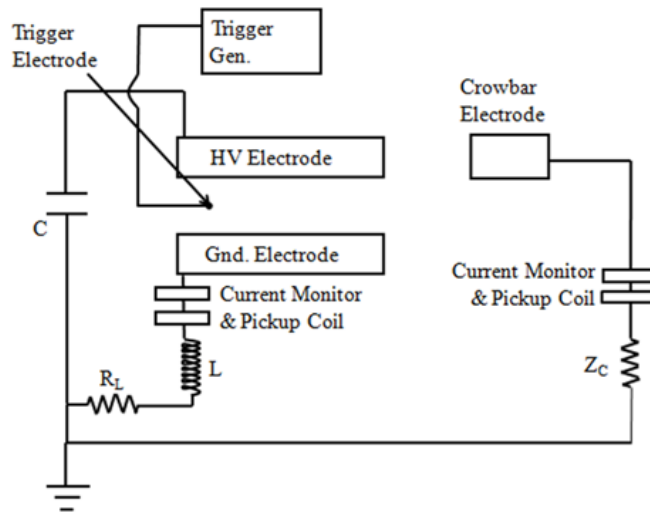
Fig. 2.14: Schematic of modified rail gap switch with crowbar electrode.

The impedance of crowbar resistor is kept smaller than that of main load so that at the time of crowbar major portion of bank current shall get diverted to the crowbar resistor. If we assume a parallel RLC circuit, which means that in Fig. 2.13 the load is pure inductive and inductance associated with capacitor and crowbar resistor are negligible, then to critically/ over damp the circuit, resistance of the crowbar resistor should satisfy the following relation:

$$Z_C \leq \frac{1}{2}\sqrt{\frac{L}{C}} \qquad (2.50)$$

The detailed analysis for a realistic crowbar design is discussed in [121]. For applications involving large capacitor banks these crowbar resistors also need to have capability to handle high energy levels and an efficient design has been reported by Rim *et al.* [122].

As reported by Kharlov in [123] the theoretical expression for the velocity of discharge plasma of negligible mass (which has also been reported to be very close to plasma channel of finite masses) at any instant 't' may be written as:

$$v(t) = \sqrt{\frac{2I(t)B(t)d}{(\gamma + 1)\rho S}} \qquad (2.51)$$

Here I (t) and B(t) are current and magnetic field at time 't' respectively, while d and S are length of plasma channel and its cross-sectional area. Constant 'γ' is the usual ratio of specific heat capacity at constant pressure to that at constant volume and ρ is the air density at atmospheric pressure. These are taken as 1.4 and 1.164 kg/m^3 respectively at a temperature of 303 K. Generally length of rail electrodes is larger than the gap between them, therefore average magnetic field over the gap may be approximated as that created by two semi-infinite parallel cylindrical rails and can be expressed as:

$$B_{avg}(t) = \frac{\mu_0}{2\pi} \times \frac{I(t)}{d} \times \ln\left(\frac{R+d}{R}\right) \qquad (2.52)$$

In this relation 'R' is the radius of rails and other symbols have their usual meanings. Substitution of magnetic field value from Eq. 2.52 to Eq. 2.51 and values of standard parameters in MKS units provide an expression for plasma velocity which is governed only by current and geometrical factors.

$$v(t) = 3.71 \times 10^{-4} \times I(t) \times \sqrt{\frac{1}{S} \times \ln\left(\frac{R+d}{R}\right)} \quad m/s \qquad (2.53)$$

In the present work, two such switches have been designed using small length electrodes and characterized at atmospheric pressure on a relatively fast (time period = 27 μs) and a slow (time period = 330 μs) capacitor banks. Initial experiments have been carried out on fast bank to investigate the effect of crowbar electrode on main discharge current and later experiments have also been conducted on slow bank to measure the velocity of discharge plasma with better accuracies.

Table 2.3

Capacitor Bank Electrical Parameters

Parameters	Fast Bank	Slow Bank
Capacitance:	11 μF	800 μF
Inductance:	1.73 μH	3.45 μH
Charging Voltage:	8.0 kV	2.5 kV
Time Period:	27 μs	330 μs
Resistance:	56 mΩ	13 mΩ
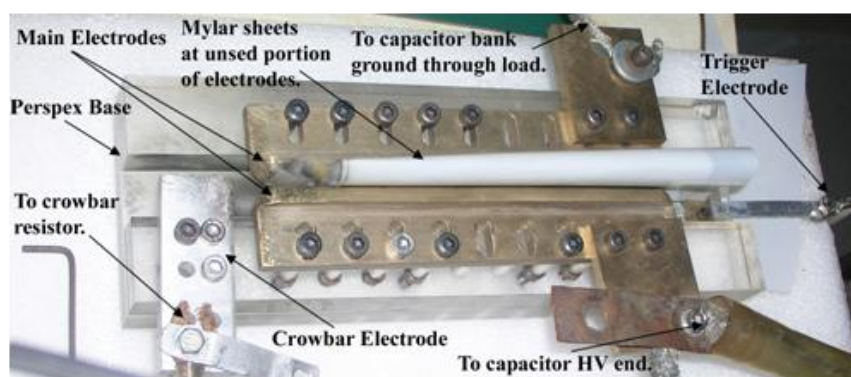
Fig.2.15: Photograph of modified rail gap switch.

To observe the influence of magnetic forces on plasma motion at atmospheric pressure the knife edge trigger electrode of field distortion type rail gap switch has been replaced by a

point electrode located at one end of the rails as shown in Fig. 2.15. The electrical parameters of both banks are shown in Table 2.3.

Modified rail gaps have been designed with long rail electrodes available with us, having total length of 30 mm for fast bank and 200 mm for slow bank. But the effective usable length of these electrodes can be varied from 3-25 mm and 10-47 mm for fast and slow bank respectively by changing the position of trigger electrode and placing an insulator sheet between unused portions of the rails. At one end of the rails a similar shaped but smaller in size crowbar electrode has been fixed near the HV electrode over the Perspex base at a separation of nearly 10 mm. The parallelism between the rails has been maintained within an accuracy of 0.1 mm by using a spacer of known thickness. The gap between main electrodes near the trigger point is important as it will decide the operating voltage, but once the plasma is formed slight variation in gap will only affect plasma channel velocity as given by Eq. 2.53. These modified rail gaps are operated in open atmosphere and their typical design parameters are shown in Table 2.4.

Table 2.4

Modified Rail Gap Parameters

Parameters	Fast Bank	Slow Bank
Total Electrode Lengths:	30 mm	200 mm
Effective Electrode Lengths:	3-25 mm	10-47 mm
Electrode Diameter:	15 mm	20 mm
Electrode Material:	Steel	Brass
Gap between main electrodes:	4.0 mm	0.9 mm
Charge Transfer:	0.8 C	11.2 C
Gap between crowbar and main electrode:	10mm	10 mm

A trigger pulse of 35 kV and rise time of 500 ns has been applied to the pointed electrode of rail gap switch to initiate the plasma formation. Crowbar resistors have been made from thick aluminum/ copper strips with typical resistance of around 10 mΩ and were connected to the capacitor ground electrode with a short length cable.
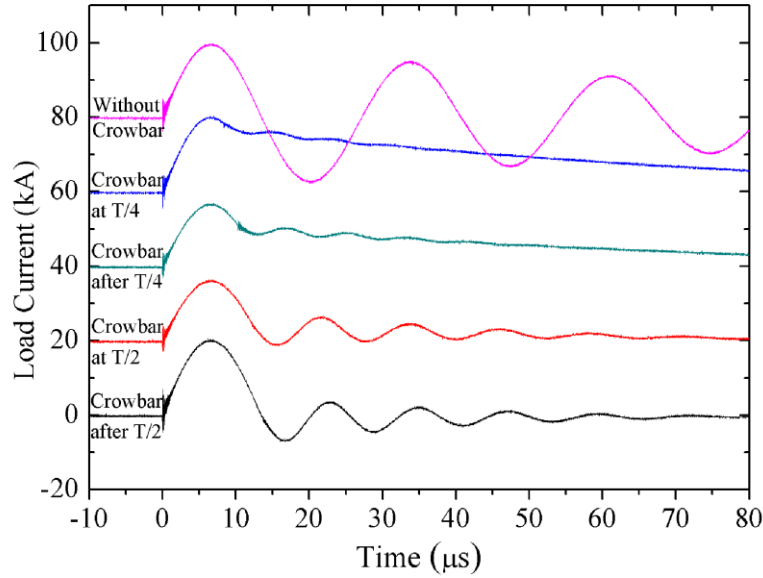
Fig.2.16: Output of current monitor placed in the load current path for different effective electrode lengths. Each waveform is off shifted by 20 kA from bottom to top for better clarity.

To measure the rate of change of load and crowbar currents, one magnetic pick up coil (dB/dt probe) with rise time < 150 ns is placed in the load current path and other in the crowbar path. In addition to this a current monitor with rise time < 400 ns is also placed to measure the load current. The time of crowbar is detected by the time of current start in the crowbar resistor indicated by the sharp change in dB/dt probe output. The feasibility of present scheme has been first investigated on fast bank due to its easy operational procedures and crowbar effect has been observed at different point of current profile. The position of trigger electrode has been changed to achieve different electrode lengths and depending upon the velocity of moving plasma the crowbar gap is closed at different times. The obtained current profiles with and without crowbar

are shown in Fig. 2.16. Experimental records obtained in one experiment when electrode length

was chosen such that the bank current diverts from load to crowbar resistor at near the half time

period of current cycle is shown in Fig. 2.17.
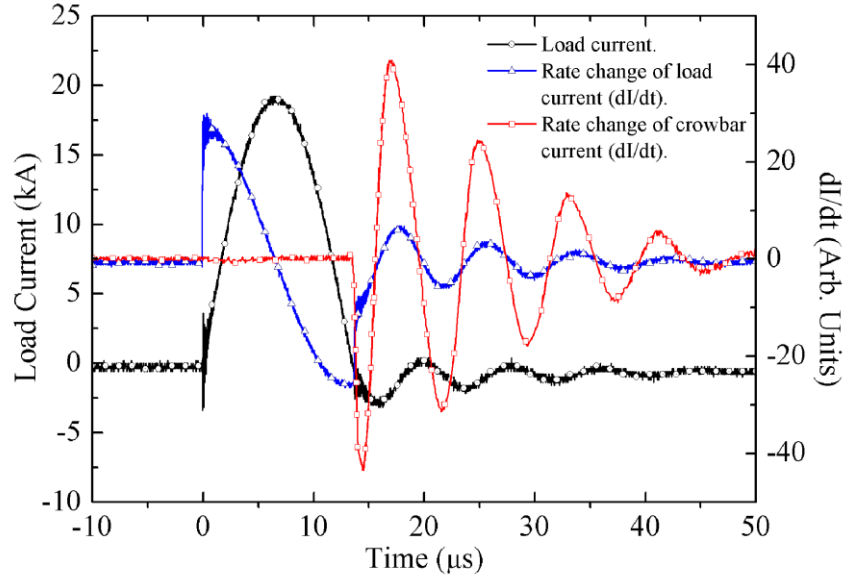
Fig.2.17: Experimental record for fast bank showing load current measured by current monitor and output of dB/dt probes placed near the load and crowbar current path respectively.

As the total travel length of plasma is very small (~2.6 mm) till current peak in case of

fast bank, therefore it was practically difficult to accurately measure the plasma velocity and it

was estimated to be nearly 300 m/s by only a few measurements. For better accuracies in

measurements, similar experiments have been carried out with slow bank. In these experiments

both load and crowbar currents have been measured with current monitors and voltage across

capacitor bank has been measured with Tektronix make high voltage probe (P6015A). Measured

current and voltage signals indicating the crowbar effect near current peak are shown in Fig. 2.18

along with a voltage waveform recorded in a separated experiment without any crowbar effect.

Diversion of load current to the crowbar resistor can easily be observed in this figure and the

load current after crowbar has been found to be decaying exponentially with small oscillations.
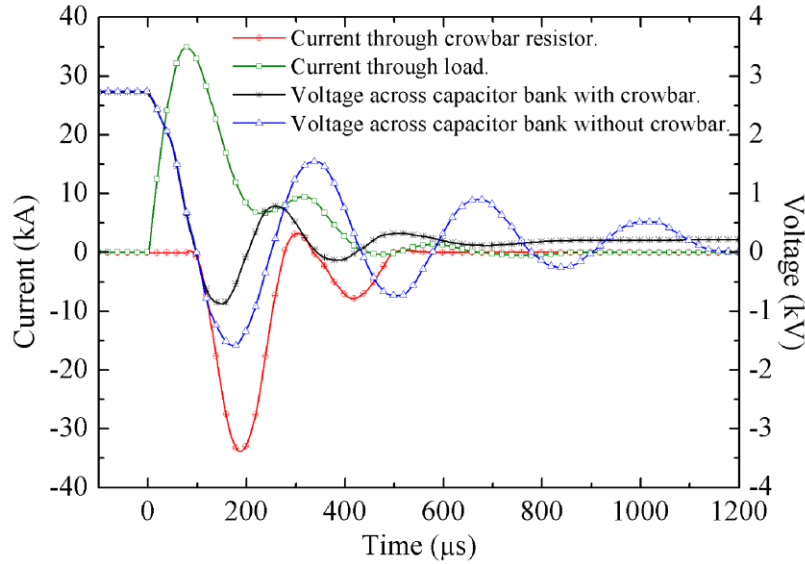
Fig.2.18: Experimental record for slow bank showing current flowing through the load and crowbar resistor along with voltage measured across the capacitor bank with and without crowbar.

These oscillations appear to be caused by improper choice of resistors having significant inductance also associated with them to critically damp the capacitor bank as also discussed in [124].

Table 2.5

Plasma Velocity Measurements

Effective Electrode Length (mm)	Time Delay (µs)
10	31.2
14	32.8
18	52
19.5	46.4
24	56
Measured Average Velocity up to peak (m/s):	440
Theoretical Average Velocity (m/s):	642

The comparison of voltage waveforms obtained with and without crowbar effect clearly indicates (Fig. 2.18) that peak reversal voltage and number of cycles reduces significantly with crowbar, hence this scheme also helps in enhancing the life of capacitor bank. These results for slow and fast banks demonstrate the mechanism of crowbar which can be improved further by suitable selection of resistors. The delay between the start of load current and start of crowbar current for different electrode lengths are shown in Table 2.5.

These two values have been used to calculate the average plasma velocity near the current peak (till 56 µs) by using least square fit and are shown in same table along with theoretical predictions obtained from Eq. 2.53. The difference between the theoretical and experimental values might be caused by the error in measurement of effective electrode length which is more significant at smaller values due to curvature in electrodes at edges. The other parameter responsible for this mismatch is the width of the plasma channel which is obtained from visible erosion marks created on the electrodes after the shot and in present case it was typically 8-10 mm.

Chapter 3

Optimization Studies on Electric Gun

The flyer velocity in electrically exploding foil system is governed by various inter-related geometrical and electrical parameters. Normally capacitor banks are used to generate fast rising high current pulses for foil explosion. For any capacitor bank the peak current and its rise time is decided by its electrical parameters like inductance, capacitance, resistance and charging voltage, which cannot be modified beyond certain limits. Therefore optimization of exploding foil parameters for a given system is crucial to achieve higher flyer velocities. With suitable foil optimizations it is possible to develop portable devices for moderately high pressure shock studies. In present work, an experimental study has been carried out to observe the effect of foil dimensions, ambient pressure, current rise time, barrel length and its area on flyer performance. The 1D numerical scheme discussed in last chapter has also been validated to predict the flyer velocity on ELG-8 system as well as on the other reported high energy banks. This chapter sequentially covers these experimental and numerical studies with their detailed outcomes.

3.1 Effect of foil dimensions

In previous chapter, it was discussed that the cross-section area of exploding foil may be estimated by using empirical relation of Action Integral along with current profile of capacitor bank. The cross-section is the product of foil width and its thickness; therefore it is necessary to

chose proper combination of thickness and width to achieve maximum velocity. The upper limit to the foil thickness comes from the skin depth of current for a given foil material at oscillation frequency of capacitor bank. This criterion ensures the uniform heating of foil, but does not provide the optimized foil width or thickness. Therefore to optimize the foil width and its thickness a numerical as well as experimental study has been carried out to observe their effect on flyer velocity.

The numerical scheme first theoretically calculates the burst current density for a given foil dimension using transcendental relation (Eq. 2.4) noted in previous chapter. To solve Eq. 2.4 a numerical code based on False Position algorithm was written in FORTRAN to calculate 't_B' for different foil thicknesses or widths. The value of 'J_B' is computed from Eq. 2.3 using bank parameters listed in Table 2.1.

To estimate the flyer velocity for a given J_B, Gurney relation (Eq. 2.5) is utilized and the required empirical constants (K & n) are experimentally determined for ELG-8 system at different charging voltages by measuring the flyer velocity using Fabry-Perot velocimeter. To include the effect of foil thickness on flyer velocity, Gurney relation may be rewritten as:

$$v_F = \frac{K. J_B^n}{\sqrt{\dfrac{\rho_P d_P}{\rho_F d_F} + \dfrac{1}{3}}}$$

(3.1)

In above expression 'K' and 'n' are usual empirical constants, while $\rho_P,$ d_P and $\rho_F,$ d_F are density and thickness of flyer and foil respectively. To determine the empirical constants exploding foil sandwiches are prepared from a 25 μm thick aluminum foil (99.99 % pure) in geometry such that a central square piece of 10 mm side length forms the exploding foil. A 125

µm thick Polyimide (Kapton) sheet is placed on top of the metallic foil, which rests over a tamper made of 2.0 mm thick PMMA and further supported by a 20 mm thick Nylon piece. A barrel made of steel with an inner hole of diameter 9.8 mm and height 7.0 mm is then fixed over the Kapton sheet with proper alignment.

The bank is charged at different charging voltages to explode the foil at different current densities, which are measured from experimentally recorded current profiles. In these calculations it is assumed that there is no change in foil dimensions till burst. A number of experiments have been carried out on same charging voltage but the shots with highest velocity and long temporal profiles are considered for fitting of Gurney relation. The maximum flyer velocity has been obtained from the plateau of the measured velocity profile curve, for the four different charging voltages listed in Table 3.1. Using Eq. 2.5 along with the data given in Table-3.1, a linear fit has been obtained between the logarithmic values of v_F and J_B and is shown in Fig.3.1. The intercept and slope of this plot has been used to calculate the empirical constants as $K = 2.16$ and $n = 0.69$ respectively.

Table 3.1

Experimental Measurements on 25 µm Aluminum Foil and 125 µm Kapton Flyer

Vch (kV)	J_B ($X10^{11} A/m^2$)	Flyer Velocity (km/s)
17	5.20	3.9
25	5.92	4.3
30	6.80	4.7
35	6.91	5.0
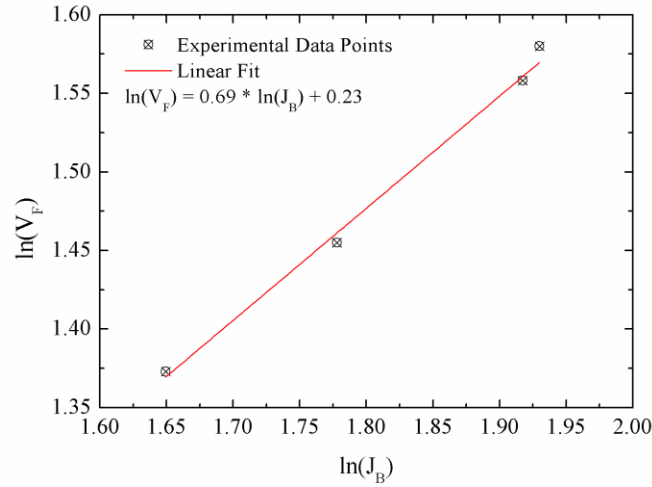
Fig. 3.1: Calculation of empirical constants in Gurney relation.

Once the empirical parameters of Gurney relation are known, it is possible to calculate the flyer velocity for different foil thicknesses keeping the flyer thickness (125 µm) same. For ELG-8 setup, skin depth in aluminum is found to be 232 µm. Therefore in our numerical calculations we have considered foil thicknesses varying from 6 µm to 100 µm.

Using Eq. 2.4 and Eq. 3.1 along with empirical constants, velocity of the flyer can be predicted for different foil width and thicknesses. Here the flyer velocities are calculated only for foils which explode before the current peak. Effect of thickness for three different foil widths is shown in Fig. 3.2 at a charging voltage of 30 kV. This plot shows that increasing the foil thickness beyond an optimum value does not help in achieving higher flyer velocities. To achieve higher flyer velocities it is more appropriate to decrease the foil width, like in case of 10 mm wide foil the rate of increase in velocity starts reducing after nearly 30 µm thicknesses, but for 8mm wide foil higher velocity can be achieved till 50 µm thicknesses.
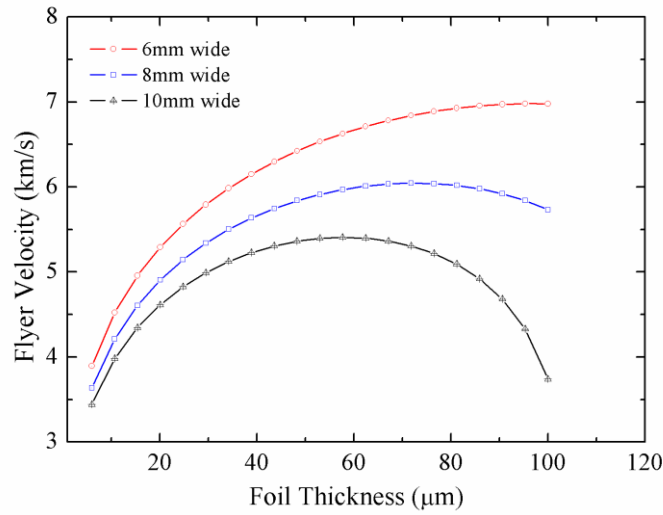
Fig. 3.2: Effect of foil dimensions on flyer velocity at 30 kV charging voltage.

This behavior can be explained by considering Eq. 3.1 where an increase in foil thickness cause a decrease in numerator due to reduction in J_B as well as in denominator due to its direct dependence on thickness. In the initial part of the graph denominator term dominates over the numerator term and there is an increase in flyer velocity but later vice versa happens and flyer velocity starts saturating or even decreasing afterwards. Though reducing the foil width is helpful
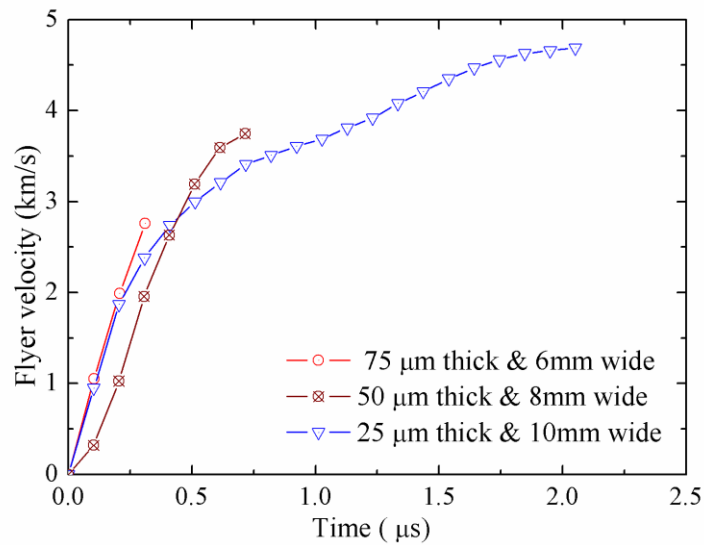
Fig. 3.3: Experimentally measured flyer velocity profile for three different foil dimensions.

in achieving higher flyer velocities but small diameter flyers also affects area available for shock diagnostics therefore flyers with diameter less than 6 mm are not considered for the present study.

To verify the above analysis velocity profiles of the flyers accelerated by three foils of different dimensions (i) 10 mm x 10 mm x 25 µm, (ii) 8 mm x 8 mm x 50 µm and (iii) 6 mm x 6 mm x 75 µm have been recorded using FPV and are shown in Fig. 3.3. These dimensions are chosen because of their practical availability and as per the outcomes shown in Fig. 3.2. To compare the three profiles the start time of flyer motion has been merged for all three foils though their burst times are different. It is observed that the intensity of reflected light in streak records for foil (ii) and (iii) are not sufficient to measure the full flyer trajectory. The possible cause may be the loss of reflectivity at higher acceleration or damage of the flyer due to shock loading. But the rise time in initial velocity profile is significantly higher in foil (ii) and (iii), which supports our analysis. Due to longer records obtained in foil of dimensions 10 mm x 10 mm x 25 µm, it has been considered as optimized dimensions for present study. Though we have reduced the width to 8 mm in some experiments but thickness was kept the same.

3.2 Effect of current rise time

In exploding foil systems, the rate of current rise decides the burst current density and hence the flyer velocity as per Eq. 3.1. But in any capacitor bank system it is not possible to change its parameters and current rise time. Therefore we have utilized the concept of opening switch to reduce the current rise time as also reported earlier [101]. The opening switch is an exploding foil that explodes and generates a sharp rising voltage pulse across its ends. During explosion the conducting metal foil rapidly converts in to non-conducting vapor phase, which results in fast rate of change of current (dI/dt) and leads to sharp voltage rise (L. dI/dt) across its

open ends, due to inductance (L) present in the circuit. To utilize this sharp voltage pulse for exploding foil accelerator, the whole assembly is designed in two stages. The first stage works as an opening switch and other as an accelerator. The equivalent circuit and schematic of two stage
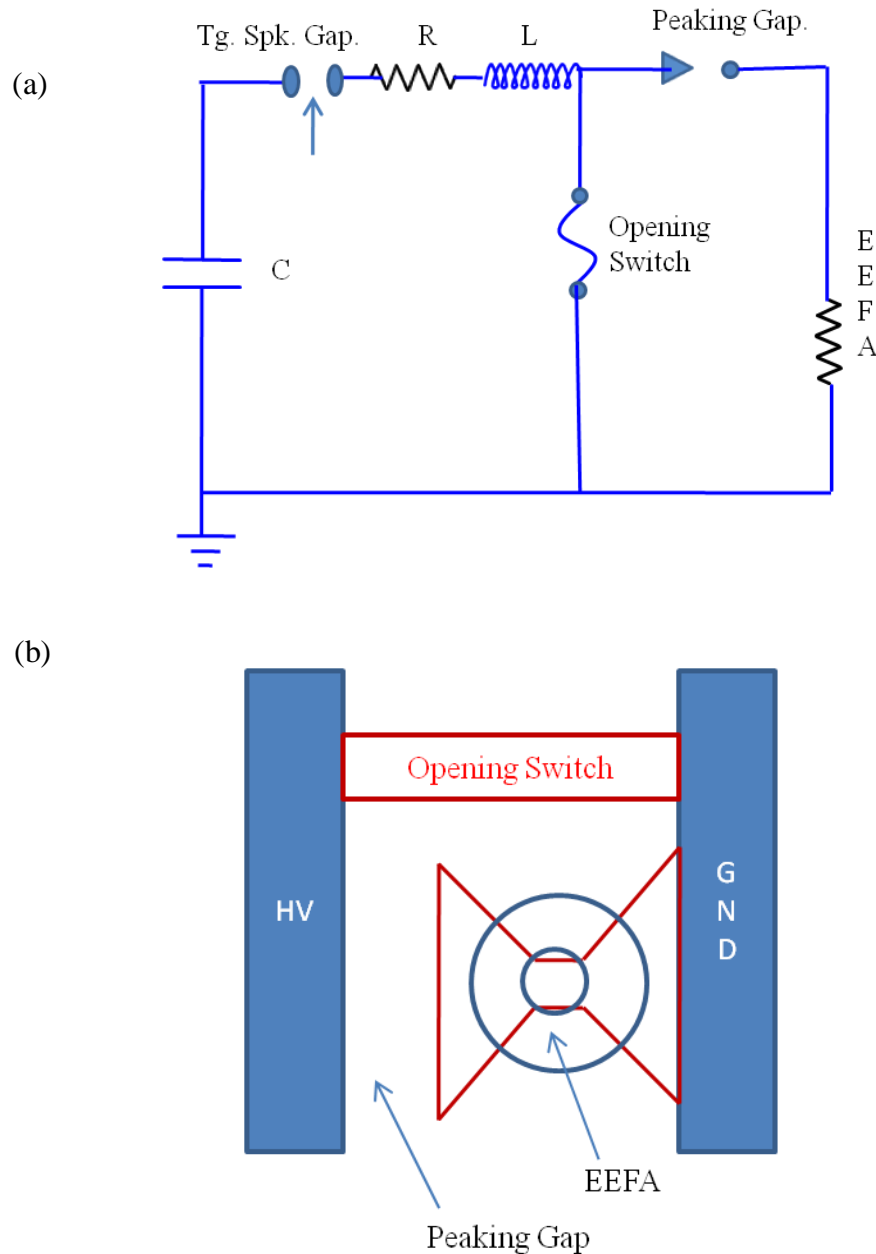
Fig. 3.4: (a) Equivalent circuit diagram and (b) schematics of two stage-exploding foil assembly. (EEFA: Electrically Exploding Foil Accelerator)

exploding foil assembly is shown in Fig. 3.4. The capacitance, inductance and resistance of the total circuit is expressed as 'C', 'L', and R' respectively. Here a peaking gap is implemented to avoid conduction of current through the accelerator stage during initial operation of opening switch. This peaking switch is designed by leaving a gap between exploding foil and high voltage electrode, which works as a surface discharge type switch. This peaking gap gets closed in the rising part of voltage peak generated by the explosion of opening switch directly placed between the high voltage (HV) and ground electrodes (GND), as shown in Fig. 3.4 (b). The sequence of operation is as follows: first the triggered spark gap gets closed by the application of an external trigger pulse and capacitor deposits its energy in the opening switch. Later due to fast opening of first stage, a voltage pulse is generated across the peaking gap which gets closed at a voltage decided by its gap. This switches the energy in to accelerator stage leading to explosion of second foil and acceleration of flyer.

In our experimental studies, we have used 13 µm thick aluminum foils having width of 5 mm and length of 30 mm for opening switch design. On the same Perspex base an exploding foil sandwich along with a peaking gap is also designed using same thickness of aluminum foil having widths of 5 mm and 8 mm. The gap distance was kept at 5 mm in initial experiments and was reduced later but no effect of gap distance on flyer velocity has been observed. Initial experiments were carried out with first stage of opening switch only to measure the circuit current and voltage across it. The measured calibrated waveforms are shown in Fig. 3.5 (a). A voltage pulse of 20 kV with rise time of 300 ns has been observed to be generated across the opening switch. Here the initial rise in voltage is due to contribution of inductive voltage (L'. dI/dt) in measurement, where L' is the inductance of transmission line lying between opening switch and voltage probe. The dip in current indicates the transformation of the metallic foil to

non conducting vapor phase. After the application of 20 kV pulse, a breakdown occurs either in

the vapor which is expanding due to thermodynamic forces or over the Perspex surface used for

foil support and current starts increasing again. Fig. 3.5 (b) shows the records obtained with two

stage assemblies, here the two peaks in voltage and significant fall in total circuit current clearly

indicates the predicted functioning of two stage assembly.
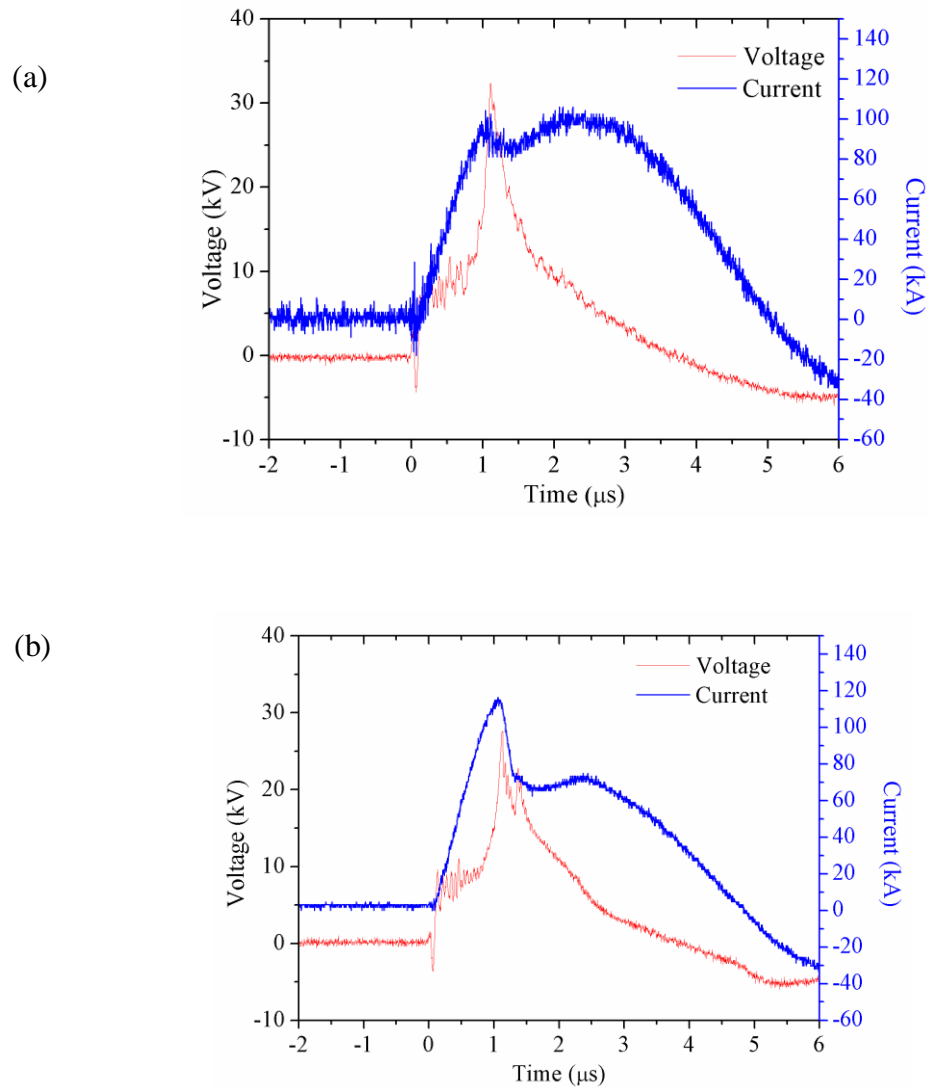
Fig. 3.5: Current and voltage measurements (a) across a single stage opening switch (b)
across a two stage assembly.

The experiments with two stage exploding foils have been carried out using two foil widths (5 mm and 8 mm) and the velocity measurements were carried out using Fabry-Perot velocimeter. The measurements with 5 mm wide exploding foil with and without the addition of opening switch (OS) stage are shown in Fig. 3.6 (a). Here it is found that flyer velocity is higher for the cases when opening switch is implemented, but the two steps observed in velocity profile are indicating the presence of shocks in flyer acceleration. The shock loading may deposit energy in the flyer and may damage it. Therefore one experiment is conducted with higher thickness flyer but flyer velocity could not be enhanced beyond 3.5 km/s. To further enhance the velocity

(a)

(b)
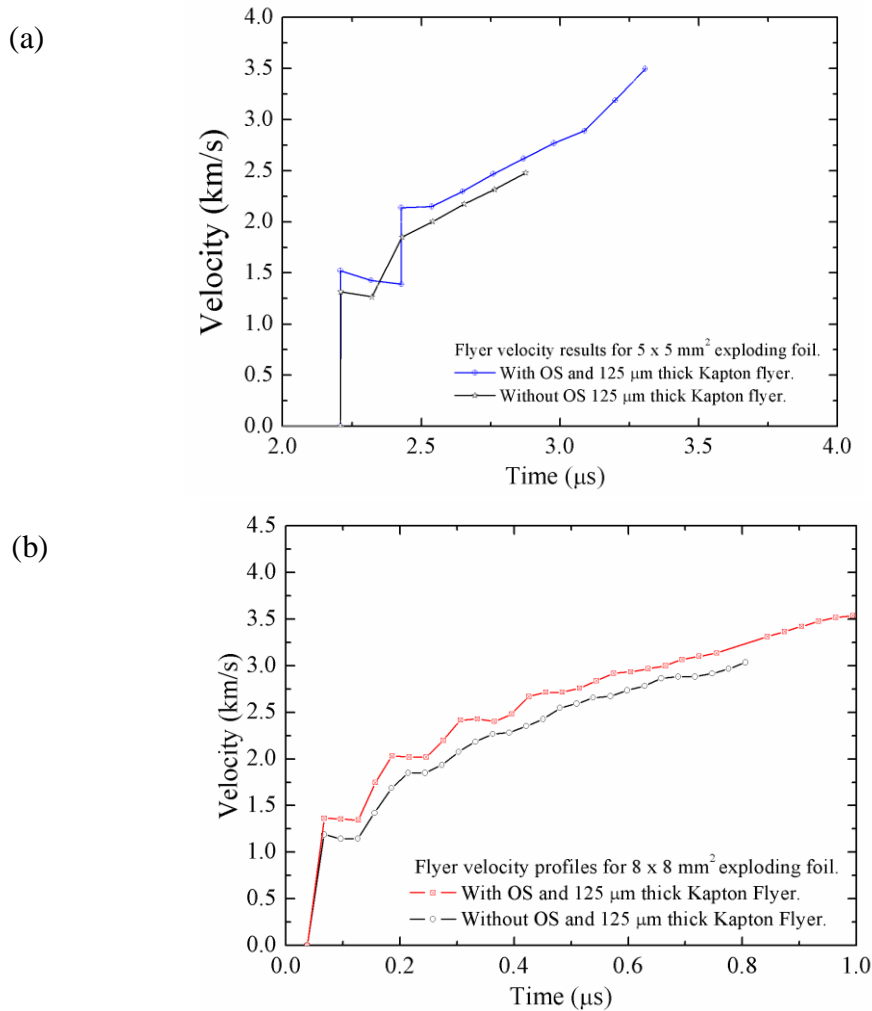
Fig. 3.6: Flyer velocity profiles for two stage and single stage exploding foil accelerators (a) for exploding foils of width 5mm (b) for exploding foils of width 8mm.

foil width has been increased to 8 mm to increase the deposited energy in the foil.   Fig. 3.6 (b) shows the velocity profiles, for two foils without opening switch and one foil with opening switch. For both the foil widths the velocity has been found to be enhanced by nearly 0.5 km/s, with the implementation of opening switch. Peaking gap has also been varied from 3 mm to 6 mm, but no significant effect has been found on flyer velocities. Therefore further research is diverted to optimization of other parameters to enhance the velocities.

3.3 Effect of barrel area: Flyer velocity enhancement by plasma propulsion

To achieve still higher flyer velocities that could produce pressures near to Mbar on present system, a scheme to generate additional plasma thrust on flyers has been conceived and experimentally investigated. The concept is to create an area over the foil which remains compressed under the barrel plane surface between inner and outer periphery. After explosion the foil generated plasma remains compressed in this region, while the pressure in barrel opening gets released due to puncture of flyer sheet. The high pressure plasma already present in the peripheral region rushes in to the barrel and provides an additional thrust on the flyer.   The schematic of exploding foil is shown in Fig. 3.7 (a) to elaborate this point.

To experimentally investigate this effect flyer velocity profiles were measured and compared for barrels of inner diameters ranging from 4 mm to 10 mm placed over exploding foils of dimension 10 x 10 mm^2. The comparative results are shown in Fig. 3.7 (b). Higher velocities were measured for smaller diameter barrels but after a certain inner diameter (6 mm) the terminal velocity of the flyer were found reducing. This appears to be caused by viscous forces, which became more significant in smaller barrel diameters. Using this scheme velocity upto 6.2 km/s was achieved on polyimide flyers of thickness 170 micron and diameter 6 mm

using exploding foils of dimension 8 x 8 mm^2. Achieving higher velocities with smaller width foils is also in accordance with our simulation results reported in Sec. 3.1. In this geometry we have also accelerated composite flyers of higher mass with a top layer of aluminum (100 μm) up to 4.5 km/s.
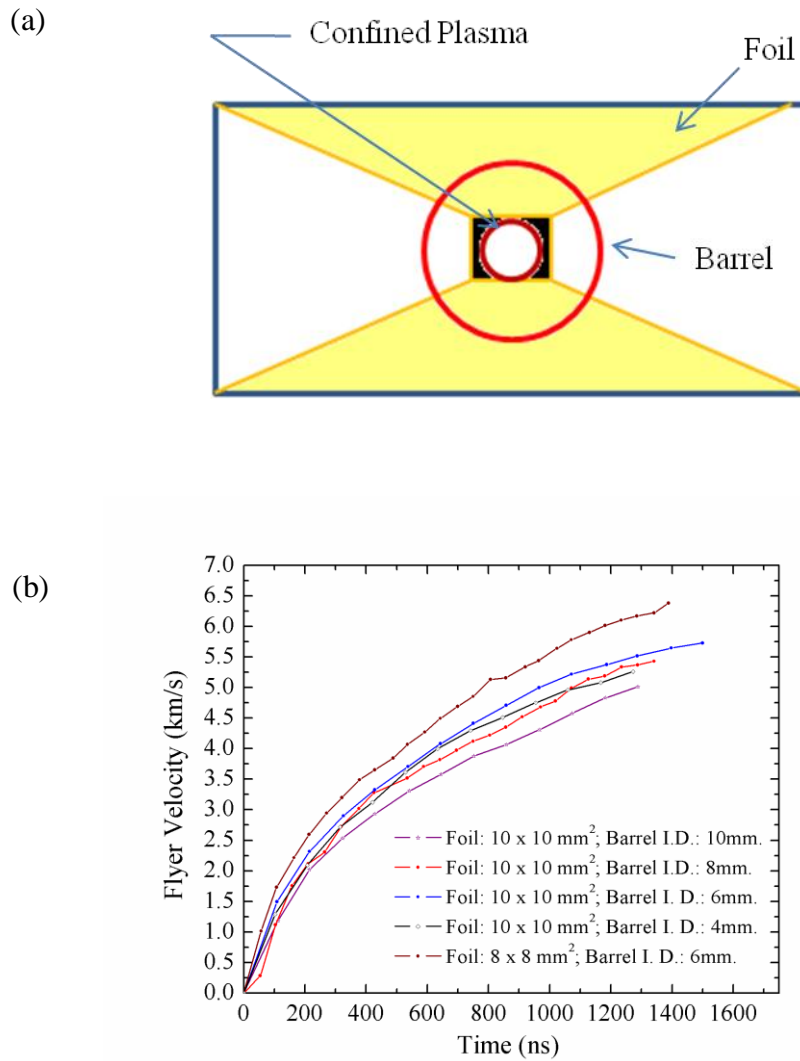
Fig. 3.7: Effect of barrel inner diameter on flyer velocity (a) schematics of exploding foil sandwiches (b) flyer velocity profiles for different barrel inner diameters.

3.4 Effect of barrel length and foil material

To carry out systematic shock studies it is necessary to achieve a range of flyer velocities. Different flyer velocities may be achieved by changing the capacitor bank charging voltage, which is sometimes difficult as it requires the variation of pressure or distance in the triggered spark gap switch. In present studies we have also utilized the change of barrel length, change of foil material and increase in flyer mass to achieve a variation in flyer velocity.

With the help of Fabry-Perot velocimeter, it is possible to record the complete flyer velocity profile over time. By the numerical integration of this profile, the flyer velocity for a given barrel length can be predicted. One such experimental result on aluminum exploding foil of thickness 25 µm and dimensions 10 x 10 mm^2 at a capacitor bank charging voltage of 34 kV is shown in Fig. 3.8 (a). Here it may be seen that a velocity variation from 3 to 4 km/s may be obtained by varying the barrel length from 2 to 7 mm. To achieve still lower velocities it is necessary to change the charging voltage, in the present system the minimum triggerable voltage is 16 kV and flyer velocity results at this voltage are shown in Fig. 3.8 (b). Here we have experimented with different flyer mass as well as different foil material. A velocity range from 2.5 to 3.0 km/s can be obtained by changing the barrel length from 2 mm to 8 mm. Further reduction in velocity was obtained when material of exploding foils was changed to copper and using composite flyers made of 125 µm thick polyimide sheet bonded to a 100 µm aluminum sheet (Fig. 3.8 (b)). In our equation of state experiments we have utilized the outcome of all these results to subject the target material at different pressures.
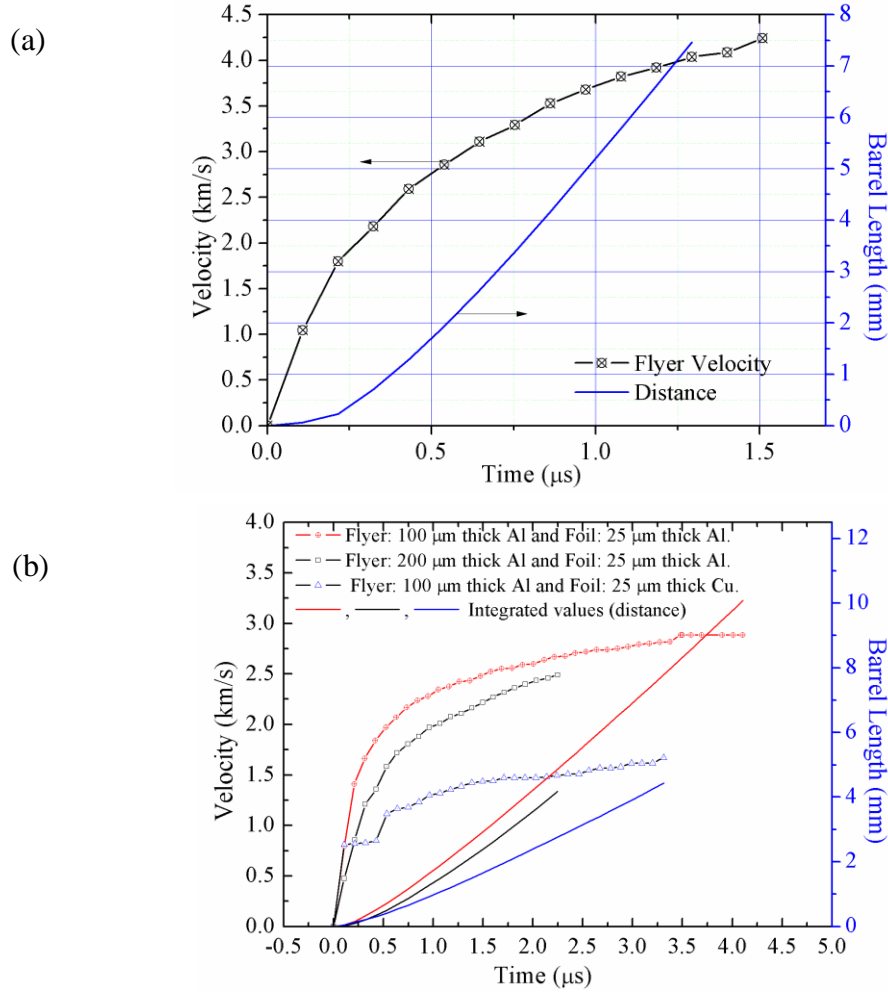
Fig. 3.8: (a) Effect of barrel length on flyer velocity at 34 kV charging voltage. (b) Effect of charging voltage, flyer thickness (mass) and foil material.

3.5 Effect of ambient pressure on flyer velocity

Due to presence of ambient air in the barrel, flyer experiences a drag force during its travel. To enhance the flyer velocity by reducing this air drag, an experimental investigation has been carried out on exploding foils operated in vacuum down to 10^{-4} mbar pressure. But instead of getting a gain, the velocity of the flyer has been found to be reducing with decrease in ambient pressure [125]. The terminal velocity of the flyer has been found to be maximum near to atmospheric pressure and minimum for measurements taken at 10^{-3} mbar pressure which

increases again at 10^{-4} mbar. The experimental velocity profiles measured by Fabry-Perot velocimeter on 25 µm thick and 10 x 10 mm^2 aluminum foils are shown in Fig. 3.9.
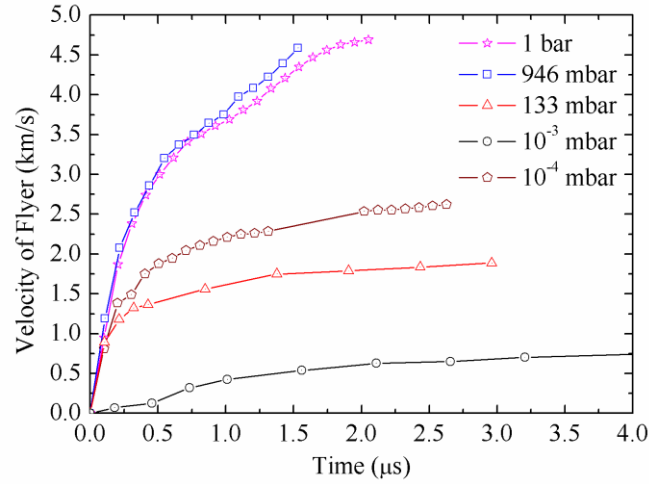
Fig. 3.9: Experimentally measured flyer velocity profiles at different ambient pressures.
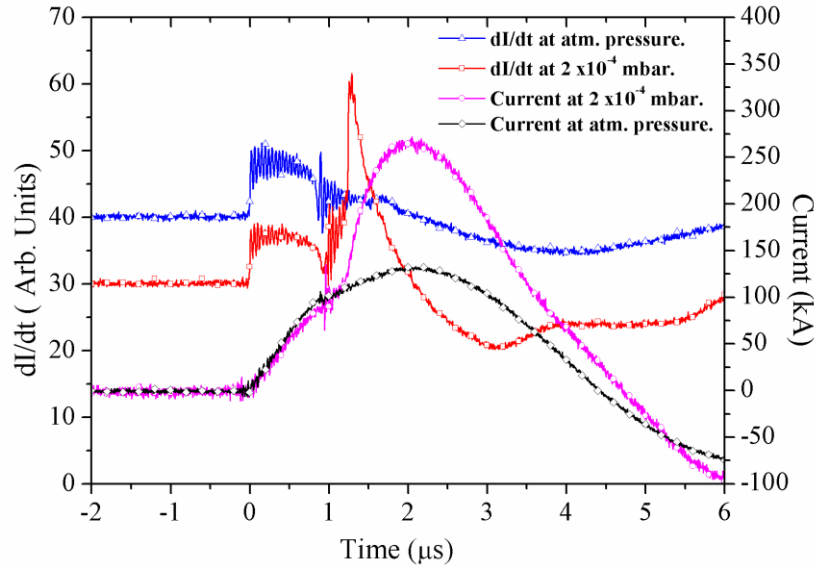
Fig. 3.10: Rate change of current (dI/dt) and current (I) profiles under vacuum and at atmospheric pressure.

To understand this behavior, current flowing through the foil and voltage across it has been measured using magnetic pick-up coil and Tektronix make P6015A probe placed across the transmission line outside the vacuum chamber respectively. Experiments have been carried out

with capacitor charged to about 28 kV, and the behavior of foil performance under vacuum (10^{-4} mbar) has been observed using direct (dI/dt) and integrated (I) output of pickup coil (Fig. 3.10). An anomalous rise has been observed in the current flowing through the foil after burst in contrast to its behavior near atmospheric pressure. To investigate this effect further, current and voltage measurements have been carried out with exploding foil operated at different vacuum levels ranging from atmospheric pressure to 10^{-4} mbar. The time of peak in foil resistance, is considered as the time of burst and used for differentiating the effect of vacuum. Current and voltage measurements have been used to calculate the foil resistance, energy deposited till burst and for 100 ns thereafter. The rapid transformation of exploding foil from conducting metallic phase to non-conducting vapor phase results in sudden rise in voltage across the foil till electric field across the electrodes becomes equal to the breakdown voltage of expanded vapor. As the foil dimensions (10 x 10 mm^2) were kept same for all the shots the developed peak voltage may be considered proportional to the dielectric strength of metal vapor. Vacuum has been created using a combination of rotary and diffusion pumps. No features of foil explosion were observed in pickup coil and voltage signals for vacuum levels ranging from 100 mbar down to 0.05 mbar. A very weak peak in voltage was observed in only a few experiments at 0.045 mbar, therefore this data was considered only for energy calculations. At these vacuum levels even the dielectric sheet was not found to be cut at all, therefore data points between 0.05 mbar to 100 mbar have not been considered for this study, but the important features of exploding foil behavior can be inferred from the measured values.

The voltage probe is placed outside the vacuum chamber, therefore it not only measures the voltage across the exploding foil, but also the inductive voltage (L'.dI/dt) developed across the short length of transmission line between exploding foil load and voltage probe. The

transmission line in present setup is designed in parallel plate geometry and following relation is used to calculate its inductance (L'):

$$L' = \frac{\mu_0 \times t \times l}{w} \tag{3.2}$$

In above relation 'μ_0' is the permeability of free space while 't' is the gap between the two current carrying conductors of length 'l' and width 'w'. As width and gap of transmission line vary in different sections therefore inductance of individual sections are theoretically estimated and total inductance is found to be 30 nH. The calibrated output of pick-up coil (dI/dt) was multiplied with this inductance value to estimate the induced voltage across the short length of transmission line. Voltages measured have been corrected by subtracting this induced voltage (L'.dI/dt) and their peak values are shown in Fig. 3.11 for different vacuum levels.
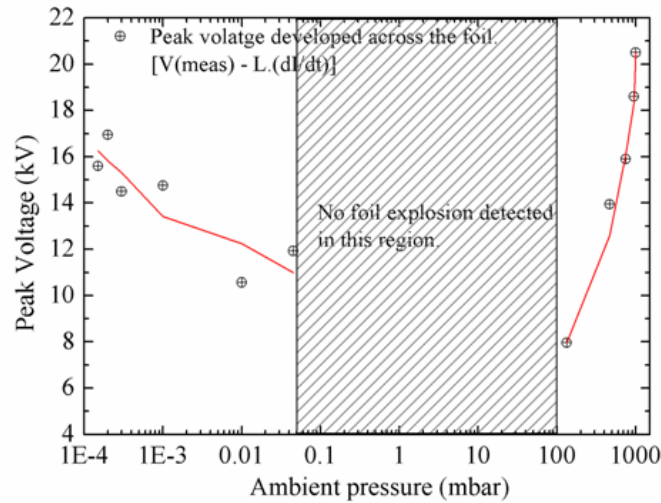
Fig. 3.11: Peak voltage measured across the foil at different vacuum levels.

The peak voltage developed across the foils at burst is found to be maximum for shots taken near to 1 bar and found to be increasing again from 0.05 mbar to 10^{-4} mbar but remains

less than its value at atmospheric pressure. The corrected voltage records along with current profiles were used to calculate the energy deposited in exploding foil by numerically integrating the temporal profile of power (voltage x current). Its value till resistance peak and additional energy deposited during a time interval of 100 ns after burst are shown in Fig. 3.12. The time interval of 100 ns is chosen because significant decrease in foil resistance has been observed during this period as will be discussed later. The energy deposited till burst and post burst phase, shows a slow decrease from 10^{-4} mbar to 0.05 mbar but at pressures slightly higher than 0.05 mbar it falls to very low values. Similar behavior is observed in the right portion of Fig.3.12, where from atmosphere down to 100 mbar pressure, deposited energy falls very rapidly. Therefore the pressure ranges typically from 100 mbar to 0.05 mbar may be termed as a dark region, where serious degradation in foil performance including absence of explosion is observed. The energy deposited in post burst phase for 100 ns duration is quite high (~170 J) at atmospheric pressure in contrast to its value (~80 J) at 10^{-4} mbar. Some variations in the measured values might have been caused by finite accuracies of voltage and current probes as
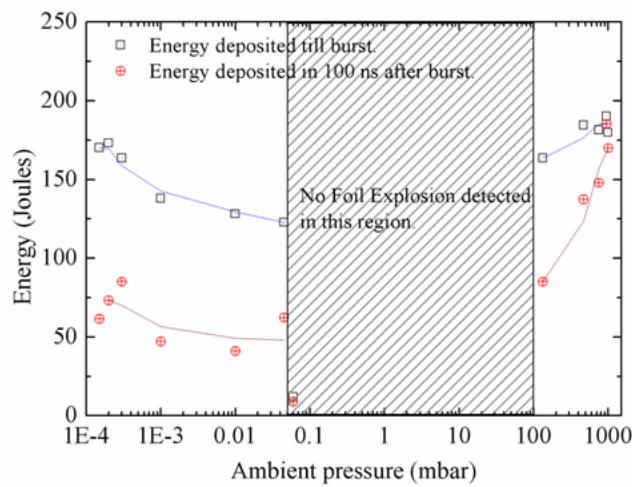
Fig. 3.12: Variation in energy deposition till burst and during 100 ns after burst.

well as due to the presence of electrical noise in the recorded signals. It is worthwhile to note here that the flyer velocity profile as shown in Fig. 3.9 has also been found to be following the same behavior as that of deposited energies, i.e. it is maximum for pressures near to 1 bar and decreases with reduction in pressure.

The value of peak resistance (at burst) has been found to be around 0.2 Ohm and nearly independent of vacuum levels except the dark region where it is found to be around 0.05 Ohm at 0.045 mbar pressure. Fig. 3.13 shows the variation of foil resistance with pressure, which indicates a sharp drop in its value after burst under vacuum as compared to atmospheric pressure regime. The reason for this drop might be the formation of a low impedance current channel parallel to the foil. This reduction in resistance also gives rise to an increase in overall current as observed in Fig 3.10. Possible reasoning about the formation of this low impedance channel is discussed in following section. A slight increase in the flyer velocity has been observed for foils operated near to 900 mbar, therefore if vacuum is desired then it should remain 50-100 mbar below atmospheric pressure.
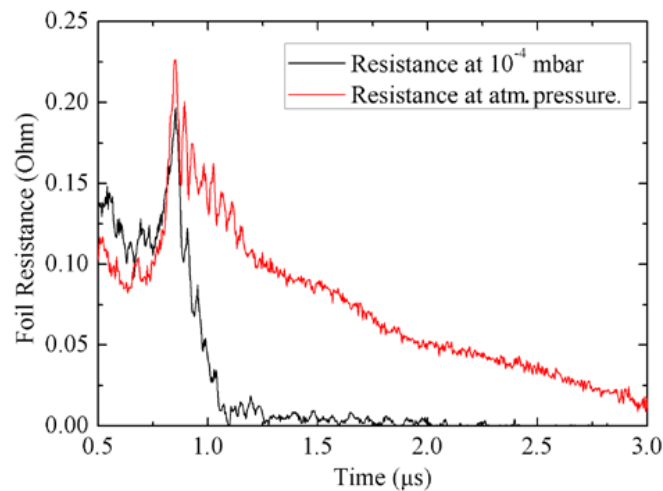
Fig. 3.13: Variation of foil resistance at two pressure levels.

3.5.1 Discussion

In the present investigations a serious degradation was observed in performance parameters of exploding foil, when operated under vacuum. The reason for this behavior appears to be caused by the formation of a low impedance path parallel to the exploding foil, which prevents subsequent deposition of energy in foil material. Here it may be noted that this low impedance path is not due to creeping discharge which normally occurs over the insulator surfaces. Though the foil is in contact with the insulator (flyer: Kapton), but the trend shown by peak voltage in Fig. 3.11, does not confirm the characteristics of creeping discharge which is reported [126] to be nearly independent of gas pressure in the range of 10^{-8} to 10^{-3} torr. This low impedance breakdown channel might be created by two possible mechanisms: (1) Ionization due to thermionic electrons emitted from the hot metal, as proposed for tungsten wires [127] and (2) Existance of a density gradient over the high density exploding foil vapour, which satisfies the condition for Paschen breakdown [127, 128] at a certain density value. The first reason is normally not considered for aluminum due to its lower melting temperature while the second is more plausible reason after burst as also mentioned in [128, 129]. But the decrease in energy and absence of explosion phenomenon in dark region cannot simply be justified by the second reason, as once explosion has not occurred; there is no high electric field developed across the foil. To understand dark region following points need to be considered:

1) The mean free path of the electrons calculated as per the relations given in Ref. 130 is larger than the foil length (10mm) for pressures lesser than 2 mbar therefore possibility of Paschen breakdown is weak.

2) Assuming the foil in liquid phase at its melting point (~ 660 ^{o}C) carrying approximately 50 kA current. In present configuration this current can deposit necessary energy to melt the foil material. At this point the theoretically estimated resistance of molten foil will be approximately 6 mΩ, which could develop an electric field of nearly 300 V/cm across its ends which are 1 cm apart and too small to initiate the vacuum breakdown.

In view of above points, it appears that the breakdown phenomenon in this region is assisted by the presence of magnetic field associated with the flow of high current through the foil and perpendicular to associated electric field. The presence of this cross field combination increases the electron path length which may initiate the avalanche breakdown in the metal vapour created by partial surface evaporation or in released adsorbed gases present over the foil surface. The electrons responsible for this initiation might be contributed by the partial dissociation of atoms at higher temperature [130] in the vicinity of molten foil material. Further in vacuum region from 100 mbar down to nearly 2 mbar, the Paschen breakdown voltage is also expected to be less in the vicinity of high temperature molten foil from its value at room temperature [130].

3.6 Investigations using 1D hydrodynamic numerical scheme

To validate the performance of the numerical scheme discussed in previous chapter, velocity profiles have been computed and compared with the reported experimental as well as simulated values of Lawrence Livermore National Laboratory (LLNL) 100 kV electric gun system [103], where two important cases were considered one in which foil explodes in the early stage of the current start and other near the current peak. The latter case is more significant to utilize the maximum part of the energy stored in capacitor bank.

The comparative results are shown in Fig. 3.14 (a) and Fig. 3.14 (b) for the two cases respectively. The velocity profiles and burst times predicted by the present formulation are found to be matching better with the experimental velocity profiles and also better than reported MHD [103] simulations for both the cases. Oscillating behavior observed in the predicted velocity profile in Fig. 3.14 (a) is due to the physical shock reverberations as also reported and observed in experimental profile [103]. Slightly more pronounced oscillations observed in Fig. 3.14 (b)
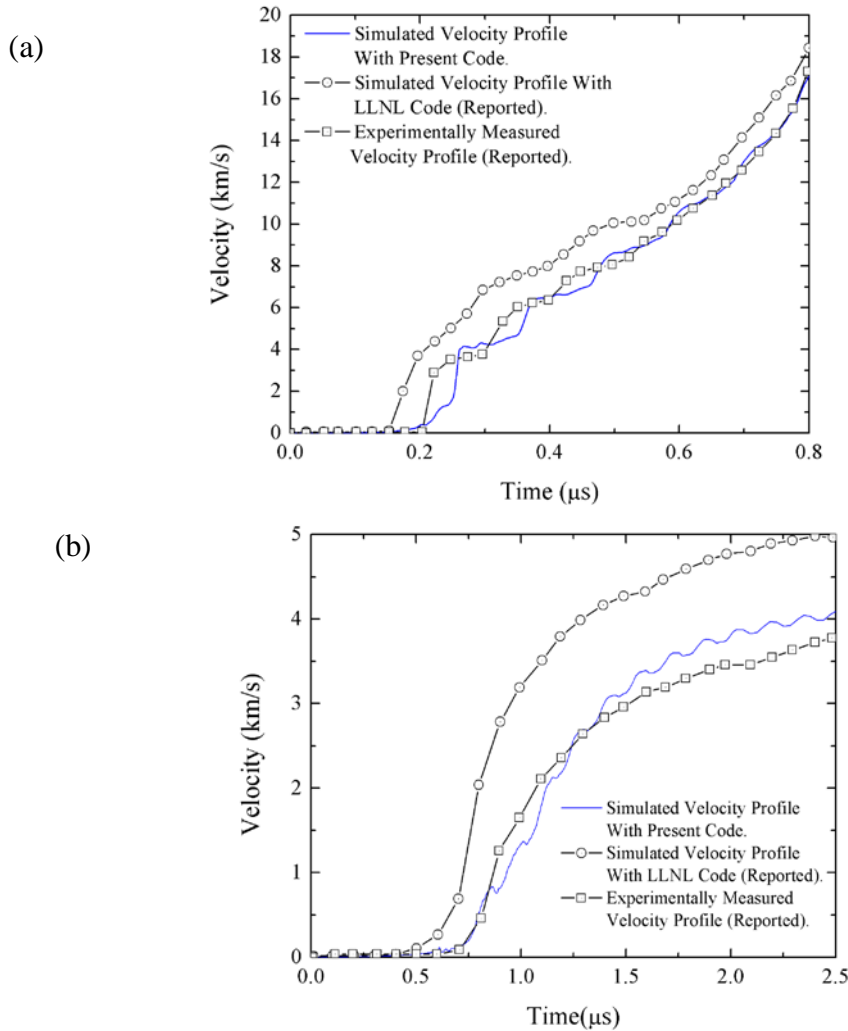
Fig.3.14: Comparison with reported results on 100 kV system of LLNL [103].
(a) For the foil exploding in the starting phase of the current start.
(b) For the foil exploding near the current peak.

appear to be caused by the shock reverberations and might not have been recorded experimentally due to larger time gaps between two reported experimental measurements. Another possibility for these oscillations could be the unavailability of empirical constants for generating the equation of state of Kapton, which are estimated by matching the Hugoniot generated by the present equation of state scheme with the reported results up to a compression ratio of two.

To validate the performance of the present code for different charging voltages, as reported on 40 kV and 100 kV banks [30], final velocities are simulated and results are compared in Fig. 3.15. Simulated values are found to be matching well with the reported experimental velocities within a maximum deviation of 1 km/s from the highest measured values on 100 kV and 40 kV banks using 102 μm thick foils. The reported experimental results on 100 kV bank using 51 μm foil appears to carry large experimental errors as the velocity measured at 100 kV charging voltage is nearly same as that of 68 kV charging voltage. The simulated values are predicting lower velocities but since the velocity profiles simulated earlier under similar foil/ flyer geometries with charging voltage 95 kV (Fig. 3.14 (a)) are matching well with the experimental values, therefore the results computed by present formulation are expected to be more realistic.

To assess the code performance on low energy bank, the experimentally measured velocity profiles on ELG-8 system is compared with the simulated values. The connection geometry of exploding foil in ELG-8 system is not exactly strip line near the connections. Therefore assumption for magnetic field boundary values as calculated for infinite parallel transmission line is not exactly valid. To account for this effect, the magnetic field boundary values are multiplied by a theoretically estimated correction factor for the present experimental

geometry. This correction factor is basically the ratio of magnetic field component perpendicular

to the current direction, generated by a finite conductor to that generated by an infinite

conductor. This one dimensional approximation is taken to consider the effect of finite size and

separation of transmission lines. To estimate this correction factor the transmission line geometry

is considered as a rectangular coil and expression for magnetic field is taken from Ref. 108. The

correction factor for the present exerimental geometry is found to be 0.88, i.e. the magnetic field

below the exploding foil should be 0.88 times the magnetic field computed for parallel infinite

conductors. It is further to be noted that in case of LLNL bank simulations, where the

transmission lines are 0.38 meter wide and are separated by 2 mm thick Kapton sheet, the

deviation of magnetic field from its value for the infinite conductors is less than 1% and the

assumption of infinite conductors remains fairly valid.
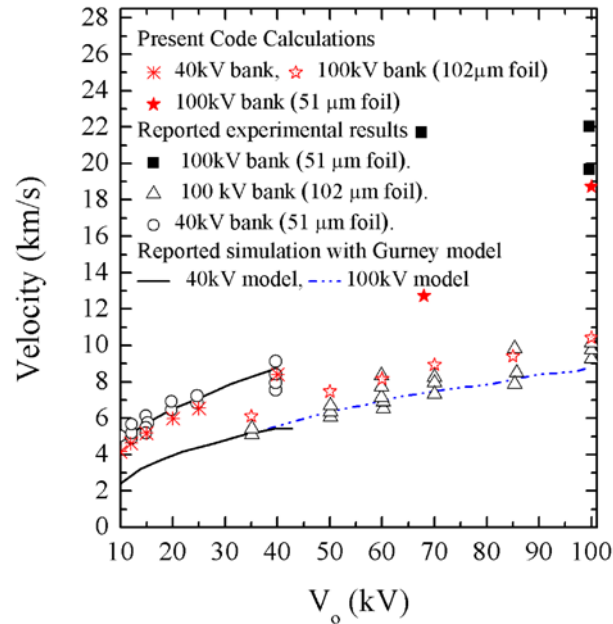
Fig. 3.15: Comparison with LLNL reported results [30] on 100kV and 40kV banks at
different charging voltages.
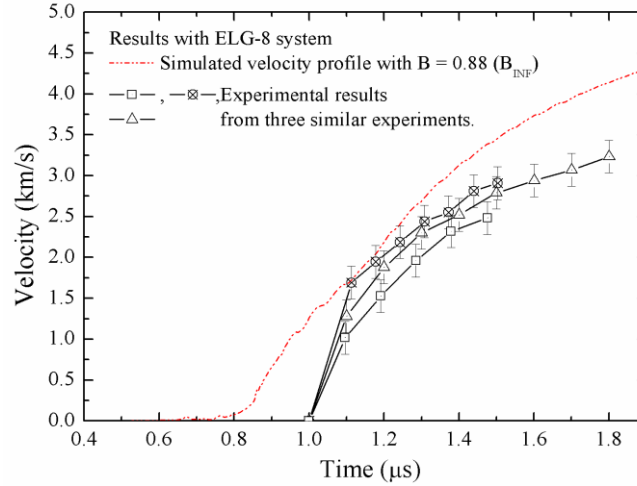
Fig. 3.16: Comparison of simulated and experimentally measured velocity profiles on ELG-8 system.

The comparison of experimental velocities inferred from the records of Fabry-Perot velocimeter in three similar experiments and numerically simulated velocity profiles computed with and without correction factor in magnetic field boundary values for ELG-8 system are shown in Fig. 3.16. The error bar corresponds to the finite experimental accuracies (0.2 km/s) associated with velocity measurements. In this case the shape of the simulated profile is nearly matching with the experimental profiles but a difference of 0.2 µs has been found in the burst times of two profiles. The simulated velocity is also nearly 1 km/s higher than the experimental values. This difference in burst time might be caused by the difference in exploding foil parameters used for simulation and used in experiments.

But if the burst time of simulated profile is shifted to match with the burst time of experimental profile then there is not much of a difference in their velocities. This indicates that small difference in burst times is causing a diference in burst current densities, hence in two velocity profiles.

Further this investigation is useful to decide the design parameters of a capacitor bank for any new system design to achieve a pre-decided flyer velocity. This comparison also indicates that strip line geometry is not only important for achieving low inductance but also to achieve higher flyer velocities. In present system it is not pssible to change the connection geometry but it may be useful for future designs.

3.7 Summary

In this chapter experimental studies are reported to optimize the performance of electrically exploding foil accelerator. A series of experiments have been conducted to determine the empirical constants for electrical analogue of Gurney formulation. Using this formulation foil thickness and width have been optimized to achieve flyers of higher velocity as well as better integrity during its travel. A concept of two stage exploding foil assembly has also been sucessfully explored to observe the effect of current rise time on flyer velocity. Although significant improvement could not be achieved but this concept may be useful for driving faster pulses from slow capacitor banks. A significant enhancement in flyer velocity was achieved by using barrel of diameter lesser than exploding foil cross-section. The additional force exerted by the compressed plasma helped in achieveing flyer velocities up to 6.2 km/s on 170 μm thick Kapton flyers and 4.5 km/s on 100 μm thick aluminum laminted composite flyers. To achieve a range of velocities, we have explored the effect of foil material, flyer thickness, barrel length and charging voltage. This resulted in flyer velocities from 1.6 km/s to 6.2 km/s. Another significant effect of ambient pressure on exploding foil performance has been studied and reported in this chapter. The measured current and voltage profiles across the foil under vacuum indicate a sharp decrease in deposited energy and foil resistance after burst. It has been concluded from these

observations that possibly due to formation of parallel low resistance plasma channel over the foil, current is diverted away from it and resulted in reduced flyer velocities.

This chapter also presents the validation results of developed 1D hydrodynamic numerical scheme against experimental and simulation data reported in literature. Numerically computed flyer velocity profiles and final flyer velocities have been found in close agreement with the reported experimental results with a significant improvement over reported simulations. Numerical modeling of present experimetal system (ELG-8) predicts the flyer velocity profiles higher than the experimental values, indicating a possibility of further improvement to achieve higher velocities.

Chapter 4

Shock Studies using Electric Gun

To characterize the electric gun setup as a projectile launcher for shock studies, a series of experiments have been carried out on different metals like tantalum, tin, iron, aluminum and copper. The experiments reported in this chapter have mostly been carried out using single beam Fabry-Perot velocimeter to measure the target velocity, while the flyer velocity was assumed from experiments conducted prior to that under similar conditions. In some materials like copper and tantalum fiber optic pins have been utilized to measure the shock velocity in stepped targets. The outcomes of these measurements were compared with the reported equation of state (EOS) data and found to be matching well within experimental accuracies, which proves the potential of present electric gun setup. A shock induced phase transition and corresponding two wave structure has been observed in iron near to 13.6 GPa pressure. The maximum pressure of 70 GPa has been generated and measured in tantalum. In this chapter an optical scheme conceived to measure the two velocities together using a single Fabry-Perot velocimeter is also discussed. Using this methodology equation of state of polyurethane based retro-reflective tape and aluminum has been measured at 12 GPa and 15 GPa pressure respectively.

4.1 Flyer planarity measurements

The planarity of the projectile at the time of impact is one of the crucial parameter in shock compression studies. The planarity of flyer may numerically be defined in terms of its tilt

and curvature. To experimentally measure it, a flat 100 µm thick copper target, fixed on a PMMA (Polymethyl-methacrylate) holder was used with electric gun system. An arrangement has been made in PMMA holder to place four optical fibers of core diameter 1.0 mm over the target through the holes created at mutually perpendicular position on a circle of diameter 6 mm as shown in Fig. 4.1 (a). These fibers were connected to fast photodiodes for detecting luminescence generated by shock breakout at the free surface of copper target.

This target assembly was symmetrically placed over the exploding foil barrel of diameter 9.8 mm and thickness 2 mm. The experiments were conducted at 16 kV charging voltage. The oscilloscope records showing the direct, integrated output of pick-up loop and signals from two fibers are shown in Fig. 4.1 (b). The initial slow rising signals in both optical fibers might be due to coupling of scattered plasma light generated by foil explosion while the fast rising signals afterwards indicate the time of shock breakout. The signals from all four fibers recorded in another oscilloscope are shown in Fig. 4.1 (c). The signals are seen to be in time sequence of 4,3,2,1 with delay of 1.20 ns, 2.56 ns, and 6.0 ns with respect to first fiber (fiber-4).

Considering a velocity of 3.2 km/s as measured in earlier similar experiments, these timings correspond to distances of 3.84 µm, 8.19 µm and 19.20 µm respectively, which indicate a tilt of 1.84 mrad along the current direction and 0.64 mrad perpendicular to it. It may be noted that this is the maximum deformation in the flyer over a diameter of 7.0 mm and for EOS experiments with FPV only central 1 to 2mm diameter of target is used, therefore a much better planarity may be expected in EOS measurements.

(a)

(b)

(c)
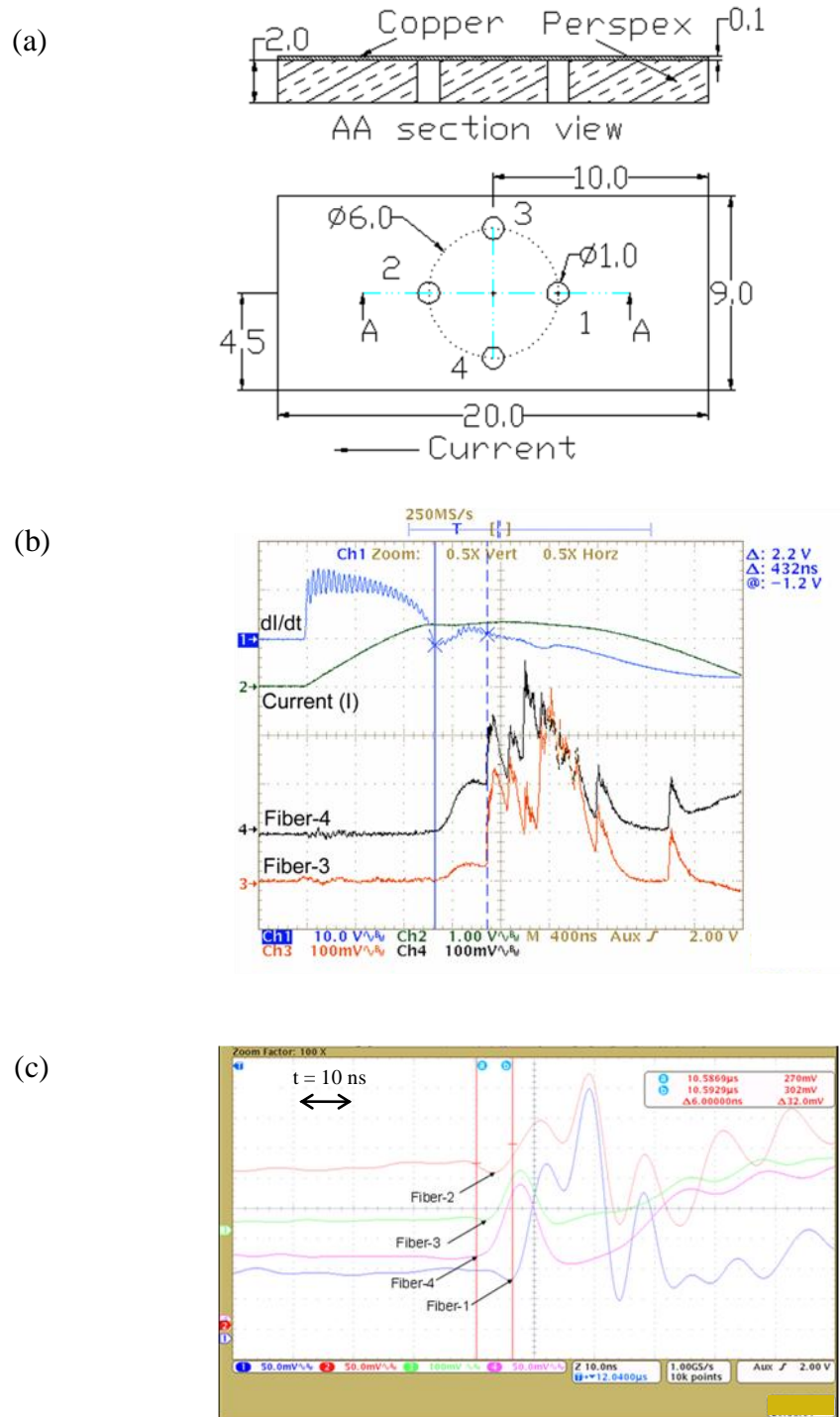
Fig. 4.1: (a) Schematic of target assembly to detect the shock breakout at target (copper) free surface using four optical fibers placed in a PMMA holder (b) Oscilloscope record showing direct, integrated output of magnetic pick-up coil and signals from fiber-3, fiber-4 (c) Signals from all four fibers recorded in another oscilloscope to measure the tilt in flyer.

4.2 Flyer velocity measurements

In most of the experiments presented in this chapter only single surface velocity is measured and to estimate the high pressure response of material flyer velocity is taken from prior experiments without target assembly. In such cases the repeatability of flyer performance becomes important and becomes the main accuracy determining parameter. Therefore before carrying out any shock experiment, few prior shots are taken to determine the flyer velocity. In most of the cases the velocity for a given barrel length has been found to remain within 10% of flyer velocity. The two such experiments carried out at a capacitor bank charging voltage of 28 kV and 34 kV using Kapton and aluminum composite flyers respectively, are shown in Fig. 4.2.
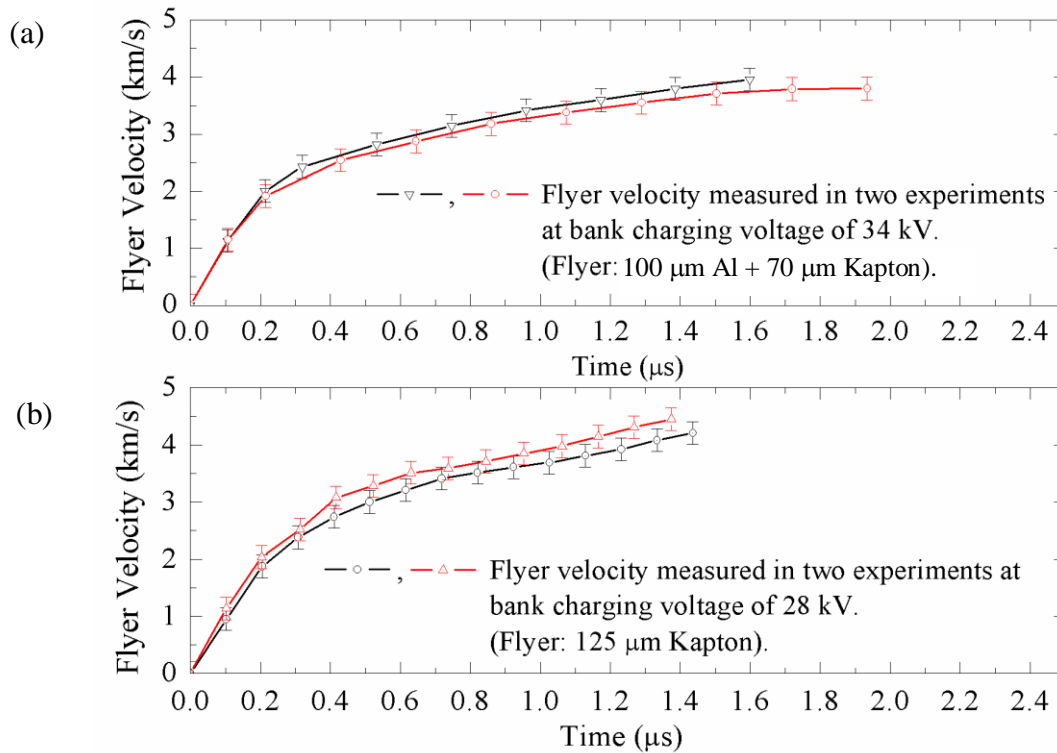
Fig.4.2: Flyer velocity measurements at bank charging voltage of 34 kV and 28 kV using (a) aluminum composite and (b) Kapton flyers.

Here longer records were obtained for aluminum composite flyers due to its higher fracture strength but flyer performance for both the cases has been found to be quite repeatable.

4.3 Target velocity profile measurements using single beam FPV

The objective of present experiments is to prove the potential of electric gun setup for high pressure studies and to record the velocity profile of impacted targets. To fulfill this aim, target of various metals have been prepared in planar forms and bonded to a suitable window material (soda lime glass/ LiF) of thickness 1 mm using a thin layer of epoxy (3-4 µm). The window helps in keeping the thin sheet of target material planar as well to avoid material ejecta during shock breakout from its otherwise free surface. The experimental configuration of these experiments is shown in Fig. 4.3 (a) and its representation in P-u_P plane is shown in Fig. 4.3 (b). Here it may be noted that a layer of aluminum is used only for composite flyers, in some experiments only. In P-u_P diagram (Fig. 4.3 (b)) the impact situation is demonstrated for an aluminum flyer moving with velocity 4 km/s. On impact with a tantalum target, it will generate a shock moving in forward direction (right) in the target and in reverse direction (left) in the flyer. Therefore the Hugoniot of flyer is reversed around the flyer velocity to represent the left going shock, while for target it is a normal right going Hugoniot from initial state (P = 0, u_P = 0). The intersection point (P_1, u_{P1}) of two Hugoniot curves gives the pressure and particle velocity in the target at the time of impact. When this right going shock reaches to target-window interface a similar situation is created with target now working as a flyer and window as the target. Hence due to symmetric nature of the curve, a left going Hugoniot reversed around the double of earlier determined particle velocity ($2u_{P1}$) is plotted to represent the target (tantalum) and a right going Hugoniot for window (LiF). Now the intersection point of two curves (P_2, u_{P2}) represents the state of window-target interface at the time of shock arrival.
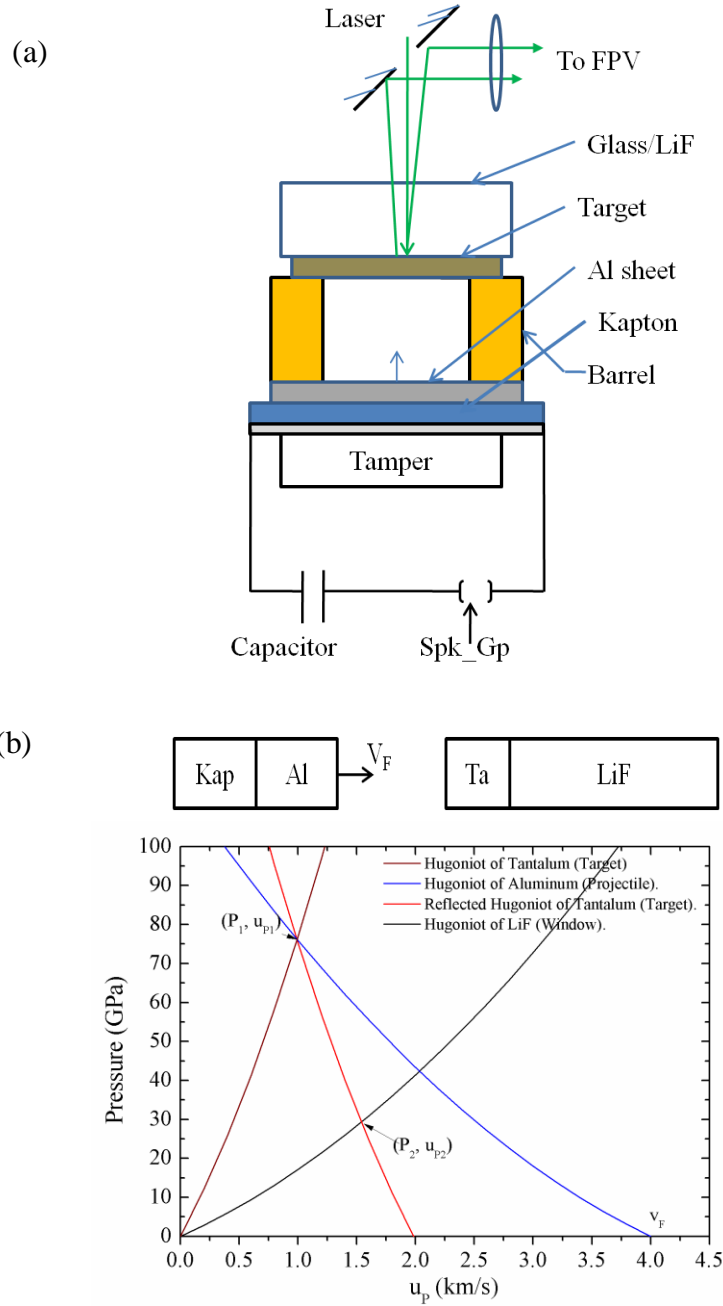
Fig. 4.3: (a) Schematic of experimental assembly for measurement of target-window interface velocity. (b) Representation of impact in P-u_P diagrams. Here projectile is aluminum, target is tantalum and window is of lithium fluoride (LiF).

In experiments the target-window interface velocity profile (u_{P2}) is measured using Fabry-Perot velocimeter. By knowing the Hugoniot of projectile as well as of target and its impact velocity (v_F), it is possible to predict the pressure and particle velocity at the time of

impact (P_1, u_{P1}) using measured target-window interface (P_2, u_{P2}) velocity. The comparison of measured values with those predicted by P-u_P curves indicates the capability of present system for equation of state studies.

4.3.1 Measurements on tantalum

In this section two experiments are reported on tantalum corresponding to a peak pressure of 27 and 70 GPa respectively. In these experiments, Fabry-Perot etalon with fringe constant 5 km/s is used to keep the fringe jumps small and well inferable. Low pressure (27 GPa) experiment was conducted at a bank charging voltage of 18 kV, using a barrel of inner diameter 9.8 mm and length 1 mm. In repetitive experiments the velocity of 125 µm thick Kapton flyer was found to be 3.2 ± 0.4 km/s at the time of impact for a barrel of length 1 mm. The obtained streak records and computed velocity profiles for Ta-Glass interface are shown Fig. 4.4 (a). A sharp jump observed in the interface velocity indicates the arrival of shock wave, after which the velocity remains constant for approximately 24 ns and then slowly decreases back to zero value after arrival and overtaking of rarefaction wave generated at the rear free surface of the flyer. The measured peak interface velocity in this case was 0.8 km/s, which matches well with the theoretically expected value of 0.72 km/s based on known Hugoniot data for Tantalum [131], Kapton [128] and Soda lime glass [132].

Similar experiment was carried out at bank charging voltage of 34 kV using a 6 mm diameter composite aluminum flyer of thickness 100 µm moving with velocity of 3.8 ± 0.4 km/s. The target was prepared from a 125 µm thick tantalum sheet bonded to a LiF window of thickness 1.0 mm. Here the data is presented in the form of pressure by converting the measured particle velocity into pressure using equation of state of LiF along with tantalum and is shown in

Fig. 4.4 (b). In this experiment the intensity of the reflected light was reduced considerably, due to higher shock pressure in tantalum, which has affected its reflectivity and resulted in lesser contrast in the streak record. Due to limited time resolution of streak camera the flat pressure region could not be determined accurately and rarefaction appears to be just following the shock.
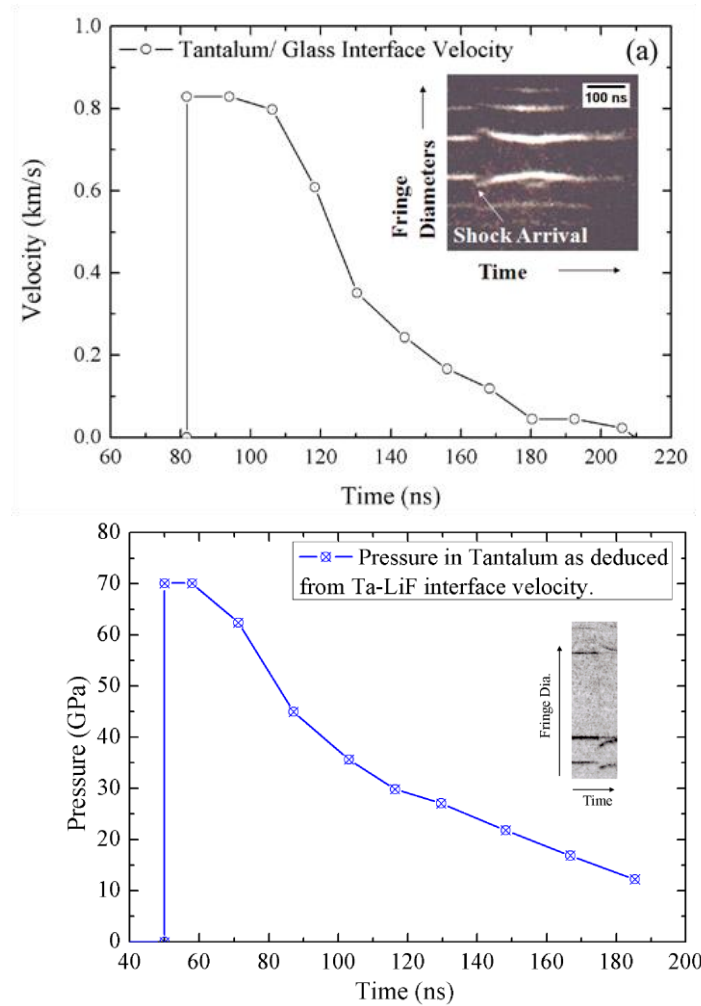
Fig.4.4: Shock studies on tantalum; (a) Particle velocity profile at an impact pressure of 27 GPa (b) Pressure profile at an impact pressure of 70 GPa.

The theoretically expected pressure in this experiment was 75.3 GPa, which is not very far from the measured pressure of 70 GPa and is within accuracy limit of 15% caused by the flyer velocity measurements as well as by Fabry-Perot velocimeter. Here the peak interface

velocity of 1.3 km/s is recorded, which is in good agreement with the theoretically expected value of 1.26 km/s for a flyer velocity of 4 km/s.

4.3.2 Measurements on tin

Studies similar to tantalum have also been conducted on 50 μm thick tin targets supported by a 1 mm thick soda-lime glass plate at a pressure of 48 GPa. This target was impacted by a composite aluminum flyer of thickness100 μm and diameter 6 mm, moving with a velocity of 3.5 km/s. The measured pressure profile along with streak record is shown in Fig. 4.5. Here also the measured peak pressure is found to be matching well with the theoretical estimations (46.6 GPa). To find the cause of sharp decrease in rarefaction profile, the hydrodynamic code discussed earlier has been utilized without any energy source to generate the pressure profile after impact. After analysis of code output this sharp step appears to be caused by the wave reflections at Al-Kapton interface.
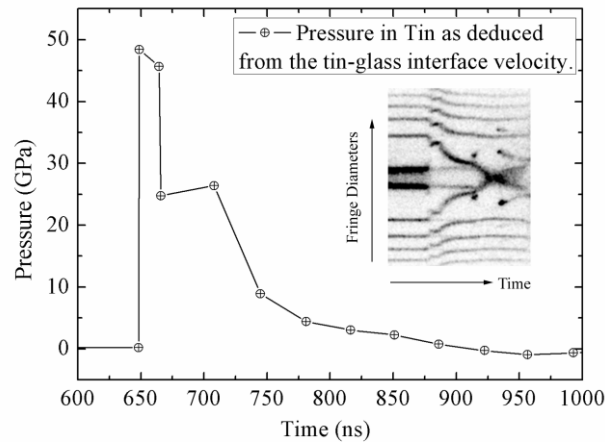
Fig.4.5: Shock studies on tin; pressure profile at an impact pressure of 48 GPa.

4.3.3 Measurements on iron

Iron is one of the important material found in earth core, and a reversible shock transformation is reported from a body-centered-cubic (α) to hexagonal-closed-packed (ε) structure above 13 GPa. We carried out a series of experiments on thin iron foils (100 μm) under shock loading from 20 GPa to 55 GPa and measured the target/ window interface velocity profiles. Pressure profiles deduced from Fabry-Perot records using equation of state of target, window and flyer materials are shown in Fig. 4.6. Due to change in density involved in phase transition, single shock splits in to two waves. A kink near 15 GPa has been found when the sample was subjected to a peak pressure of 44 GPa, indicating a polymorphic transition. At lower peak pressure near to 20 GPa, a clear two wave structure with a detailed release profile was recorded. The streak record showing the movement of Fabry-Perot fringe diameters under phase transition is also shown in inset of Fig. 4.6. Deduced pressure profiles show a transition in iron from bcc to hcp phase at 13.6 GPa under shock and a reverse phase transition in the release path at 10.8 GPa, where the slope of velocity profile becomes nearly flat after a sharp fall; which
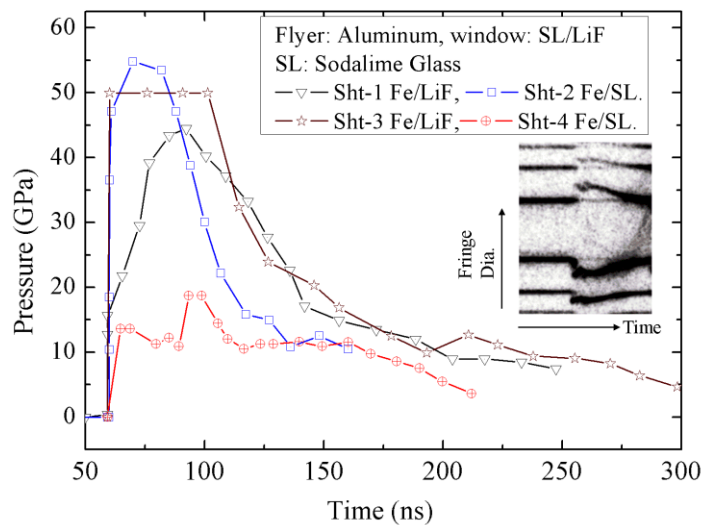
Fig. 4.6: Shock studies on iron, a phase transition is observed at 13.6 GPa pressure.

is well in agreement with the values reported in various literatures [43, 133].

4.4 Equation of state measurement using stepped targets

To determine the equation of state of any unknown material it is necessary to measure minimum two velocities. If shock velocity is measured in the impacted target and flyer velocity is obtained from some prior knowledge then the EOS data may be generated for any target material. To measure the shock velocity, target is normally made in stepped geometry of known step heights. The delay measured in the arrival of shock at different steps may be used to

(a)

(b)
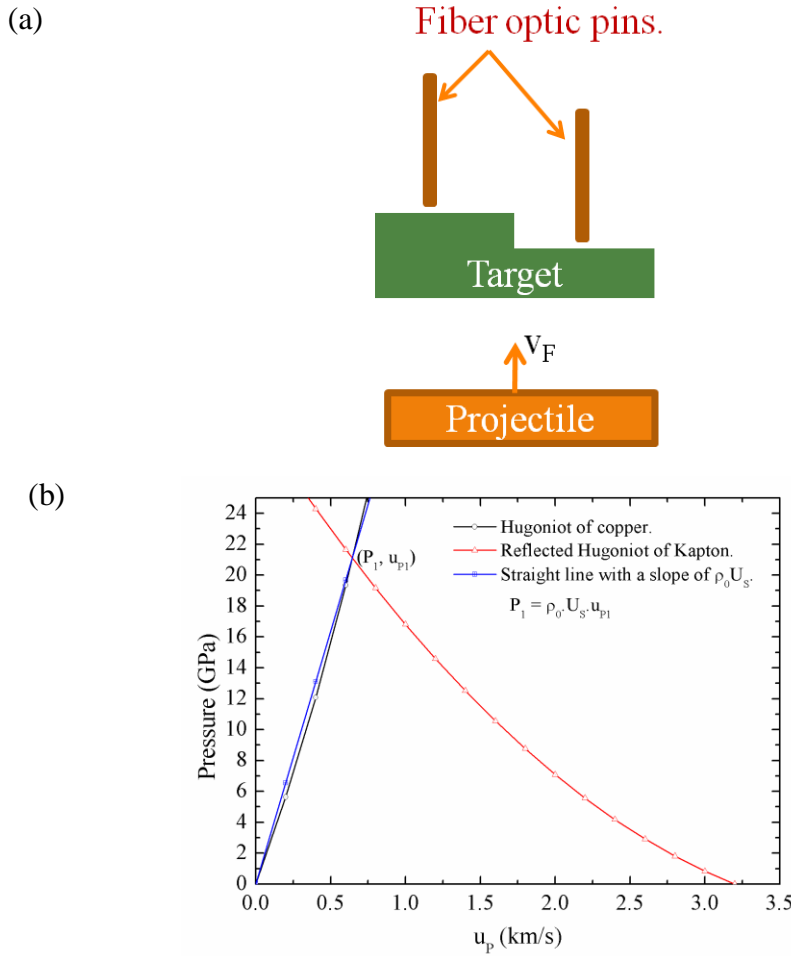
Fig. 4.7: Shock studies on step targets; (a) Experimental configuration. (b) Measurement of equation of state of copper.

compute the shock velocity. The experimental configuration is shown in Fig. 4.7 (a), the target is prepared in stepped geometry, with two fibers placed over them. The rise time of voltage pulses of photodiodes attached to fibers have been optimized near to 3 ns. The P-u_P Hugoniot curves depicting the impact situation for copper target is shown in Fig. 4.7 (b), here the target is impacted by a flyer of Kapton, moving with a velocity of 3.2 km/s. With the prior knowledge of flyer material and its velocity, it is possible to draw its Hugoniot reflected around the impact velocity (v_F) in P-u_P plane. Now by experimentally measuring the shock velocity (U_S), a Rayleigh line initiating from the origin with a slope of $\rho_0 U_s$ may be drawn for target. The intersection point of the Rayleigh line with flyer Hugoniot will provide the pressure and particle velocity (P_1, u_{P1}) at the time of impact corresponding to a point on the Hugoniot of target material.

In experimental investigations shock wave velocity measurements have been performed on stepped targets of copper and tantalum with step heights of 50 µm and 127 µm respectively. Due to small projectile diameter (~9.8 mm) and limitations of target preparation technique, only one step is prepared either by controlled chemical etching of copper or by bonding the two sheets of tantalum with top one having a through hole at its centre. Two polymer optical fibers with1.0 mm core diameter were placed in a Perspex target holder over the steps. The overall thickness of the target and position of fibers were kept such that the rarefaction wave originated from the free surface of flyer or step edges should not catch the shock before its break out at steps. But due to finite receiving cone angle of the fibers, the fiber placed on second step is prone to collect the light generated from the region near to step.

The fiber optic signals obtained with copper stepped target at 23 GPa are shown in Fig. 4.8 (a). A voltage pulse in the photodiode output indicates the arrival of shock wave and delay

between two such signals yields the shock travel time between the steps (50 μm). It can be observed from the oscilloscope records that the rise time of the light pulse for the fiber at second step is slower than that for the fiber at first step. The possible cause for this could be the collection of some portion of light by fiber from step edge, where shock strength is reduced due to arrival of rarefaction from the free boundary. Using the time delay between the two light signals, measured shock wave velocity in 50 μm thick step target of copper is found to be 4.4 km/s. In this experiment also the flyer velocity is taken as 3.2 km/s from previous measurements

(a)

(b)
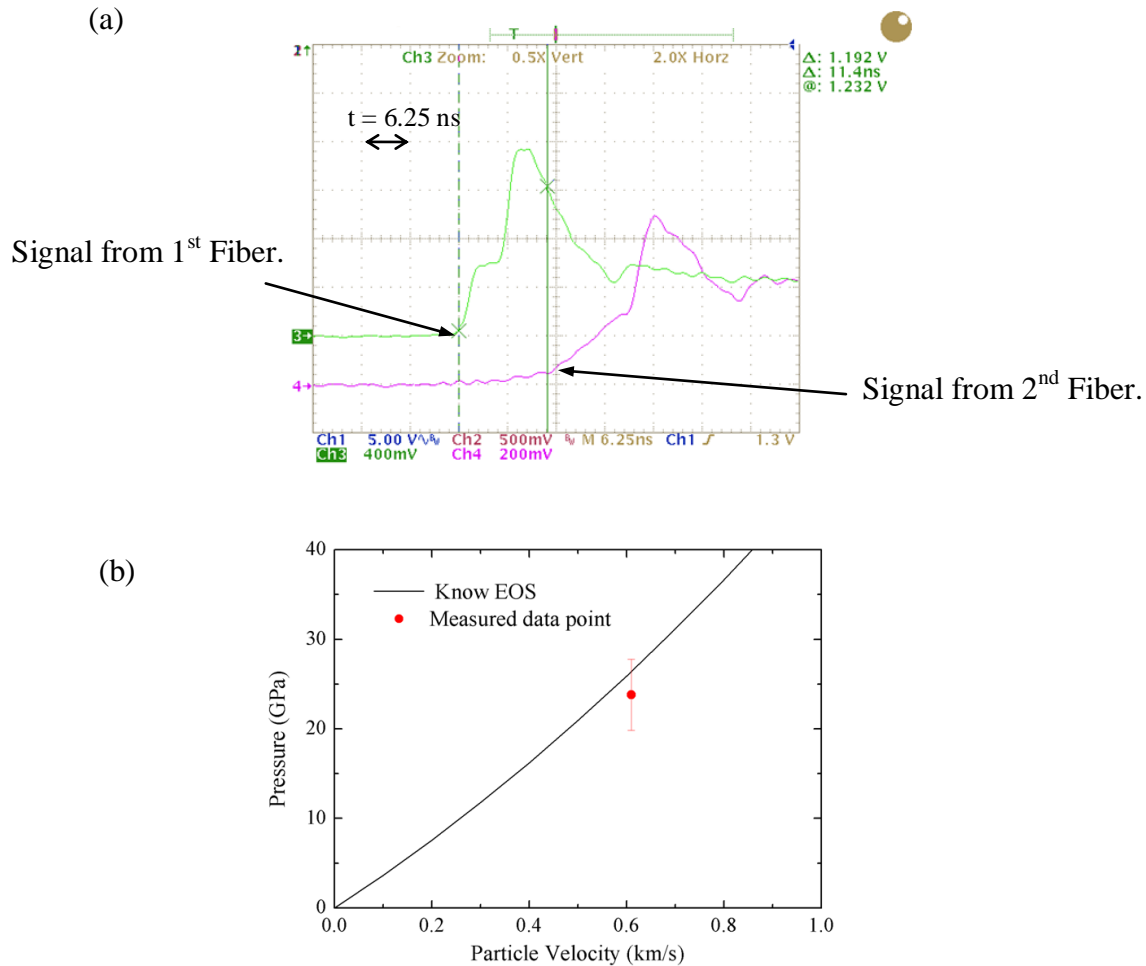
Fig. 4.8: Equation of state measurement of copper impacted by a polyimide (Kapton) flyer of thickness 125 μm moving with velocity of 3.2 km/s. (a) Fiber optic signals. (b) Comparison of measured data with the known Hugoniot. (Errors in pressure are ~17%)

as the placement of target obstruct the flyer view and made it difficult to launch laser light. Using this data impact pressure and particle velocity is calculated and shown along with the known Hugoniot of copper in Fig. 4.8 (b). The measurement errors are calculated by considering the errors in measurement of target thickness and time difference between two signals.

Similar experiments were conducted on tantalum target with a step size of 127 μm, impacted by a Kapton flyer moving with a velocity of 4.7 km/s. This target was designed by bonding a 25 μm thick tantalum foil to another 127 μm thick tantalum foil having a hole at its center to collect the shock generated light from the first step. The measured shock velocity was found to be 4.1 km/s, which corresponds to a pressure of 48 GPa. The comparison of measured equation of state data with the known Hugoniot of tantalum is shown in Fig. 4.9.
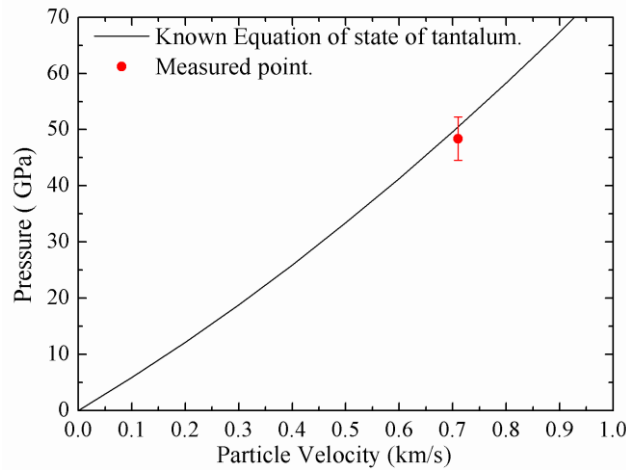
Fig.4.9: Equation of state measurement of tantalum impacted by a Kapton flyer of thickness 125 μm moving with velocity of 4.7 km/s. (Errors in pressure are ~7%)

The equation of state data for both the measurements hav been found to be matching well with the reported Hugoniot within experimental errors. To reduce such errors and to simultaneously record the flyer as well as target velocity another scheme based on Fabry-Perot velocimeter is developed and is discussed in next section.

4.5 Two velocity measurements using single FPV

Simultaneous measurement of projectile and free surface velocity of target (or target-window interface) is important for any shock compression experiment. One possibility is to use two Fabry-Perot velocimeters but it requires two streak cameras and two interferometers for measuring velocities of two surfaces, which makes such measurements complex and expensive. In our first approach, a possibility of using single FPV for two surface velocity measurements is experimentally explored. The simplified experimental configuration is shown in Fig. 4.10. The laser light is launched in such a way that it illuminates both the surfaces under study and reflected light coming from the flyer as well as from the target is used to generate interference fringes. In this arrangement, during the initial flyer movement, expanding fringes are expected to be seen in the streak record along with unchanged fringes produced by the fraction of light reflected from stationary target. After impact, these unchanged fringes would also show a jump according to the movement of target surface. Therefore by recording both fringe movements on same record, velocity profile of both the surfaces can be computed.
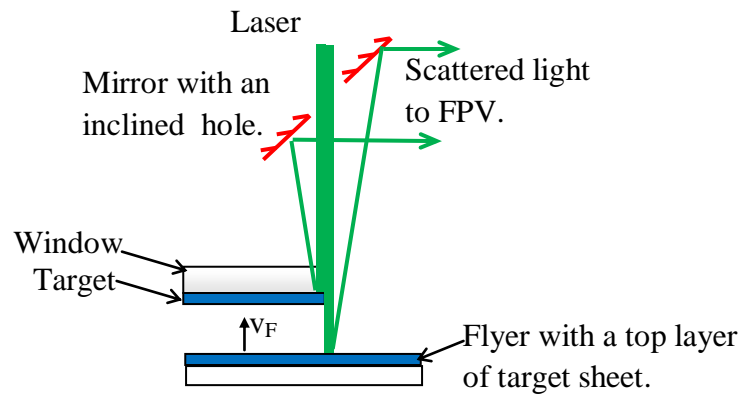
Fig.4.10: Experimental geometry for two velocity measurements using single FPV.

The experimental viability of this concept has been confirmed by measuring the equation of state data of polyurethane based retro-reflective tape at 12 GPa and aluminum at 15 GPa. Initial experiments have been carried out on a 30 μm thick retro-reflective tape, which is used because of its good reflective properties maintained even on the arrival of shock. The projectiles made of retro-reflective tape (30 μm) bonded over the Kapton sheet (125 μm) were accelerated in a barrel of length 2 mm. These projectiles were impact on the target made of 30 μm thick retro-reflecting tape supported by a 1 mm thick soda-lime glass plate. Time evolution of fringe diameters with computed time resolved velocity profiles of both target and flyer are shown in Fig. 4.11 (a). The initial part of the streak record shows the fringe movements according to flyer movement along with stationary fringes generated from the stationary target. At a later stage on impact these stationary fringes also show a jump corresponding to the movement of tape- glass interface. The analysis of obtained streak record shows a flyer velocity of 3.1 km/s and tape-glass interface peak velocity of 1.6 km/s. As retro-reflective tape is mostly made of polyurethane with a thin reflecting metal layer, the EOS of polyurethane as reported in Ref. 131 is used for the theoretical prediction of interface velocity. On comparison measured peak interface velocity has been found to be 30 % higher than this theoretical prediction which might be due to the presence of metallic layer of unknown thickness embedded in the tape.

The results of experiments carried out in a similar way on 30 μm thick aluminium target impacted by a 30 μm aluminum flyer bonded to 125 μm thick Kapton are shown in Fig. 4.11 (b). In these experiments though the major portion of the laser spot is focussed on target but due to loss in reflectivity on shock arrival the fringe intensities are low. The analysis of obtained streak record shows a flyer velocity of 2.3 km/s and aluminium-glass interface peak velocity of 1.2 km/s, which has been found to be matching well with the reported EOS data within experimental

accuracies of 8%, which is higher in present case due to finite absolute error (± 0.2 km/s) involved with the present FPV measurements, but at higher pressures or at higher velocities contribution of this error will become less significant.

(a)

(b)
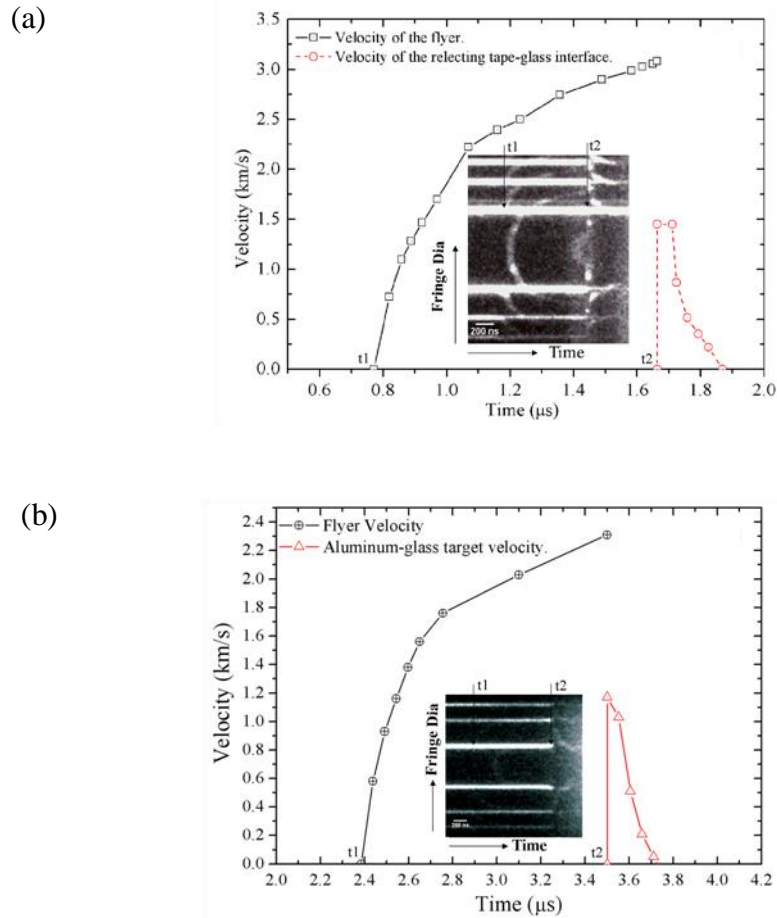
Fig.4.11: Streak record of FPV and inferred velocity profiles (a) for retro-reflective tape at 12 GPa (b) for aluminium at 15 GPa. (t_1= Time at which flyer movement starts, t_2= Time at which target-glass boundary moves.)

4.6 Summary

Experimental studies performed on electric gun setup to access its performance as a shock generating device are presented in this chapter. These studies include the measurement of

crucial flyer parameters like its planarity, which has been found to be order of few mrads. After confirming the planarity of flyer and its velocity reproducibility (<10%), the material like tin and tantalum were subjected to a shock pressure of 48 and 70 GPa respectively. The measured particle velocities have been found to be matching well with the theoretically estimated values based on reported Hugoniot of target, flyer and window. These studies were further extended to determine the phase transition in iron. A series of shock compression experiments have been carried out on iron foils from 20 GPa to 55 GPa and a two wave structure corresponding to a phase transition from α to ε phase has been recorded near to 13.6 GPa, which is well in agreement with the values reported in literature. To generate the equation of state data for any unknown material experimental geometry has been changed and stepped target of copper and tantalum were prepared. Using fiber optic pins shock velocities were measured to produce the equation of state data at 23 GPa and 48 GPa for copper and tantalum respectively, which has been found close to their reported Hugoniot. To extend the capabilities of present Fabry-Perot velocimeter to measure the two velocities together, a scheme has been proposed and experimentally verified on aluminum and retro-reflective tape at 15 GPa and 12 GPa respectively.

Chapter 5

Equation of State Measurements in Zr and Ti Metals Using Dual Beam Velocimeter

The shock loading characteristics of any material can be determined by precise measurement of two velocities at the time of impact for a given experimental geometry. In one possible configuration these velocities may be projectile (flyer) velocity and the free surface or target window interface velocity of impacted target. In last chapter the concept of two surface velocity measurement has been experimentally demonstrated by using half the laser beam for illumination of target while other half for illumination of flyer and carried out the equation of state (EOS) measurements on polyurethane based retro-reflective tape and aluminum targets. But this type of arrangement puts a restriction on the placement of target as well as it poses difficulty in controlling the laser energy distribution over the target and flyer. In many experiments it is desired to concentrate more laser energy on target than flyer due to severe degradation in target reflectance on shock arrival. Therefore necessary modifications has been carried out to measure the equation of state (EOS) points with better accuracies using two beams of unequal intensities derived from a single laser. The details of this velocimeter have already been discussed in Chapter-2. In this chapter, using this velocimeter the characteristics of titanium and zirconium metal foils under shock loading have been studied up to 16 GPa and 12 GPa pressure respectively. The flyer velocity optimization techniques reported earlier in Chapter 3 have been implemented to accelerate flyers at different velocities. The measured equations of state data for

both the metals have been found to be well in agreement with the reported Hugoniot, within the experimental accuracies. A phase transition from α (hcp) to ω (hexagonal) phase has been detected near to 11.4 GPa for titanium and 8.2 GPa for zirconium in the rising part of target-glass interface velocity profile.

5.1 Importance of the study

Many research groups have studied the high pressure behavior of these metals using facilities like gas gun [8, 134], explosives [9, 10], high power proton beam source, [9] and a transition from hcp (α) to hexagonal (ω) phase has been reported over a wide pressure range. The published phase transition pressure under shock loading varies from 6.2 GPa [7] to 8.3 GPa [8] for Zr and 5.1 GPa [9] to 11.9 GPa [10] for Ti. These variations are attributed to pressure levels in high purity titanium by Razorenov *et al.* [9] and to pressure exposure time, hydrostaticity of the pressure, microstructure and impurity concentration by Sikka *et al.* [11] in general. Various theoretical and experimental studies have been carried out to understand the effect of impurities, peak shock stress, and texture on phase transition kinetics [12-17]. It has also been reported [8] that phase transition pressure in Zr increases from 7.1 GPa to 8.3 GPa with an increase in impurity content typically from 0.02 to 0.1 % by weight and no signature of phase transition was found in particle velocity profile for an impurity of 1.8 wt %. Most of these studies have been carried out on thick samples and very few have reported results on thin foils [9] where shock loading time is comparatively small.

In present study thin foils have been experimented under short duration pressure loading and outcomes are compared with those reported on thicker specimens. These measurements have been carried out on thin (127 μm) metal foils with overall purity of 99.5% for Zr whereas 99.99 % for Ti and the results have been found close to those reported on comparatively much thicker

samples. Zirconium samples used in this study are of relatively higher overall impurity concentration (0.5 %) than reported earlier [8], but no significant change in phase transition pressure is observed. In this work the use of dual beam Fabry-Perot velocimeter (FPV) has also been reported first time to simultaneously measure the velocity profiles of projectile as well as of target-window interface. The details of experiments will be discussed in following sections:

5.2 Experimental methodology for EOS measurements

The experiments have been carried out under symmetric impact conditions when flyer and target are of same material. For symmetric impact a sheet of target material is bonded over the dielectric flyer (Kapton) of thickness 125 μm, using a thin layer (typically 3-5 μm) of epoxy. The material under study (target) is bonded to a suitable transparent window and placed over the barrel in such a manner that it covers only half the barrel area, leaving other half for measurement of flyer velocity similar to that shown in Fig. 4.9 or in Fig. 2.10. The flyer velocity was varied by charging the capacitor to different voltages.
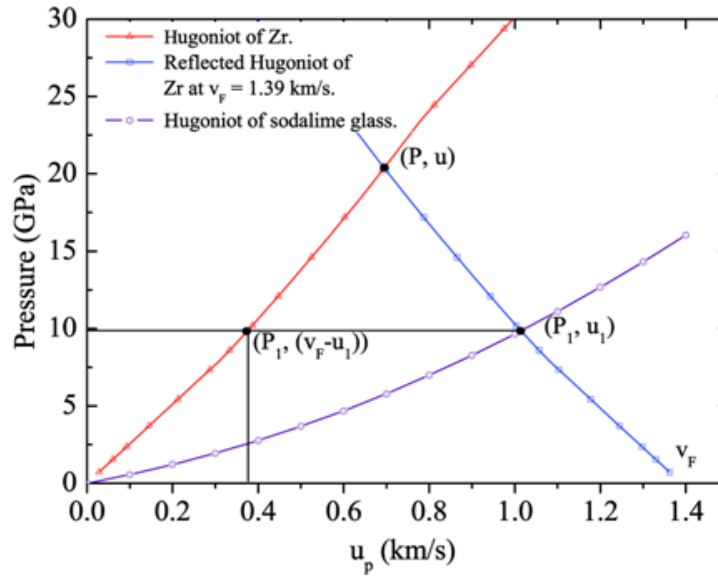
Fig. 5.1: P-u$_P$ diagrams illustrating the methodology of EOS measurements of target material.

To illustrate the measurement methodology of shock experiments, impact situation is demonstrated for zirconium in Fig. 5.1 using known Hugoniots in P-u_P plane. In this figure right going P-u_P curves are plotted for target (zirconium [135]) as well as for window material (soda-lime glass [132]) and left going Hugoniot reflected around flyer velocity 'v_F' (1.39 km/s) for the flyer. Here the value v_F =1.39 km/s is taken as it corresponds to one of our experimental results. On impact a shock of pressure 'P' and particle velocity 'u' is induced in the target which on arrival at target-window interface induces another shock of pressure 'P_1' and particle velocity 'u_1' in the window material. Now in target material the pressure falls from 'P' to 'P_1' along its reflected Hugoniot. The fall in pressure occurs due to lower shock impedance of soda-lime glass, which is a low cost window material but reported to remain transparent up to 24 GPa [136].

In our experiments with dual beam FPV the velocity profiles of flyer as well as of target-glass interface has been recorded on a single streak camera. The flyer (v_F) and target-glass interface (u_1) velocities at the time of impact are deduced from these records. Using the known EOS of window material, the pressure P_1 at the target glass interface can be calculated and due to symmetric nature of impact this pressure also corresponds to a particle velocity of (v_F-u_1) on right going Hugoniot of target material. Hence the point [P_1, (v_F-u_1)] represents a shocked state on Hugoniot of target material.

5.3 Experimental results and discussion

Commercially available metal foils with overall purity of 99.5 % for zirconium and 99.99 % for titanium have been used for this study. The X-ray diffraction patterns of both the foils have been analyzed to infer the qualitative information about texturing. It is found that both the foils

have preferred orientations along the compression axis. Zirconium is found to be more textured

along *[002]* direction, while titanium along *[103]* direction. Using the peak widths of XRD data

typical average grain size of 0.23 μm and 0.26 μm is found for Zr and Ti respectively, indicating

the presence of large grains in foils.

Table 5.1

Summary of Experimental Results

Experiment No.	*Flyer/ Target material*	*Impact velocity* v_F *(km/s)*	*Peak interface velocity* u_1 *(km/s)*	*Particle velocity (u_P) in target* v_F- u_1 *(km/s)*	*Peak pressure at interface (GPa)*
Ti-1	Titanium	1.59 (±0.025)	1.16 (±0.065)	0.43 (±0.09)	12.02 (±1.01)
Ti-2	Titanium	1.97 (±0.042)	1.38 (±0.075)	0.59 (±0.117)	15.69 (±1.32)
Zr-1	Zirconium	1.32 (±0.043)	0.97 (±0.074)	0.35 (±0.117)	9.26 (±1.03)
Zr-2	Zirconium	1.39 (±0.067)	1.02 (±0.065)	0.37 (±0.132)	9.88 (±1.02)
Zr-3	Zirconium	1.64 (±0.03)	1.18 (±0.065)	0.46 (±0.095)	12.25 (±1.05)

Overall purity of metal foils: Ti: 99.99 % and Zr: 99.5 %.
Thickness of flyer and target: 127 μm.

To measure the EOS of these metal foils, five symmetric impact experiments have been

carried out using dual beam FPV.   The details of these experiments are summarized in Table

5.1. The simultaneously measured velocity profiles in experiment Ti-1 are shown in Fig. 5.2

along with streak record showing the evolution of fringe diameters with time. The

superimposition of two fringe patterns can easily be seen in this record, the expanding fringe

diameter since t = 0 along with a new fringe afterwards at centre are representing the movement

of flyer. The fringes that maintain a constant positions till t =1 µs, and show a sudden jump

afterwards represent the movement of target-glass interface.
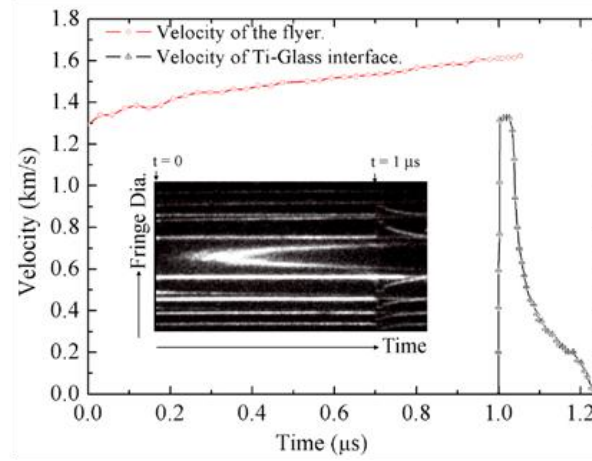
Fig. 5.2: Simultaneously measured flyer and target-glass interface profiles for experiment no. Ti-1, and streak record showing the movement of interference fringes corresponding to both the surfaces. The camera recording starts at time t = 0, when the flyer has already achieved a velocity of 1.3 km/s and later impact happens at t = 1 µs.

The velocity profiles are generated by visual marking of fringe positions at different time

instances and using the Eq. 2.33. But to determine EOS points accurately, fringe intensity

profiles have been generated by digitalizing the streak record along a line at the time of impact

and peak of intensity profiles of each fringe has been used to determine its position. The

accuracy of fringe positions is now limited by the resolving power of streak camera which is 20

lp/ mm in the present setup and corresponds to an accuracy of 0.2%. These accuracies are

reflected in measurements of D_{L0}, D_{L1} and also in D_{R0}, therefore the total absolute measurement

errors are estimated by Taylor series expansion as described by Eq.2.36, around these parameters

up to first order. As computed values represent total absolute error therefore the error bars shown

in Table 5.1 are taken as half of these values. These errors in velocities at interface are also used

to compute the errors in pressure by using EOS of window material. The total error in particle

velocity (v_F-u_1) is large in present experimental setup as it includes the errors of both individual velocities v_F and u_1. To reduce this error one possibility is to more accurately fit the spatial profile of interference fringes to equations of Fabry-Perot interferometer, and other is to measure the free surface velocity of target to estimate the particle velocity. As the free surface velocity measurements will involve only single velocity so error will be reduced to nearly half of its present value, but one needs to maintain the planarity of target foil which may be bonded to a flat

(a)

(b)
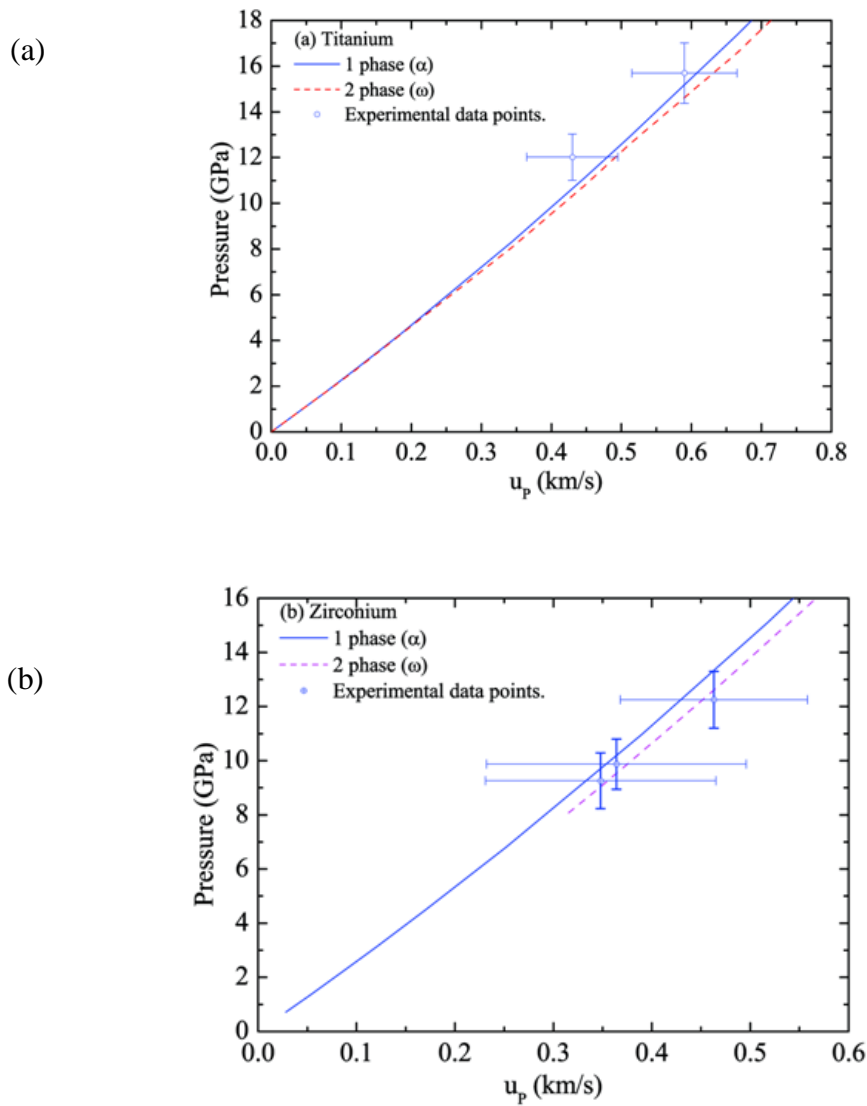
Fig. 5.3: Comparison of experimentally measured data points with the reported Hugoniot curves for (a) Titanium [137] (b) Zirconium. [135]

surface with a finite size hole for laser illumination.

The measured EOS points, shown in Table 5.1 are compared with the reported Hugoniot of target materials as shown in Fig. 5.3 (a) and Fig. 5.3 (b) for titanium [137] and zirconium [135] respectively. The slight deviations in measured pressures appears to be due to difference in Hugoniot of commercially available soda-lime glass used in present study to that reported in literature. But the present measurements demonstrate the capability of dual beam FPV in shock experiments which may be improved further with more careful choice of window materials.
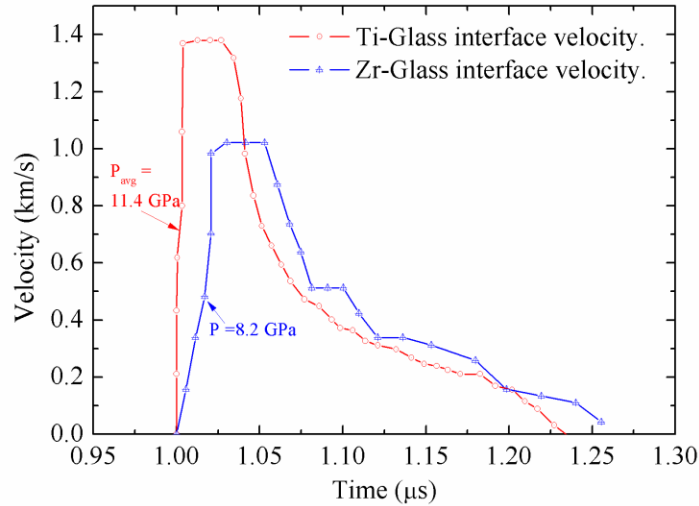
Fig. 5.4: Detailed velocity profiles of target-glass interface for titanium (experiment no. Ti-2) and zirconium (experiment no. Zr-2). The pressures shown near kink are estimated by using reported EOS of target and window materials. For Ti, due to finite temporal resolution of FPV, the transition pressure is taken as the average of two points across the slope.)

A weak kink has been observed in the rising part of glass-target interface velocity profiles of titanium as well as that of zirconium. This appears to be caused by the well reported α to ω phase transition under shock loading, but due to weak contrast in streak pattern at the rising portion of shock arrival this feature was visible in only a few records. In case of Ti the rise time of particle velocity profile is too fast to record the exact position of slope change near phase

transition. Figure 5.4 shows the detailed target-glass interface profiles for experiment no. Ti-2 and Zr-2. By doing reverse calculations using EOS of target materials, [131] it is possible to predict the pressure at kink as 8.2 GPa for zirconium but for Ti, due to finite time resolution (~3ns) of present Fabry-Perot velocimeter, two points were observed over the kink ends separated by 4 ns. Therefore the transition pressure was approximately averaged over these two end points of the kink as 11.4 GPa ± 1.6 GPa. This transition pressure for Ti is near and within experimental accuracies to its value (10.4 GPa [134]) reported on high purity thicker samples. But for zirconium measured transition pressure is close to that reported (8.3 GPa [8]) on samples of impurity concentration 0.1 wt %. In these experiments instead of a clear two wave structure, a weak kink has been observed in the shock loading profile. The finite time resolution of velocimeter, smaller thickness of target foil and high shock pressures developed in it on impact with flyers (~20 GPa for Zr and ~26 GPa for Ti) appears to be responsible for this behavior leading to short shock duration.

5.4 Summary

The capabilities of electric gun setup along with dual beam velocimeter has been validated by equation of state measurements on zirconium and titanium metals under shock loading up to pressures of 12 GPa and 16 GPa respectively. The concept of dual beam Fabry-Perot velocimeter has been successfully demonstrated by simultaneously measuring the velocity profiles of target as well as that of flyer using a single streak camera and laser. This improvement in FPV makes shock diagnostics economic and operationally simple. Measured EOS data on thin foils has been found to be matching well with the data reported in literature on relatively thicker samples. The detailed velocity profiles of target-glass interface show a weak kink in its rising part indicating a phase transition from α to ω phase. The transition pressure in

present study is found to be approximately 8.2 GPa for zirconium (overall purity 99.5%) and 11.4 GPa $\pm$ 1.6 GPa for titanium (overall purity 99.99%). To improve the accuracies of present velocity measurements, further work to fit fringe intensity profiles using equations of Fabry-Perot interferometer, will be done in near future to enable better prediction of peak positions at different time instances with smaller error and better confidence.

Chapter 6

Conclusions and Future Scope of Studies

The present thesis reports the development and optimization of a portable shock generation technique as well as its diagnostics to study the shock loading behavior of different metals. In this quest the performance of an electrically exploding foil accelerator of energy 8 kJ has been optimized to accelerate flyers from 1.5 km/s to 6.2 km/s. To enhance the shock impedance of flyer a thin sheet of aluminum has also been bonded to the polyimide (Kapton) and velocities up to 4.5 km/s has been achieved. In initial experiments the flyer performance was characterized in terms of its velocity, planarity and integrity. A typical asymmetric tilt of 1.8 mrad along the current direction and 0.6 mrad perpendicular to it at a flyer velocity of 3.2 km/s has been measured by recording the shock breakout at four mutually perpendicular locations on the free surface of a planar target. To achieve higher flyer velocities in a controlled and repetitive way an investigation has been carried to study the effect of various experimental parameters like foil dimensions, current rise time, barrel inner diameter, and ambient pressure. During optimization, the empirical constants for electrical analogue of Gurney formulation have been experimentally determined by measuring the flyer velocity at different burst current densities of exploding foil. Using the concept of action integral along with Gurney formulation, the effect of foil widths and its thickness on flyer velocity has been predicted. To achieve faster current rise time pulses from the existing capacitor bank, concept of two stage exploding foil assemblies is explored, where first stage works as an opening switch to generate a 20 kV/ 300 ns voltage pulse,

which is fed to another second stage of exploding foil accelerator.   In the above two experimental investigations, a faster rise and small increase in velocity profiles have been detected for optimized foils but final velocities have been limited to 4 km/s. This is probably due to flyer breakup because of its shock loading in the initial stage or because of jumping of fast moving plasma over it. In further studies a significant increase has been observed in the flyer velocity, when barrel dimensions were kept smaller than the foil dimensions. This experimental observation has been termed as the plasma propulsion effect, where the thrust on the flyer has been enhanced due to presence of compressed high pressure plasma in the unexposed portion of the excess foil under barrel surface. Using this scheme we obtained a velocity of 6.2 km/s on polyimide flyers of thickness 170 µm and diameter 6 mm.

Another significant and unexpected effect is observed, when the exploding foil assemblies were operated under vacuums to reduce the air drag. But instead of an increase, a significant reduction has been observed in flyer velocities and degradation in foil explosion characteristics under vacuum. Experimental investigation of this effect has been carried out at different vacuum levels ranging from 1 bar to 1×10^{-4} mbar and it has been observed that exploding foil shows an anomalous behavior under vacuum (< 900 mbar). The detailed analysis of current and voltage measurements indicates that the energy deposited in the foil after the burst drops significantly when operated in vacuum. No signature of foil burst has been observed in a vacuum range from 100 mbar to 0.05 mbar, and in close by vacuum regions energy deposited till burst has also been found to be much smaller than its value at atmospheric or low vacuum regions. Possible cause for this behavior appears to be the formation of a low resistance breakdown channel parallel to metal foil. This parallel breakdown channel might be initiated by the electrons contributed by the partial dissociation of atoms at higher temperature in the vicinity

of molten foil material with enhanced interaction length in presence of generated magnetic field near the foil.

A 1D hydrodynamic code based on realistic models of equation of state and electrical resistivity has been modified to numerically simulate the flyer velocity profiles. Computed velocity profiles have been compared with the experimental and simulated velocity profiles reported on 100 kV Lawrence Livermore National Laboratory (LLNL) system. Better match to the experimental velocity profiles have been obtained with the present scheme than the reported MHD modeling [103]. The computed final velocities have also been found in good agreement with the experimental values reported on LLNL 40 kV as well as 100 kV systems at different charging voltages. The simulated velocity profiles for ELG-8 bank developed in our laboratory show a deviation of 1 km/s caused by the variation in experimental and numerical burst time, which requires some improvements in the resistivity model parameters to better represent the exploding foil material used in present experiments.

Another significant outcome of this research is the development of a dual beam Fabry-Perot velocimeter, which can simultaneously measure two velocities using single laser, streak camera and Fabry-Perot interferometer. This improvement makes this technique a standalone diagnostics for equation of state (EOS) measurements. In this approach, surfaces under study are illuminated by two closely spaced (2-3 mm) nearly parallel optical beams derived from a single laser. The scattered light collected from both the surfaces is used to generate a superimposed interference patterns on a single streak camera, which can resolve the velocities of individual surfaces moving with different velocities at different time instances. The measurement errors of this system have been analyzed and are found to be mainly decided by the accuracies in prediction of fringe diameters. To improve these accuracies the spatial profiles of fringes has

been analyzed to determine the peak position and fringe diameters at the time of impact, which becomes easier when both velocity profiles are available on same streak record. The other important parameter of a velocimeter is its temporal resolution which is mainly decided by the cavity fill time of etalon and streak camera resolution. In present experimental setup the dominating factor was found to be cavity fill time and the temporal resolution has been found to be approximately 3 ns.

To determine the shock velocity in stepped targets, simple fiber optic pins have been developed along with fast photodiodes. The response time of these pins has been determined to be better than 3 ns with the available pulse light sources. These pins are helpful in measuring the equation of state data, when target reflections are poor.

With this optimized setup and diagnostics, various metals like tantalum, tin and aluminum have been subjected to shock compression and peak particle velocities at the target-glass interface as measured by Fabry-Perot velocimeter and found to be in good agreement with the reported equation of state data. These studies have been further extended to measure the target velocity profile under phase transition in iron foils. A series of experiments have been carried out on iron samples from 20 GPa to 55 GPa pressure and target/ window interface velocity profiles have been measured. A kink near 15 GPa has been observed when the sample was subjected to a peak pressure of 44 GPa, indicating a polymorphic transition. At lower peak pressures near to 20 GPa, a clear two wave structure with a detailed release profile was recorded. Deduced pressure profiles show a transition in iron from bcc to hcp phase at 13.6 GPa under shock, which is well in agreement with the reported values. To check the performance of present setup at highest possible pressure shock experiments were also carried out on tantalum at 70 GPa pressure using LiF window and aluminum laminated flyers.

To measure the equation of state of any unknown material, shock velocity is measured in the stepped targets of copper and tantalum using fiber optic pins. The time delay between the shock breakouts at two steps have been used to determine the shock velocity and the flyer velocity was taken from previous experiments. Using this experimental scheme equation of state points for copper at 23 GPa and tantalum at 48 GPa have been measured. A comparison with their known Hugoniots shows a close match between the two, which also confirms the potential of present electric gun.

The significance of present research is to establish a portable setup for shock studies on materials having importance in shock research and useful for nuclear systems. To fulfill this aim, we have considered zirconium and titanium metals for high pressure studies using dual beam velocimeter. These metals also have associated phase transition characteristics which are still the topic of interest in scientific research. Equation of state measurements have been carried out on zirconium and titanium metals under shock loading up to pressures of 12 GPa and 16 GPa respectively. Measured EOS data on thin foils has been found to be matching well with the data reported in literature on relatively much thicker samples. The detailed velocity profiles of target-glass interface show a weak kink in its rising part indicating a phase transition from α phase to ω phase. The transition pressure in present study is found to be approximately 8.2 GPa for zirconium (overall purity 99.5%) and 11.4 GPa $\pm$ 1.6 GPa for titanium (overall purity 99.99%). These experiments also first time demonstrate the potential FPV in dual beam mode to determine the EOS of different materials.

Future scope of studies

This is the beginning of shock studies using portable electrically exploding foil accelerator along with dedicatedly developed dual beam Fabry-Perot velocimeter. There are various interesting phenomenon that can be investigated at the pressures (~70 GPa) achievable on this setup. Using reverse impact technique, and measuring the sound velocity, it is possible to detect the polymorphic transitions occurring with small volume change which are difficult to observe under shock loading, like bct to bcc transition in tin at ~ 40 GPa [138] and disputed polymorphism in tantalum [139, 140]. The studies reported on zirconium and titanium still requires an investigation, as in present work the phase transition characteristics are reported on a single overall impurity concentration, which may be varied further with the knowledge of individual impurity contents.

Another interesting effect of shock loading time on polymorphic phase transition can be investigated on present setup by using thinner projectiles. The phase transitions requiring longer time durations for completion may result in metastable states lying on the extended Hugoniot of first phase [141]. If sample thickness is sufficient then these metastable states may finally decay to a state on second phase Hugoniot. But if sample thickness is small then the temporal evolution of shock or particle velocity, may provide information about the kinetics of transitions from metastable state to a state on second phase Hugoniot. In near future these investigations will be carried out by varying the projectile and sample thicknesses.

Temperature is a crucial parameter of equation of state, and is not determined by present velocity measurements. Temporal measurement of temperature along with shock loading is helpful in generating complete information about high pressure behavior of materials [142].

Therefore in near future a radiation pyrometer [91] will also be used in shock measurements on present setup. The work to achieve much higher flyer velocities (near to 8 km/s or more) by increasing the current amplitude and decreasing its rise time is in progress. This also requires the implementation of low inductance spark gap as well as capacitor bank and investigations to reduce their inductances are in progress. The work is also on to develop a fiber optic based velocimeter that may enhance the capabilities of present setup for multipoint measurements.

References

[1]. L. Dubrovinsky, N. Dubrovinskaia, E. Bykova, M. Bykov, V. Prakapenka, C. Prescher, K. Glazyrin, H.-P. Liermann, M. Hanfland, M. Ekholm, Q. Feng, L. V. Pourovskii, M. I. Katsnelson, J. M. Wills, and I. A. Abrikosov, "The most incompressible metal osmium at static pressures above 750 gigapascals," Nature, **525**, 226 (2015).

[2]. R. Hawke, D. E. Duerre, J. G. Huebel, J. G. Klapper, D. J. Steinberg, and R. N. Keeler, "Method of isentropically compressing materials to several megabars," J. Appl. Phys. **43**, 2734 (1972).

[3]. G. Wang, B. Luo, X. Zhang, J. Zhao, C. Sun, F. Tan, T. Chong, J. Mo, G. Wu and Y. Tao, "A 4 MA, 500 ns pulsed power generator CQ-4 for characterization of material behaviors under ramp wave loading," Rev. Sci. Instrum. **74**, 0151117 (2013).

[4]. N. Amadou, E. Brambrink, A. Benuzzi-Mounaix, T. Vinci, T. de Resseguier, S. Mazevet, G. Morard, F. Guyot, N. Ozaki, K. Miyanishi, and M. Koenig, "Laser-driven quasi-isentropic compression experiments and numerical studies of the iron alpha-epsilon transition in the context of planetology," AIP Conf. Proc. **1426**, 1525 (2012).

[5]. L. M. Barker, "High-pressure quasi-isentropic impact experiments," in: *Shock Compression of Condensed Matter*, edited by J. R. Asay, R. A. Graham, and G. K. Straub (North–Holland, Amsterdam, 1983), p. 111.

[6]. A. Ray and S. V. G. Menon, "Quasi-isentropic compression using functionally graded materials in gas gun and explosive driven systems," J. Appl. Phys. **105**, 064501 (2009).

[7]. A. R. Kutsar, M. N. Pavlovskii, and V. V. Komissarov, "Observation of a two-wave shock configuration in zirconium," JETP Lett. **39**, 480 (1984).

[8]. E. Cerreta, G.T. Gray, R. Hixson, P. A. Rigg, and D. W. Brown, "The influence of interstitial oxygen and peak pressure on the shock loading behavior of zirconium," Acta. Mater. **53,** 1751 (2005).

[9]. S. V. Razorenov, A. V. Utkin, G. I. Kanel, V. E. Fortov, A. S. Yarunichev, K. Baumung, and H. U. Karow, "Response of high-purity titanium to high-pressure impulsive loading," High Press. Res. **13**, 367 (1995).

[10]. A. R. Kutsar, M. N. Pavlovskii, and V. V. Komissarov, "Observation of a two-wave shock configuration in titanium," JETP Lett. **35**, 108 (1982).

[11]. S. K. Sikka, Y. K. Vohra, and R. Chidambaram, "Omega phase in materials," Prog. Mater. Sci. **27**, 245 (1982).

[12]. R. G. Hennig, D. R. Trinkle, J. Bouchet, S. G. Srinivasan, R. C. Albers, and J. W. Wilkins, "Impurities block the α to ω martensitic transformation in titanium," Nat. Mater. **4**, 129 (2005).

[13]. N. Velisavljevic, G. N. Chesnut, L. L. Stevens, and D. M. Dattelbaum, "Effects of interstitial impurities on the high pressure martensitic α to ω structural transformation and grain growth in zirconium," J. Phys.: Condens. Matter. **23**, 125402 (2011).

[14]. E. K. Cerreta, F. L. Addessio, C. A. Bronkhorst, D. W. Brown, J. P. Escobedo, S. J. Fensin, G. T. Gray III, T. Lookman, P. A. Rigg, and C. P. Trujillo, "The influence of peak shock stress on the high pressure phase transformation in Zr," J. Phys.: Conf. Ser. **500**, 032003 (2014).

[15]. J. P. Escobedo, E. K. Cerreta, C. P. Trujillo, D. T. Martinez, R. A. Lebensohn, V. A. Webster, and G.T. Gray III, "Influence of texture and test velocity on the dynamic, high-strain, tensile behavior of zirconium," Acta. Mater. **60**, 4379 (2012).

[16]. H. R. Wenk, P. Kaercher, W. Kanitpanyacharoen, E. Z. Alarcon, and Y. Wang, "Orientation relations during the α-ω phase transition of zirconium: In situ texture observations at high pressure and temperature," Phys. Rev. Lett. **111**, 195701 (2013).

[17]. D. R. Trinkle, R. G. Hennig, S. G. Srinivasan, D. M. Hatch, M. D. Jones, H. T. Stokes, R. C. Albers, and J. W. Wilkins, "New mechanism for the α to ω martensitic transformation in pure titanium," Phys. Rev. Lett. **91**, 025701 (2003).

[18]. R. E. Duff and A. N. Blackwell, "Explosive driven shock tubes," Rev. Sci. Instrum. **37**, 579 (1966).

[19]. T. J. Ahrens, "Shock wave techniques for geophysics and planetary physics," in: *Methods of experimental physics: Geophysics laboratory measurement*, (Academic Press Inc. Orlando Florida, 1987), p. 185.

[20]. H. F. Swift, "Light gas gun technology: A Historical perspective," in: *High pressure shock compression of solids VIII: The science and technology of high-velocity impact*, edited by L. C. Chhabildas, L. Davison, and Y. Horie, (Springer-Verlag Berlin Heidelberg Germany, 2005), p.1.

[21]. A. C. Charters, "Development of the high-velocity gas-dynamics gun," Int. J. Impact Engng. **5**, 183 (1987).

[22]. L. C. Chhabildas and M. D. Knudson, "Techniques to launch projectile plates to very high velocities," in: *High pressure shock compression of solids VIII : The science and technology of high-velocity impact*, edited by L. C. Chhabildas, L. Davison, and Y. Horie, (Springer-Verlag Berlin Heidelberg Germany, 2005), p.143.

[23]. L. C. Chhabildas, L. N. Kmetyk, W. D. Reinhart, and C. A. Hall, "Enhanced hypervelocity launcher - capabilities to 16 km/s," Int. J. Impact. Engng. **17**, 183 (1995).

[24].   D. Wetz, F. Stefani, J. Parker, and I. McNab, "Development of a Plasma-Driven Railgun to Reach 7 km/s," Proc. IEEE Int. Power Mod. and High Voltage Conf. May 2008, pp.85-88.

[25].   D. Wetz, F. Stefani, D. Motes, J. Parker, and I. McNab, "Development of a plasma railgun for affordable and rapid access to space," 16th IEEE Int. Pulsed Power Conf. **2**, 1799, (2007).

[26].   R. W. Karhi, D. A. Wetz, M. Giesselmann, J. J. Mankowski, J. P. Diehl, and P. M. Kelly, "A 40-Stage Synchronous Distributed Energy Railgun," IEEE Trans. Plasma Sci. **39**, 1192, (2011).

[27].   D. V. Keller and R. J. Penning Jr., "Exploding foils: The production of plane shock waves and acceleration of thin plates," in: *Exploding Wires-Vol.2*, edited by W. G. Chace and H. K. Moore, (Plenum Press Inc. NY, 1962), p. 263.

[28].   A. H. Guenther, D. C. Winsch and T. D. Soapes, "Acceleration of thin plates by exploding foil techniques," in: *Exploding Wires- Vol.2*, edited by W. G. Chace and H. K. Moore, (Plenum Press Inc. NY, 1962), p. 279.

[29].   H. H. Chau, G. Dittbenner, W. W. Hofer, C. A. Honodel, D. J. Steinberg, J. R. Stroud and R. C. Weingart, "Electric gun: A versatile tool for high pressure shock research," Rev. Sci. Instrum. **51**, 1676 (1980).

[30].   K.E. Froeschner, R. S. Lee, H. H. Chau and R. C. Weingart, "Performance of a 100 kV/ 78 kJ electric gun system," in: *Shock Waves in Condensed Matter: Proceedings of the American Physical Society, Topical Conference, Sante Fe, Mexico-July1983*, edited by J. R. Assay, R. A. Graham, and G. K. Straub, (North-Holland, Amsterdam, 1984), p. 85.

[31]. A. M. Frank and H. H., Chau, "Six mm, plane-wave shock driver," LLNL Report No.UCRL-JC-1131301 (1993).

[32]. H. R. Kleinhanβ, F., Lungenstraβ and H. Zollner, "Initiation threshold of high explosives in small flyer plate experiments," Proc. ninth Symposium (International) on Detonation, OCNR 113291-7, Office of Naval Research, Portland, USA, (1989), p. 66.

[33]. J. E. Osher, H. H. Chau, G. R. Gathers, R. S. Lee, and R. C. Weingart, "Applications of a 100-kV electric gun for hypervelocity impact studies," Int. J. Impact Engng. **5**, 501 (1986).

[34]. R. W. Lemke, M. D. Knudson, and J. P. Davis, "Magnetically driven hyper-velocity launch capability at the Sandia Z accelerator," Int. J. Impact Engng. **38**, 480 (2011).

[35]. H. Nagao *et al.*, "Hugoniot measurement of diamond under laser shock compression up to 2 TPa," Phys. Plasmas. **13**, 052705 (2006).

[36]. N. Holmes, R. Trainor, R. More, and R. Anderson, "Laser-generated shock wave experiments at pressures above 1 TPa," IEEE J. Quantum Elec. **15**, 946 (1979).

[37]. L. D. Landau and E. M. Liftshitz, in: *Fluid Mechanics vol-6, 2nd edition: Course of Theoretical Physics*, (Pergamon Headington Hill Hall, Oxford U. K. 1987).

[38]. Lee Davison, in: *Fundamentals of shock wave propagation in solids,* (Springer-Verlag Berlin Heidelberg Germany, 2008).

[39]. M. B. Boslough and J. R. Asay, "Basic Principles of shock compression" in: *High pressure shock compression of solids*, edited by J. R. Asay, and M. Shahinpoor, (Springer-Verlag Berlin Heidelberg Germany, 1992), p.36.

[40]. T. J. Ahrens, "Shock wave techniques for geophysics and planetary physics," in: *Methods of experimental physics: Geophysics laboratory measurement*, (Academic Press Inc. Orlando Florida, 1987), pp.185-233.

[41]. M. Temporal, B. Canaud, W. J. Garbett and R. Ramis, "Uniformity of spherical shock wave dynamically stabilized by two successive laser profiles in direct-drive inertial confinement fusion implosions," Phys. Plasmas. **22**, 102709 (2015).

[42]. G. I. Kanel, S. V. Razorenov, and V. E. Fortov, in: *Shock-Wave Phenomena and the Properties of Condensed Matter,* (Springer, NY, 2004) p.6.

[43]. D. Bancroft, E. L. Peterson, and S. Minshall, "Polymorphism of iron at high pressure," J. Appl. Phys. **27**, 291 (1956).

[44]. H. Mao, W. A. Bassett, and T. Takahashi, "Effect of pressure on crystal structure and lattice parameters of iron up to 300 kbar," J. Appl. Phys. **28**, 272 (1967).

[45]. R. A. Graham, in: *Solids under high pressure-shock compression: Mechanics physics and chemistry*, (Springer-Verlag NY, 1993), Chap. 3, p.55.

[46]. H. S. Yadav and N. K. Gupta, "Flyer plate motion and its deformation during flight," Int. J. Impact Engng., **7**, 71 (1988).

[47]. Y. V. Bat'kov, N. P. Kovalev, A. D. Kovtun, V. G. Kuropatkin, A. I. Lebedev, Y. M. Makarov, S. F. Manachkin, S. A. Novikov, V. A. Raevsky, and Y. M. Styazhkin, "Explosive three-stage launcher to accelerate metal plates to velocities more than 10 km/s," Int. J. Impact Engng. **20**, 89, (1997).

[48]. M. De Icaza, C. T. Renero, and F. E. Prieto, "Experimental facilities for impact physics research at the National University of Mexico," Physica B+C, **139**, 599 (1986).

[49]. R. A. Burden, J. W. Gray, and C. M. Oxley, "Explosive foil injection (EFI) pre-accelerator for electromagnetic launchers," IEEE Trans. Magn. **25**, 107, (1989).

[50]. P. Lehmann, J. Wey, H. Mach, A. Eichhorn and K. Daree, "Study of a railgun plasma armature," IEEE Trans. Plasma Sci. **17**, 371 (1989).

[51]. Y. Zhou, P. Yan, Y. Sun, W. Yuan, D. Zhang, and M. Li, "Design of a distributed energy store rail gun," IEEE Trans. Plasma Sci., **39**, 230 (2011).

[52]. I. R. McNab, F. Stefani, M. Crawford, M. Erengil, C. Persad, S. Satapathy, H. Vanicek, T. Watt, and C. Dampier, "Development of a naval rail gun," IEEE Trans. Magn. **41**, 206, (2005).

[53]. I. T. Jr. Luke and M. F. Stumborg, "The operational value of long range land attack EM guns to future naval forces," IEEE Trans. Magn. **37**, 58 (2001).

[54]. M. D. Knudson, "Megaamps, megagauss, and megabars: Using the Sandia Z Machine to perform extreme material dynamics experiments," AIP Conf. Proc. **1426**, 35 (2012).

[55]. J-P Davis, C. Deeney, M. D. Knudson, R. W. Lemke, T. D. Pointon, and D. E. Bliss, "Magnetically driven isentropic compression to multimegabar pressures using shaped current pulses on the Z accelerator," Phys. Plasmas. **12**, 056310 (2005).

[56]. I. Gilath, "Laser induced spallation and dynamic fracture at ultra high strain rate" in: *High pressure shock compression of solids: Dynamic Fracture and Fragmentation*, edited by L. Davison, D. E. Grady and M. Shahinpoor, (Springer-Verlag NY, 1996), p.92.

[57]. L. R. Veeser and S. C. Solem, "Studies of laser-driven shock waves in aluminum," Phys. Rev. Lett. **40**, 1391 (1978).

[58]. R. Cauble, D. W. Phillion, T. J. Hoover, N. C. Holmes, J. D. Kilkenny, and R. W. Lee, "Demonstration of 0.75Gbar planar shocks in X-ray driven colliding foils," Phys. Rev. Lett. **70**, 2102 (1993).

[59]. S. Eliezer, J. J. Honrubia and G. Velarde, "Direct-indirect drive a new possibility for laser induced fusion," Phys. Lett. A, **166**, 249 (1992).

[60]. T. Mochizuki S. Sakabe and C. Yamanaka, "X-Ray Geometrical Smoothing Effect in Indirect X-Ray-Drive Implosion," Japan. J. Appl. Phys. **22**, L124 (1983).

[61]. S. N. Luo, D. C. Swift, T. E. Tierney, D. L. Paisley, G. A. Kyrala, R. P. Johnson, A. A. Hauer, O. Tschauner, and P. D. Asimow, "Laser induced shock waves in condensed matter: some techniques and applications," High Press. Res. **24**, 409 (2004).

[62]. N. A. Tahir, D. H. H. Hoffmann, A. Kozyreva, A. Shutov, J. A. Maruhn, U. Neuner, A. Tauschwitz, P. Spiller, and R. Bock, "Shock compression of condensed matter using intense beams of energetic heavy ions," Phys. Rev. E. **61**, 1975 (2000).

[63]. D. H. H. Hoffmann, A. Blazevic, P. Ni, O. Rosmej, M. Roth, N. A. Tahir, A. Tauschwitz, S. Udrea, D. Varentsov, K. Weyrich, and Y. Maron, "Present and future perspectives for high energy density physics with intense heavy ion and laser beams," Laser Part. Beams **23**, 47 (2005).

[64]. R. J. Wasley, J. F. O'Brien, and D. R. Henley, "Design and construction of a new coaxial electrical discharge pin," Rev. Sci. Instrum. **35**, 466 (1964).

[65]. W. M. Isbell, in: *Shock waves: Measuring the dynamic response of materials*, (Imperial College Press, 2005), p.130.

[66]. R. F. Benjamin and F. J. Mayer, "Applications of the microshell-tipped optical fiber," *Optical Fiber Sensors*, (Optical Society of America, 1985), paper ThFF4.

[67]. L. M. Barker, M. Shahinpoor and L. C. Chhabildas, "Experimental and diagnostic techniques" in: *High pressure shock compression of solids*, edited by J. R. Asay, and M. Shahinpoor, (Springer-Verlag Berlin Heidelberg Germany, 1992), p.55.

[68]. G. Yiannakopoulos, "A review of Manganin gauge technology for measurements in gigapascal range," MRL Technical Report No. MRL-TR-90-5 (1990).

[69]. C. S. Lynch, "Strain compensated thin film stress gauges for stress wave measurements in the presence of lateral strain," Rev. Sci. Instrum. **66**, 5582 (1995).

[70]. F. Bauer, "PVDF gauge piezoelectric response under two-stage light gas gun impact loading," AIP Conf. Proc. **620**, 1149 (2002).

[71]. F. Bauer, "PVF$_2$ polymers: Ferroelectric polarization and piezoelectric properties under dynamic pressure and shock wave action," Ferroelectrics, **49**, 231 (1983).

[72]. L. M. Barker and R. E. Hollenbach, "Interferometer technique for measuring the dynamic mechanical properties of materials," Rev. Sci. Instrum. , **36**, 1617 (1965).

[73]. L. M. Barker and R. E. Hollenbach, "Velocity interferometery for time resolved high velocity measurements," Proc. of High Speed Photography, Videography & Photonics, Soc. Photo Opt. Instrum. Eng. **427**, 116 (1984).

[74]. P. M. Johnson and T. J. Burgess, "Free surface velocity measurement of an impacted projectile by optical Doppler shift," Rev. Sci. Instrum. **39**, 1100, (1968).

[75]. L. M. Barker and R. E. Hollenbach, "Laser interferometer for measuring high velocities of any reflecting surface", J. Appl. Phys. **43**, 4669 (1972).

[76]. R. L. Hilliard and C. G. Shepherd, "Wide Angle Michelson Interferometer for measuring Doppler line width," J. Opt. Soc. Am. **56,** 362 (1966).

[77]. G. M. B. Bouricious and S. F. Clifford, "An optical interferometer using polarization coding to obtain quadrature phase components," Rev. Sci. Instrum. **41**, 1800 (1970).

[78]. W. F. Hemsing, "Velocity sensing interferometer (VISAR) modification," Rev. Sci. Instrum. **50**, 73 (1979).

[79]. D. D. Bloomquist and S. A. Sheffield, "Optically recording interferometer for velocity measurement with subnanosec resolution," J. Appl. Phys. **54**, 1717, (1983).

[80]. M. Durand, P. Laharrague, P. Lalle, A. Le Bihan, J. Morvan and H. Pujols, "Interferometric laser technique for accurate velocity measurement in shock wave physics", Rev. Sci. Instrum. **48**, 275 (1977).

[81]. C. F. McMillan, D. R. Goosman, N. L. Parker, L. L. Steinmetz, H. H. Chau, T. Huen, R. K. Whipkey, and S. J. Perry, "Velocimetry of fast surfaces using Fabry-Perot interferometer," Rev. Sci. Instrum. **59**, 1 (1988).

[82]. W. L. Seitz and H. L. Stacy, "Fabry-Perot interferometery using an image intensified rotating mirror streak camera," Proc. of High Speed Photography, Videography & Photonics, Soc. Photo Opt. Instrum. Eng. **427**, 186 (1983).

[83]. D. R. Goosman, A. M. Frank, H. H. Chau, and N. L. Parker, "Fabry-Perot velocimeter technique: Is Doppler shift is affected by surface normal direction," Proc. of High Speed Photography, Videography & Photonics, Soc. Photo Opt. Instrum. Eng. **427**, 127 (1983).

[84]. D. R. Goosman, "The multibeam Fabry-Perot velocimeter," Sci. & Tech. Rev. LLNL Livermore, California, (July 1996) p.12.

[85]. A. K. Saxena, T. C. Kaushik, and Satish C. Gupta, "Shock loading characteristics of Zr and Ti metals using dual beam velocimeter," J. Appl. Phys. **118**, 075904 (2015).

[86]. J. Weng, H. Tan, S. Hu, Y. Ma and X. Wang, "New all fiber velocimeter," Rev. Sci. Instrum. **76**, 093301 (2005).

[87]. O. T. Strand, D. R. Goosman, C. Martinez, T. L. Whitworth, and W. W. Kuhlow, "Compact system for high-speed velocimetry using heterodyne techniques," Rev. Sci. Instrum. **77**, 083108 (2006).

[88]. J. Weng, X. Wang, Y. Ma, H. Tan, L. Cai, J. Li, and C. Liu, "A compact all-fiber displacement interferometer for measuring the foil velocity driven by laser," Rev. Sci. Instrum. **79**, 113101, (2008).

[89]. J. Weng, H. Tan, S. Hu, Y. Ma, and X. Wang, "New all fiber velocimeter," Rev. Sci. Instrum. **76**, 093301 (2005).

[90]. M. B. Boslough and T. J. Ahrens, "A sensitive time-resolved radiation pyrometer for shock-temperature measurements above 1500 K," Rev. Sci. Instrum. **60**, 3711 (1989).

[91]. A. S. Rav, A. K. Saxena, K. D. Joshi, T. C. Kaushik, and S. C. Gupta, "Time resolved radiation pyrometer for transient temperature measurement," AIP Conf. Proc. **1349**, 451 (2011).

[92]. W. M. Isbell, "Historical overview of hypervelocity impact diagnostic technology," Int. J. Impact Engng. **5**, 389 (1987).

[93]. D. H. Kalantar *et al.*, "Direct observation of the α−ε transition in shock-compressed iron via nanosecond X-ray diffraction," Phys. Rev. Lett. **95**, 075502 (2005).

[94]. S. A. Sheffield, R. L. Gustavsen and R. R. Alcon, "In-situ magnetic gauging technique used at LANL - method and shock information obtained," AIP Conf. Proc. **505,** 1043 (2000).

[95]. R. S. Lee, J. E. Osher, H. H. Chau, G. Pomykal and R. D. Speer, "1 MJ electric gun facility at LLNL," IEEE. Trans. Magn. **29**, 457 (1993).

[96]. D. J. Hatt and Philip F. X. Ryan, "Calibration and testing of a large scale electric gun for shock Hugoniot measurements," MRL Technical Report, MRL-TR-93-24, DSTO Materials Research Laboratory, Australia (1993).

[97]. G. J. Wang , J. He , J. Zhao , F. Tan , C. Sun , J. Mo , X. Xong and G. Wu, "The techniques of metallic foil electrically exploding driving hypervelocity flyer to more than 10 km/s for shock wave physics experiments," Rev. Sci. Instrum., **82**, 095105 (2011).

[98]. A. K. Saxena, T. C. Kaushik and S. C. Gupta, "Shock experiments and numerical simulations on low energy portable electrically exploding foil accelerators," Rev. Sci. Instrum. **81**, 033508 (2010).

[99]. R. Bealing and P. G. Carpenter, "Exploding foil devices for shaping meg-amp current pulses," J. of Phys. E: Sci. Instrum. **5**, 889 (1972).

[100]. T. J. Tucker and P. L. Stanton, "Electrical Gurney Energy: A new concept in modeling of energy transfer from electrically exploded conductors," Sandia National Laboratory Report, SAND 75- 0244 (1975).

[101]. T. C. Kaushik, L. V. Kulkarni, and S. K. H. Auluck, "Feasibility studies on performance enhancement in electrically exploding foil accelerators," IEEE Trans. Plasma Sci. **30**, 2133 (2002).

[102]. S. C. Schmidt, W. L. Seitz and J. Wackerle, "An empirical model to compute the velocity histories of flyers driven by electrically exploding foils Los Alamos National Laboratory Report: LA-6809 (1977).

[103]. J. E. Osher, G. B. Henry, H. Chau, R. S. Lee, C. Lee, R Seeper and R. C. Weingart, "Operating characteristics and modeling of the LLNL 100-kV electric gun," IEEE Trans. on Plasma Sci. **17**, 392 (1989).

[104]. B.-Q. Luo, C.-W. Sun, J.-H. Zhao, J. He, "Unified numerical simulation of metallic foil electrical explosion and its applications," IEEE Trans. Plasma Sci. **41**, 49 (2013).

[105]. A. K. Saxena, T. C. Kaushik, M. P. Goswami, and S. C. Gupta, "Printed circuit board based electrically triggered compact rail gap switch," Rev. Sci. Instrum. **81**, 056106 (2010).

[106]. http://in.tek.com/datasheet/high-voltage-probe-single-ended/p5100a-tpp0850-p5122-p5150-p6015a-datasheet-0

[107]. R. H. Huddlestone and S. L. Leonard, in: *Plasma Diagnostic Techniques*, (Academic Press, NY, 1965), Chap. 2.

[108]. H. Knopfel, in: *Pulsed High Magnetic Field*, (North-Holland Publishing Company, Amsterdam–London, 1970), p.132.

[109]. M. Born and E. Wolf, in: *Principles of Optics*, (Pergamon, NY, 1983), p.329.

[110]. E. Hecht, in: *Optics*, (Person Education Inc. India, 2008), Chap. 9, p.416.

[111]. M. Durand, P. Lalle, and Andriot, "Eight beam Fabry-Perot velocimeter," AIP Conf. Proc. **309**, 1751 (1994).

[112]. A. K. Saxena, T.C. Kaushik, A. M. Rawool and Satish C. Gupta, "Equation of state measurements using single Fabry-Perot velocimeter," J. of Phys: Conf. Series. **377**, 012049 (2012).

[113]. T. C. Kaushik and B. K. Godwal, "Numerical study of the impedance mismatch effect in laser irradiated layered targets", J. Appl. Phys. **64**, 4889 (1988).

[114]. D. J. McCloskey, "An analytic formulation of equation of state," Rand Corp. Report RM-3905-PR (1964).

[115]. T. J. Burgess, "Electrical resistivity model of metals," 4th Int. Conf. On Megagauss Magnetic Field Generation and Related Topics, Santa Fe, NM, USA, 307 (1986).

[116]. R. D. Richtmyer and K.W. Morton, in: *Difference methods for initial value problems*, 2nd ed., (Interscience, NY, 1967).

[117]. B. K. Godwal, T. C. Kaushik, and S. K. Sikka, "Equation of state in laser shock simulation", Laser Part. Beams **15** 353 (1997).

[118]. J. VonNeumann and R. D. Richtmyer, "A method for the numerical calculation of hydrodynamic shock," J. Appl. Phys. **21**, 232 (1950).

[119]. A. K. Saxena, A. M. Rawool, and T. C. Kaushik, "Crowbar scheme based on plasma motion for pulsed power applications," IEEE Trans. Plasma Sci. **41**, 3058 (2013).

[120]. B. M. Kovalchuk, A. A. Kim, A. V. Kharlov, E. V. Kumpyak, N. V. Tsoy, V. V. Vizir, and V. B. Zorin, "Three-electrode gas switches with electrodynamical acceleration of a discharge channel," Rev. Sci. Instrum. **79**, 053504 (2008).

[121]. D. O. Campos, M. Machida, R. Y. Honda, E. A. Aramaki and L. A. Berni, "Analytic study on high-voltage crowbar system," Jpn. J. Appl. Phys. **34**, 5818 (1995).

[122]. G. H. Rim, C. H. Chu, Y. W. Choi, Y. S. Jin, and E. P. Pavlov, "Protection scheme of a charging and discharging system for a 500 kJ capacitor bank," IEEE Trans. Mag. **37**, 389 (2001).

[123]. A. V. Kharlov, "Arc motion and electrode erosion in high current spark gaps," IEEE Trans. Plasma Sci. **38,** 2474 (2010).

[124]. C. Grabowski, J. H. Degnan, T. Cavazos, D. G. Gale, C. Gilman, W. Sommars, T. P. Intrator, J. M. Taccetti, B. Waganaar, R. E. Siemon and G. A. Wurden, "Development of a high current low inductance crowbar switch for FRX-L," IEEE Trans Plasma Sci. **30**, 1905 (2002).

[125]. A. K. Saxena, M. G. Sharma, T. C. Kaushik, "Anomalous behavior of electrically exploding aluminum foils under vacuum," IEEE Trans. Plasma Sci. **43**, 2682 (2015).

[126]. A. S. Pillai and R. Hackam, "Surface flashover of solid insulators in atmospheric air and in vacuum," J. Appl. Phys. **58**, 146 (1985).

[127]. B. Stenerhag, S. K. Händle, and B. Göhle, "Effect of wire parameters on the emission of hard X rays from exploding wires," J. Appl. Phys. **42** 1876 (1971).

[128]. B. Stenerhag, S. K. Händle, and I. Holmström, "Exploding wires in air and vacuum," Z. Physik, **198**, 172 (1967).

[129]. I. M. Vitkovitsky and V. E. Scherrer, "Recovery characteristic of exploding wire fuses in air and vacuum," J. Appl. Phys. **52**, 3012 (1981).

[130]. E. Sili, J. P. Cambronne, and F. Koliatene, "Temperature dependence of electrical breakdown mechanism on the left of the Paschen minimum," IEEE Trans. Plasma Sci. **39**, 3173 (2011) and also the Ref. 11 cited therein.

[131]. S. P. Marsh, in: *LASL Shock Hugoniot Data,* (University of California Press, London U.K., 1980).

[132]. D. E. Grady and L. C. Chhabildas, "Shock-wave properties of soda-lime glass," Sandia Report No. SAND 096-2571-C (1996).

[133]. L. M. Barker and R. E. Hollenbach, "Shock wave study of the $\alpha \Leftrightarrow \varepsilon$ phase transition in iron," J. Appl. Phys. **45**, 4872 (1974).

[134]. E. Cerreta, G. T. Gray III, A. C. Lawson, T. A. Mason, and C. E. Morris, "The influence of oxygen content on the α to ω phase transformation and shock hardening of titanium," J. Appl. Phys. **100**, 013530 (2006).

[135]. C. W. Greeff, "Phase changes and equation of state of Zr," Modelling Simul. Mater. Sci. Eng. **13**, 1015 (2005).

[136]. C. S. Alexander, "Index of refraction of shock loaded soda-lime glass," AIP Conf. Proc. **1195**, 1431 (2009).

[137]. C. W. Greeff, D. R. Trinkle, and R. C. Albers, "Shock induced α-ω transition in titanium," J. Appl. Phys. **90**, 2221 (2001).

[138]. J. Hu, X. Zhou, H. Tan, J. Li, and C. Dai, "Successive phase transition in tin under shock compression,", Appl. Phys. Lett. **92**, 111905 (2008).

[139]. F. Xi, K. Jin, L. Cai, H. Geng, Y. Tan, and Jun Li, "Sound velocity of tantalum under shock compression in the 18–142 GPa range," J. Appl. Phys. **117**, 185901 (2015).

[140]. L. Burakovsky, S. P. Chen, D. L. Preston, A. B. Belonoshko, A. Rosengren, A. S. Mikhaylushkin, S. I. Simak, and J. A. Moriarty, "High-pressure-high-temperature polymorphism in Ta: resolving an ongoing experimental controversy," Phys. Rev. Lett. **104**, 255702 (2010).

[141]. J. W. Forbes, in: *Shock wave compression of condensed matter: Shock wave and high pressure phenomenon: A primer*, (Springer NY, 2012) pp.201-241.

[142]. T. Kimura, N. Ozaki, T. Sano, T. Okuchi, T. Sano, K. Shimizu, K. Miyanishi, T. Terai, T. Kakeshita, Y. Sakawa, and R. Kodama, "P-ρ-T measurements of H_2O up to 260 GPa under laser-driven shock loading," J. Chem. Phys. **142**, 164504 (2015).